

The *Spitzer* Local Volume Legacy: Survey Description and Infrared Photometry

D.A. Dale¹, S.A. Cohen¹, L.C. Johnson¹, M.D. Schuster¹, D. Calzetti², C.W. Engelbracht³,
R.C. Kennicutt^{4,3}, J.C. Lee⁵, M. Block³, A. Begum⁴, J.J. Dalcanton⁶, J.G. Funes⁷,
A. Gil de Paz⁸, K.D. Gordon⁹, B.D. Johnson¹⁰, A.R. Marble², S. Sakai¹¹, E.D. Skillman¹²,
L. van Zee¹³, F. Walter¹⁴, D.R. Weisz¹², B. Williams⁵, S.-Y. Wu⁴, Y. Wu¹⁵

ABSTRACT

The survey description and the near-, mid-, and far-infrared flux properties are presented for the Local Volume Legacy, a *Spitzer Space Telescope* legacy program built upon a foundation of *GALEX* ultraviolet and ground-based H α imaging of 258 galaxies within 11 Mpc. The Local Volume Legacy (LVL) survey covers an unbiased, representative, and statistically robust sample of nearby star-forming galaxies, exploiting the highest extragalactic spatial resolution achievable with *Spitzer*. As a result of its approximately volume-limited nature, LVL augments previous *Spitzer* observations of present-day galaxies (such as from SINGS, the *Spitzer* Infrared Nearby Galaxies Survey) with improved sampling of the low-luminosity dwarf galaxy population. The collection of LVL galaxies shows a large spread in mid-infrared colors, likely due to the conspicuous deficiency of PAH emission from low-metallicity galaxies. Conversely, the far-infrared tightly tracks the total infrared, with a dispersion in their flux ratio of order 0.1 dex. In terms of the relation between infrared-to-ultraviolet ratio and ultraviolet spectral slope,

¹Department of Physics and Astronomy, University of Wyoming, Laramie, WY 82071; ddale@uwyo.edu

²Astronomy Department, University of Massachusetts, Amherst, MA 01003

³Steward Observatory, University of Arizona, Tucson, AZ 85721

⁴Institute of Astronomy, University of Cambridge, Cambridge CB3 0HA, United Kingdom

⁵Carnegie Observatories, 813 Santa Barbara Street, Pasadena, CA 91101

⁶Department of Astronomy, University of Washington, Seattle, WA 98195

⁷Vatican Observatory Research Group, Steward Observatory, University of Arizona, Tucson, AZ 85721

⁸Departamento de Astrofísica, Universidad Complutense, Madrid, E-28040, Spain

⁹Space Telescope Science Institute, 3700 San Martin Drive, Baltimore, MD 21218

¹⁰Department of Astronomy, Columbia University, New York, NY 10027

¹¹Division of Astronomy and Astrophysics, University of California, Los Angeles, CA 90095

¹²Astronomy Department, University of Minnesota, Minneapolis, MN 55455

¹³Department of Astronomy, Indiana University, Bloomington, IN 47405

¹⁴Max Planck Institut für Astronomie, Königstuhl 17, 69117 Heidelberg, Germany

¹⁵Astronomy Department, Cornell University, Ithaca, NY 14853

the LVL sample is shifted to redder colors than the standard correlation for starburst galaxies. Comparisons with theoretical models suggest that the amplitude of deviations from the starburst relation corresponds to the age of the stellar populations that dominate the ultraviolet/optical luminosities.

Subject headings: surveys — galaxies: photometry — infrared: galaxies

1. Introduction

The goal of the *Spitzer* Local Volume Legacy (LVL) survey¹ is to fill a vital niche in existing multi-wavelength surveys of present-day galaxies with a statistically robust, approximately volume-complete study of our nearest star-forming neighbors. Although star formation rates based on optical spectroscopy as well as *GALEX* ultraviolet and *Spitzer* infrared imaging have been measured for thousands of galaxies (and hundreds of thousands via the Sloan Digital Sky Survey), most currently available datasets are derived from flux-limited samples, and thus suffer from well-known biases against low-mass, low surface brightness systems. Multi-wavelength datasets that do include such systems generally only provide representative samples of this galaxy population (e.g., SINGS; Kennicutt et al. 2003), and are thus not suitable for studies that both seek to probe the low metallicity dwarf galaxy regime and require datasets which are true to the statistics rendered by volume-limited sampling.

With LVL, we have directly addressed this issue by performing the most complete census to-date of dust and star formation within the Local Volume. LVL consolidates and builds upon recent Local Volume galaxy surveys which have acquired ground-based narrowband H α (Kennicutt et al. 2008), *GALEX* ultraviolet (Lee et al. 2009b) and *HST* resolved stellar population imaging (Dalcanton et al. 2009), by collecting *Spitzer* IRAC and MIPS infrared imaging for a complete sample of 258 galaxies derived from these programs. The resultant LVL multi-wavelength dataset provides information on each galaxy’s (i) instantaneous star formation rate, as traced by H α emission, which is produced by the recombination of gas ionized by massive, short-lived OB stars (<20 Myr; Meynet & Maeder 2000), (ii) star formation rate averaged over a longer ~ 100 Myr timescale, as traced by the non-ionizing ultraviolet continuum, which originates in the photospheres of OB stars, (iii) overall stellar mass, from mid-infrared (3.6 and 4.5 μm) luminosities which are generally dominated by the light from old stellar populations, and (iv) dust content, from both the strength and the shape of the infrared emission, which represents the stellar light which has been absorbed and re-radiated by dust. Temporally resolved star formation histories derived from the modeling of stellar population color-magnitude diagrams from *HST* resolved stellar photometry are also available for 69 of the nearer galaxies in the sample. The collection of these observations enable a wealth of spatially-resolved and spatially-integrated studies probing present-day star formation,

¹<http://www.ast.cam.ac.uk/IoA/research/lvls>

chemical abundance, stellar structure, and dust properties as well as galaxy evolution, particularly for metal-poor, low-mass galaxies which dominate the LVL sample by number. As part of the LVL program, we are providing homogeneously processed $H\alpha$, *GALEX* ultraviolet and *Spitzer* IRAC and MIPS infrared images to the community. Public data releases have begun through the NASA/IPAC Infrared Science Archive² (IRSA), with completion of data deliveries expected by the end of 2009.

Principal science issues to be addressed by LVL include: constraining the physical mechanisms underlying dust heating and understanding correlations between infrared emission, dust content, and global galaxy properties; establishing the primary factors which influence polycyclic aromatic hydrocarbon (PAH) emission and evaluating the robustness of PAH emission as a star formation rate indicator, particularly at low metallicities and high specific star formation rates; and probing the temporal variation of star formation as a function of global properties, with special focus on the dwarf galaxy population that dominates the sample (e.g., Lee et al. 2009a). Specific forthcoming papers concentrate on the development of an accurate photometric technique for gauging PAH emission (Marble et al. 2009), the impact of relatively young, luminous AGB stars on stellar masses derived from the near-infrared (Johnson et al. 2009), utilizing ultraviolet-infrared colors to investigate the “inside-out” growth of galaxies (Gil de Paz et al. 2009), a characterization of the population of heavily-obscured star-forming regions (Staudaher et al. 2009), using integrated fluxes to model the spectral energy distributions with the aim of quantifying parameters such as dust mass and temperature, radiation field strength, dust-to-gas ratio, and PAH mass fraction (Gordon et al. 2009; Draine et al. 2009), and combining $H\alpha$ and infrared data to formulate optimal star formation rate indicators. Efforts are also being made to collect new and existing optical *UBVRI* imaging and spectroscopy for the sample, which enable, for example, work updating the local mass/luminosity-metallicity relationship from the *B* to 4.5 μm bands (H. Lee et al. 2009), and stellar energy distribution fitting using stellar population synthesis model grids to provide constraints on star formation histories and present-day stellar masses.

In this paper, we provide a requisite component for much of this work by presenting the *Spitzer* observations, data reduction and IRAC and MIPS infrared flux densities for the LVL sample. Near-infrared photometry measured from 2MASS data within the same apertures that are used on the *Spitzer* imaging are also provided. Section 2 describes the sample, Section 3 reviews the observational and data processing programs, Section 4 covers details of the integrated aperture photometry, Section 5 presents initial results based on the photometry, and Section 6 summarizes our work.

²<http://ssc.spitzer.caltech.edu/legacy/lvlhistory.html>

2. The Sample

The Local Volume Legacy public dataset consists of *GALEX* ultraviolet, $H\alpha$ and *Spitzer* IRAC and MIPS imaging for a tiered sample of 258 galaxies that have been drawn from two existing volume-limited surveys. The inner tier mainly consists of galaxies targeted by ANGST, the ACS Nearby Galaxies Survey Treasury (Dalcanton et al. 2009). This includes all known galaxies within 3.5 Mpc which lie outside the Local Group and the Galactic plane ($|b| > 20^\circ$), as well as galaxies in the M 81 group. ANGST has augmented existing deep *HST* imaging with new observations to provide complete stellar photometry with homogeneous depth for these galaxies. The outer tier is derived from the larger 11 Mpc narrowband $H\alpha$ imaging survey of Kennicutt et al. (2008), and *GALEX* ultraviolet follow-up observations of a sub-sample which avoids the Galactic plane ($|b| > 30^\circ$) (Lee et al. 2009b). The precursor $H\alpha$ survey and the *GALEX* ultraviolet component taken together has been referred to as 11HUGS, the 11 Mpc $H\alpha$ and Ultraviolet Galaxy Survey. The sample as compiled by Kennicutt et al. (2008) is divided into primary and secondary subsets. The primary subset includes galaxies that meet a combined criteria of $D \leq 11$ Mpc, $|b| > 20^\circ$, $m_B < 15$ mag and RC3 type $T \geq 0$ (i.e., galaxies with spiral and irregular morphologies later than S0a). The secondary subset is comprised of galaxies within 11 Mpc for which $H\alpha$ data are available, but fall outside one of the limits in magnitude, Galactic latitude and morphological type, and have available $H\alpha$ data (i.e., galaxies that were either observed as available telescope time allowed, or had existing $H\alpha$ measurements in the literature). The total sample encompasses the majority of the ANGST galaxies, as well as Local Group galaxies not targeted by ANGST. The outer tier of LVL mainly consists of those galaxies in the primary subset, but with more stringent limits on Galactic latitude ($|b| > 30^\circ$, consistent with that applied for *GALEX* follow-up³) and a slightly relaxed brightness limit ($m_B < 15.5$ mag). These bounds represent the ranges beyond which the original surveys that have provided the bulk of our knowledge about the Local Volume galaxy population are known to become severely incomplete (e.g., Tully 1988). Within the bounds, statistical tests and comparison with blind all-sky H I surveys confirm that the sample completeness is excellent ($>95\%$; Lee et al. 2009a). More details on the sample selection and properties of the precursor surveys are given in Dalcanton et al. (2009; ANGST sample definition, *HST* observations and reduction), Kennicutt et al. (2008; 11 Mpc sample compilation, $H\alpha$ observations, and integrated flux and equivalent width catalog), Lee et al. (2007; Local Volume star formation demographics as traced by the $H\alpha$ equivalent width), Lee et al. (2009a; 11 Mpc sample completeness properties) and Lee et al. (2009b; *GALEX* observations and integrated ultraviolet photometry catalog). A schematic illustration of LVL’s tiered volume coverage is shown in Figure 1, and the final LVL sample of 258 galaxies is given in Table 1.

The two tiers of LVL are highly complementary. Figure 2 presents distributions in the primary selection criteria (morphology, apparent B magnitude, Galactic latitude, and distance) for LVL,

³A Galactic latitude limit of $|b| > 30^\circ$ for the ultraviolet observations avoids objects with excess Galactic extinction and high foreground star density which would violate *GALEX*’s bright object safety limits.

where the ANGST sub-sample has been marked separately. Data on these basic properties are taken from the compilations given in Kennicutt et al. (2008) and Dalcanton et al. (2009). ANGST provides complete coverage within an inner volume, and includes both early (dwarf spheroidals, ellipticals, lenticulars) and late (spiral and irregular) morphological types, and many of the lowest mass galaxies. 11HUGS covers a 30 times larger volume, and therefore offers better statistical sampling of the star-forming galaxy population as a whole. As would be expected for an approximately volume-limited sample, the sample population is dominated by low-luminosity, dwarf galaxies. Approximately 61% are irregulars, 31% have spiral morphology, 5% are dwarf spheroidals, and 2% are early-type galaxies. For comparison, the SINGS sample is dominated more by luminous spiral galaxies (63%), with 17% irregular, 12% S0, and 8% elliptical morphologies. While the 11HUGS-based portion of the sample goes as faint as $m_B = 15.5$ mag, as explained above, Figure 2 shows that the faintest systems in the ANGST inner-tier approach $m_B = 19$ mag (e.g., M 81 Dwarf A and BK3N). In terms of their absolute B magnitudes, 81% of the galaxies in LVL are intrinsically fainter than the LMC ($M_B = 17.9$ mag).

The distances in the LVL sample range from 50-60 kpc for the Magellanic Clouds out to 11 Mpc at the outer edge of the survey. Kennicutt et al. (2008) describe in detail the origins of the adopted distances displayed in Figure 2. Many of the galaxies within 5 Mpc have distance determinations based on standard candles, whereas estimates based on secondary indicators or flow-corrected velocities (assuming $H_0 = 75 \text{ km s}^{-1} \text{ Mpc}^{-1}$) are adopted for the more distant systems. About half of the sample galaxies have reliable distances from measurements of the tip of the red giant branch ($\sim 40\%$ of the sample) and Cepheid variables (6% of the sample). Since the inception of the LVL program, four galaxies included in the sample have updated distances which place them outside of 11 Mpc: UGC 00521, UGC 06782, IC 2049, and UGC 7321. This is an inherent difficulty with efforts to construct a volume-limited sample. The membership of the sample will be necessarily fluid until accurate distance and photometric measurements are available for all of the galaxies that are within the volume and around its periphery.

Overall, the LVL sample covers a diverse cross-section of morphologies and star formation properties, and spans a factor of 10^4 in optical luminosity, a factor of 10^5 in star formation rate, and the full range of metallicity found locally (~ 1.5 dex). The nature of the sample allows LVL to more robustly sample infrared properties associated with metal-poor, dwarf galaxies than previous surveys. For example, the plots in Figure 3 show LVL’s coverage of parameter spaces defined by integrated infrared and infrared-to-optical galaxy properties. The 3–1100 μm total infrared (TIR) luminosity is computed from the MIPS 24, 70, and 160 μm fluxes (Equation 4 in Dale & Helou 2002). Also shown are the distributions for SINGS, which was designed to broadly, but not statistically, sample the range of properties in nearby galaxies. While the SINGS survey is slightly biased to cooler far-infrared colors and larger infrared-to-optical ratios, the two surveys dramatically differ in their distributions of total infrared luminosity. As would be expected, LVL is far more effective at filling in the distribution at faint infrared luminosities, whereas SINGS focuses more on infrared-bright and dusty systems.

3. Observational Strategy and Data Processing

LVL *Spitzer* observations build upon IRAC and MIPS archival data which were already available for about a quarter of the sample when the program began. In this section we describe the observational strategy employed for the new IRAC and MIPS infrared data obtained to complete *Spitzer* coverage of the LVL sample, and the archival data that has been reprocessed for inclusion in our dataset.

3.1. New *Spitzer* IRAC 3.6, 4.5, 5.8, and 8.0 μm Data

New *Spitzer* IRAC (Fazio et al. 2004) observations were obtained for 180 LVL galaxies. The IRAC observing strategy follows that of SINGS, which shows that stellar and small grain dust emission is typically detected out to the optical radius at a surface brightness level of $\sim 0.01\text{--}0.1 \text{ MJy sr}^{-1}$ (Regan et al. 2006; Dale et al 2000). For galaxies smaller than the IRAC field of view ($D_{25} \leq 300''$) the Astronomical Observing Requests (AORs) were constructed using four dithered 30 s integrations. For larger galaxies a mosaicking strategy with \sim half-array spatial offsets was used, with the sizes of the mosaic ‘cores’ tailored to the optical size of each galaxy. Two sets of IRAC maps were obtained for each source to enable asteroid removal and to enhance map sensitivity and redundancy. Combining all eight 30 s frames thus results in a net integration per pixel of 240 s (and 120 s around the ~ 2.5 -wide mosaic peripheries). Since each source was observed in all IRAC channels, ample sky coverage is automatically provided by the non-overlapping nature of the two IRAC imagers.

The BCD data used for post-pipeline processing are from the S18 pipeline version. The multi-epoch, multiple-pointing IRAC observations for each galaxy are combined into one single mosaic for each band using the MOPEX mosaicking software. Additional post-BCD processing includes: distortion corrections, rotation of the individual frames (for multi-epoch observations), bias structure and bias drift corrections, image offset determinations via pointing refinements from the SSC pipeline (MOPEX’s default), detector artifact removal, constant-level background subtraction, and image resampling to $0''.75$ pixels using drizzling techniques. The drizzling slightly improves the final PSF over the native one; the full-width half maxima are $\sim 1''.6$ in the shorter wavelength channels and $\sim 1''.9$ at $8 \mu\text{m}$. The final images are in units of MJy sr^{-1} and have the average sky level removed; sky values are estimated via several “blank” regions located near but beyond the target galaxy emission. Though the LVL IRAC data processing is built upon MOPEX while the SINGS project developed their own IRAC data processing package, the nature of the final data products in the two surveys are essentially the same.

In cases where exceptionally bright target sources saturated or entered the non-linear regime of the detector during the 30 second exposure, additional 1.2 s images are used to allow for recovery of this information. Pixels affected by these issues, typically in the 5.8 and $8.0 \mu\text{m}$ frames, are flagged by MOPEX during processing. The correction begins by creating a mosaic of the 1.2 s

exposures interpolated onto the same pixel grid as the original mosaic. A difference image is then created from the two mosaics and any residual, systematic difference in the background sky levels is removed. Pixels in the difference image valued at 1 MJy sr^{-1} or higher are flagged (routinely regions of ~ 400 contiguous pixels) and these pixels in the long integration mosaic are replaced by their short integration counterparts. The nuclear regions for the following galaxies were affected by saturation: NGC 0253, NGC 2903, NGC 3031, NGC 3034 (at all IRAC wavelengths), NGC 3351, NGC 3593, NGC 3627, NGC 4258, NGC 5195, and NGC 5253.

3.2. New *Spitzer* MIPS 24, 70, and 160 μm Data

New *Spitzer* MIPS (Rieke et al. 2004) observations were obtained for 201 LVL galaxies. Galaxies were imaged in all three MIPS bands centered at 24, 70, and 160 μm , using the highly successful scan mapping strategy employed in the SINGS project. The scan mode was used even on galaxies small enough to fit within the array field of view, because achieving adequate background measurements for extended targets in photometry mode is less efficient than the scan mode. Each map was executed at the medium scan rate, and includes multiple scan legs tailored to the size of the galaxy and half-array offsets between scan legs. Each galaxy was mapped twice, with the maps separated by 10-40 days to allow time for the field-of-view to rotate and for asteroids to move out of the field. This second map was performed in the reverse direction (the “backward mapping” mode), with offsets in the cross-scan and in-scan directions. Taken together, these mapping strategies ensure that each point on the galaxy is scanned over in two different directions, which aids reduction of array artifacts on both Si:As and Ge:Ga arrays. The in-scan offset ensures that Ge:Ga stimflashes do not occur at the same point in both maps and thereby improves the calibration. The integration time per point is 160, 80, and 16 s at 24, 70, and 160 μm , respectively.

The MIPS images are processed with the MIPS Data Analysis Tool (DAT; Gordon et al. 2005), supplemented by custom scripts for the specific data reduction and mosaicking of extended sources. The latter include at 24 μm : readout offset correction, array-averaged background subtraction, and exclusion of the first five images in each scan leg due to boost frame transients. At 70 and 160 μm , the custom scripts include a pixel-dependent background subtraction for each map to remove residual detector drifts and background cirrus and zodiacal emission. This method of reduction was used for all the SINGS galaxies as well as very large galaxies (M 31, M 33, M 101, SMC, LMC, etc.). The resulting PSFs have full-width half maxima of ~ 6 , 18, and $40''$ at 24, 70, 160 μm , respectively. The pixel scales of the MIPS mosaics are $1''.5$, $4''.5$, and $9''.0$ at 24, 70, and 160 μm , respectively.

Finally, a correction for 70 μm non-linearity effects is included in the data processing. A correction of the form

$$f_{\text{true}}^{70\mu\text{m}} = 0.502(f_{\text{measured}}^{70\mu\text{m}})^{1.182}, \quad (1)$$

derived from data presented by Gordon et al. (2009) and slightly different than the form first

presented in Dale et al. (2007) for SINGS galaxies, is applied to pixel values above a threshold of $\sim 44 \text{ MJy sr}^{-1}$. A small fraction of the pixels in a total of 40 LVL $70 \mu\text{m}$ images require such a correction. The median correction to the global $70 \mu\text{m}$ flux density for these 40 galaxies is only a few percent.

3.3. Archival *Spitzer* Data

Archival IRAC and MIPS data, with spatial coverage and sensitivity similar to or greater than that described in § 3.1 and § 3.2, are utilized for 78 (IRAC) and 57 (MIPS) galaxies. No new IRAC or MIPS observations were obtained for these subsets of the LVL sample. The data processing procedures for the archival data are the same as those followed for the new observations described above, except for the asteroid rejection in the few cases where only one epoch was measured. Table 2 indicates for which galaxies we utilize archival *Spitzer* data.

4. Aperture Photometry

This section describes the infrared data collected for the LVL program. Table 2 presents the global flux densities for the entire LVL sample, for wavelengths spanning the near- to far-infrared. The data are corrected for Galactic extinction (Schlegel, Finkbeiner, & Davis 1998) assuming $A_V/E(B - V) \approx 3.1$ and the reddening curve of Li & Draine (2001). The effect of airmass has been removed from the ground-based near-infrared fluxes. Additional issues such as sky removal, aperture corrections, and upper limits are covered in detail below.

4.1. 2MASS Near-Infrared JHK_s Photometry

The Two Micron All Sky Survey (2MASS) obtained data for the entire sky at 1.25, 1.65, and $2.17 \mu\text{m}$ using two automated, ground-based 1.3 m telescopes (Skrutskie et al. 2006). Galaxy photometry is available from the 2MASS Extended Source Catalog for over a million galaxies and from the 2MASS Large Galaxy Atlas for several hundred galaxies larger than $1'$ (Jarrett et al. 2003). Integrated fluxes for several LVL galaxies were adopted from the Large Galaxy Atlas, and these are generally consistent with expectations based on IRAC 3.6 and $4.5 \mu\text{m}$ fluxes and simple stellar model extrapolations to 2MASS wavelengths. However, most LVL galaxies do not appear in the Large Galaxy Atlas, and for these relatively faint systems many of the fluxes from the Extended Source Catalog are 0.5–2 mag low based on similar extrapolations from IRAC 3.5 and $4.5 \mu\text{m}$ data. We find that when Extended Source Catalog fluxes appear unexpectedly faint, it is typically due to the comparatively small apertures used in the automated 2MASS extraction (see, for example, the case of UGC 08245 in Figure 4). Hence we have extracted 2MASS fluxes for the vast majority of the LVL sample using the same apertures and foreground star removals used to determine IRAC and

MIPS fluxes, as discussed in the following section. Figure 5 displays the ratios of our near-infrared extractions with those provided in the 2MASS Extended Source Catalog. Included in the figure are results from Kirby et al. (2008) based on deep H band imaging of nearby galaxies with the 3.9 m Anglo-Australian Telescope; Kirby et al. (2008) likewise find that Extended Source Catalog extractions are 0.5–2 mag too faint.

4.2. *Spitzer* 3.6, 4.5, 5.8, 8.0, 24, 70, and 160 μm Photometry

4.2.1. *Foreground Star and Background Galaxy Removal*

The presence of foreground stars and background galaxies can significantly affect the global infrared fluxes for some galaxies, particularly the fainter dwarfs and galaxies at low Galactic latitudes. Once identified, the foreground stars and background galaxies are removed through a simple interpolation of the local sky from the images using the IRAF task *IMEDIT*. Our procedure for identifying these sources relies on a multi-wavelength analysis (3.6, 8.0, 24 μm , and $H\alpha$), looking for objects $H\alpha$ -rich or especially blue (foreground stars; $f_\nu(3.6)/f_\nu(8.0) > 8$), or small red systems with galaxy-like morphologies. Archival *Hubble Space Telescope* imaging was also inspected for obvious background galaxy or foreground stellar identifications, when available. When uncertain about the identification of a particular source, we opted to err on the conservative side and allow such sources to remain in the global flux extraction. However, these sources of uncertain origin are typically very faint and negligibly impact global flux extractions. The median ratios of edited-to-unedited fluxes is [0.854, 0.846, 0.939, 0.971, 0.980, 1.00, 1.00] at [3.6, 4.5, 5.8, 8.0, 24, 70, 160] μm ; very few significant corrections are made at 24, 70, and 160 μm .

The uncertainties provided in Table 2 include both calibration and statistical uncertainties. Calibration uncertainties are 5–10% for IRAC 3.6 and 4.5 μm data, and 10–15% for IRAC 5.8 and 8.0 μm data; 10% IRAC calibration uncertainties are used in Table 2. MIPS calibration uncertainties are 4%, 7%, and 12% respectively at 24, 70, and 160 μm (Engelbracht et al. 2007, Gordon et al. 2007, and Stansberry et al. 2007).

4.2.2. *Aperture Corrections*

For a given galaxy, the same aperture was used for extracting all IRAC and MIPS fluxes. Elliptical apertures for IRAC and MIPS photometry were based on capturing all the galaxy emission visible for all IRAC and MIPS images. Typically this means that the 3.6 μm image was used to create the aperture, since *Spitzer* is most sensitive at 3.6 μm and that is the *Spitzer* wavelength at which stars are brightest.

Since the IRAC flux calibration is based on point source photometry for a 12'' radius aperture, the fluxes for all extended sources and aperture radii $\neq 12''$ need to have an additional correction

applied. These corrections account for the “extended” emission due to the wings of the PSF and also for the scattering of the diffuse emission across the IRAC focal plane. This photometric correction is different than merely subtracting off the sky value (§ 3.1). As described in Dale et al. (2007), the IRAC extended source correction has been derived for a variety of source morphologies and extents. For an effective aperture radius $r = \sqrt{ab}$ in arcseconds derived from the semi-major a and semi-minor b ellipse axes provided in Table 2, the IRAC extended source aperture correction is

$$f_{\text{true}}^{\text{IRAC}} / f_{\text{measured}}^{\text{IRAC}} = Ae^{-r^B} + C, \quad (2)$$

where A , B , and C are listed in Table 3⁴. The median IRAC extended source aperture corrections are [0.914, 0.941, 0.826, 0.756] at [3.6, 4.5, 5.8, 8.0] μm .

In contrast to the IRAC aperture corrections, the main reason MIPS aperture corrections are needed is due to the smearing of light outside the aperture. MIPS aperture corrections are empirically determined from a comparison of fluxes from smoothed and unsmoothed 3.6 μm imaging, an approximate proxy for tracing the MIPS galaxy morphologies. The aperture correction for a given MIPS flux is the ratio of the fluxes from the unsmoothed 3.6 μm image to the flux from the 3.6 μm image smoothed to the same PSF as the MIPS image in question. The median MIPS aperture corrections are [1.01, 1.01, 1.03] at [24, 70, 160] μm , and the most significant corrections are [1.09, 1.12, 1.42] for CGCG 269-049.

4.3. Upper Limits

Many of the optically-faint galaxies in the sample are frequently undetected in the infrared, particularly at wavelengths of 5.8 μm and longer. Upper limits are included in Table 2 for sources undetected by infrared imaging. The 3σ upper limits for *Spitzer* imaging are derived according to

$$f_{\nu}(3\sigma \text{ upper limit}) = 3 \sigma_{\text{sky}} \Omega_{\text{pix}} \sqrt{N_{\text{pix}} + N_{\text{pix}}^2 / N_{\text{sky}}} \approx 3 \sigma_{\text{sky}} \Omega_{\text{pix}} \sqrt{2N_{\text{pix}}} \quad (3)$$

where σ_{sky} is the sky surface brightness fluctuation per pixel (MJy sr^{-1}), Ω_{pix} the solid angle subtended per pixel, N_{pix} the number of pixels in the galaxy aperture, and N_{sky} the number of pixels in the sky aperture. The parameter σ_{sky} is approximately 0.02, 0.03, 0.11, 0.12, 0.2, 0.9, 1.7 MJy sr^{-1} at 3.6, 4.5, 5.8, 8.0, 24, 70, and 160 μm , respectively. A similar computation for 2MASS near-infrared upper limits is carried out after converting that survey’s mean 10σ point source sensitivities (~ 16.4 , 15.5, and 14.8 mag for J , H , and K_s , respectively; Skrutskie et al. 2006) to 3σ values and accounting for the difference in the $4''$ radius 2MASS point source aperture and the LVL galaxy apertures.

⁴See <http://ssc.spitzer.caltech.edu/irac/calib/extcal/>

5. Results

5.1. Detection Rate

The lower panels of Figure 6 display the detection rates for the different *Spitzer* imaging channels as a function of *B* band apparent and absolute magnitudes. Nearly all galaxies are detected at all *Spitzer* wavelengths down to $m_B \approx 14$ mag and $M_B \approx -13$ mag. Consistent with our pre-survey expectations, the $m_B \sim 15.5$ mag cut-off for the outer tier of the sample that extends to 11 Mpc (see § 2) proved to be a useful sample selection criterion, as very few MIPS detections are available fainter than this magnitude limit. The inner tier/ANGST portion of the sample extends the sample to much fainter levels, as faint as $m_B \approx 19$ mag in the cases of BK03N and M 81 Dwarf A. As expected for the optically-faint galaxies, the highest detection rates are found for the stellar-dominated 3.6 and 4.5 μm channels, while the 70 and 160 μm imaging proved to be far more challenging to convincingly detect cold dust emission. A stacking analysis (e.g., Dole et al. 2006) could be employed to obtain a better statistical understanding of the fainter galaxy population at long wavelengths.

5.2. Comparison with Data from *IRAS*

Secure flux measurements are available at all *IRAS* and MIPS wavelengths for a subset of 66 LVL galaxies. The *IRAS* data are compiled from Rice et al. (1988), Moshir et al. (1990), Sanders et al. (2003), Lisenfeld et al. (2007), and our own archival extractions. Figure 7 provides a comparison of MIPS 24 μm and *IRAS* 25 μm data, and the 3–1100 μm total infrared as measured by MIPS and *IRAS* using the *TIR* equations provided in Dale & Helou (2002). The agreement between 24 and 25 μm fluxes is excellent: $\nu f_\nu(24\mu\text{m})/\nu f_\nu(25\mu\text{m}) = 1.02$ with a dispersion of 25%. The ratio of MIPS- and *IRAS*-based total infrared measures has a similar scatter (21%), but the average ratio is 1.17. These findings are similar to those by Kennicutt et al. (2009) for a sample of 205 nearby galaxies with both *IRAS* and MIPS data. The righthand panel in Figure 7 includes semi-empirical predictions from models of infrared spectral energy distributions. Part of the systematic offset in $TIR_{\text{MIPS}}/TIR_{\text{IRAS}}$ can be attributed to the relative inability of *IRAS* to accurately measure the total infrared for cold galaxies, galaxies for which the bulk of the infrared emission peaks beyond 100 μm .

5.3. Multi-Wavelength Spectral Energy Distributions

Figures 8 and 9 show ultraviolet- $\text{H}\alpha$ -infrared mosaics of NGC 5236 and UGC 05829, spanning wavelengths where the emission is dominated by young stars (0.15 μm), H II regions ($\text{H}\alpha$), old stars (3.6 μm), PAHs (8.0 μm), very small grains (24 μm) and large grains (70 μm). The galaxies and wavelengths displayed in these two figures highlight the broad range of environments and galaxies

sampled by the LVL survey (see § 2). Figure 10 provides the panchromatic ultraviolet-infrared broadband spectral energy distributions for all 258 galaxies.⁵ The solid curve is the sum of a dust (dashed) and a stellar (dotted) model. The dust curve is a Dale & Helou (2002) model (least squares) fitted to ratios of the observed 24, 70, and 160 μm fluxes, and then scaled to match the overall infrared brightness. The α_{SED} listed within each panel parameterizes the distribution of dust mass as a function of heating intensity, as described in Dale & Helou (2002). To quantify the uncertainty on α_{SED} displayed within each panel of Figure 10, 1,000 Monte Carlo simulations of the fit to each galaxy’s far-infrared fluxes are performed, utilizing the tabulated flux uncertainties to add a random (Gaussian deviate) flux offset at each MIPS wavelength. The α_{SED} uncertainties reflect the standard deviations in the simulations. The stellar curve is a 1 Gyr continuous star formation, solar metallicity curve from Vazquez & Leitherer (2005) fitted to the 2MASS data. The initial mass function for this curve utilizes a double power law form, with $\alpha_{1,\text{IMF}} = 1.3$ for $0.1 < m/M_{\odot} < 0.5$ and $\alpha_{2,\text{IMF}} = 2.3$ for $0.5 < m/M_{\odot} < 100$ (e.g., Kroupa 2002). Though this stellar curve is not adjusted for internal extinction and may not be applicable to many galaxies in the sample, it is included as a fiducial reference against which deviations in the ultraviolet can be compared from galaxy to galaxy.

The spectral energy distributions for the LVL sample range widely. There are stellar-dominated (NGC 0404, UGC 05373, UGCA 0193) and comparatively dusty (IC 5256, NGC 6503) systems; for sources detected by MIPS, the infrared-to-far-ultraviolet ratio in the sample spans more than three orders of magnitude, from 0.1 to over 100 (§ 5.5). There are galaxies with far-infrared spectral energy distributions indicative of warm (UGCA 0281) and cold dust grains (NGC 5055). Compared to what would be expected based on their stellar and far-infrared emission, many galaxies show a dearth of emission from PAHs in the 8.0 μm band (e.g., ESO 245-G005, UGC 01249, UGC 05272). The variations in global spectral energy distributions are discussed in more detail below.

5.4. Infrared Colors

The IRAC–MIPS infrared colors for the LVL sample are displayed in Panel a of Figure 11. The $f_{\nu}(70\mu\text{m})/f_{\nu}(160\mu\text{m})$ ratio typically traces the temperature of large interstellar grains, while the $f_{\nu}(8.0\mu\text{m})/f_{\nu}(24\mu\text{m})$ ratio has several influences. The flux at 24 μm mostly represents emission from very small grains (grains with effective radii of 15–40 Å; Draine & Li 2007), and the flux at 8.0 μm can have contributions from stars, hot dust, PAHs, and AGN. Perhaps due to the diversity of emission mechanisms responsible for 8.0 and 24 μm flux levels, the $f_{\nu}(8.0\mu\text{m})/f_{\nu}(24\mu\text{m})$ ratio spans two orders of magnitude compared to the single factor of ~ 10 stretch in the the $f_{\nu}(70\mu\text{m})/f_{\nu}(160\mu\text{m})$ ratio. Since the LVL sample largely lacks “strong” AGN, loosely defined here as AGN that dominate

⁵The far- and near-ultraviolet data are from images acquired as part of the *GALEX* Nearby Galaxy Survey, Medium Imaging Survey, and All-Sky Imaging Survey along with several Guest Investigator programs including the 11HUGS Cycle 1 and ANGST Cycle 3 proposals (Lee et al. 2009b).

a galaxy’s emission over substantial portions of the electromagnetic spectrum, it is unlikely that AGN contribute much to the scatter in Figure 11.

The (42–122 μm) far-infrared (*FIR*) and total infrared are frequently used as indications of the star formation rate in galaxies (Kennicutt 1998; Bell 2003). However, in many instances the far-infrared continuum is unavailable or not detected, so monochromatic infrared proxies for *FIR* or *TIR* are occasionally employed (e.g., Papovich & Bell 2002; Bavouzet et al. 2008). Hence, the tightness (dispersion) in monochromatic-to-bolometric ratios are of general interest. Five flavors of these ratios are displayed in the remaining panels of Figure 11, and a tabulation of median LVL infrared colors and monochromatic-to-bolometric infrared ratios can be found in Table 4 along with their dispersions. Panel b of Figure 11 shows the distribution of the 8.0 μm emission with respect to the 3–1100 μm total infrared, a distribution which exhibits a dispersion of 0.23 dex, similar to that for $f_\nu(70\mu\text{m})/f_\nu(160\mu\text{m})$ and $f_\nu(8.0\mu\text{m})/f_\nu(24\mu\text{m})$. While it is evident that the LVL sample is distributed fairly evenly by morphology across $f_\nu(70\mu\text{m})/f_\nu(160\mu\text{m})$ ratios, the bulk of the systems exhibiting relatively low $f_\nu(8.0\mu\text{m})/f_\nu(24\mu\text{m})$ and $\nu f_\nu(8.0\mu\text{m})/TIR$ ratios are from late-type spirals and irregulars.

The preponderance of late-type spirals and irregulars showing relatively low 8.0 μm emission is amplified when “dust-only” 8.0 μm emission is considered. Panel e of Figure 11 shows a plot similar to that in Panel b but with the stellar emission removed using the expression presented in Helou et al. (2004):

$$\nu f_\nu(8.0\mu\text{m})_{\text{dust}} = \nu f_\nu(8.0\mu\text{m}) - \eta^{8*} \nu f_\nu(3.6\mu\text{m}) \quad (4)$$

where $\eta^{8*} = 0.232 \times 3.6/8.0$. The dispersion (0.44 dex) and overall range are significantly larger when the dust-only 8.0 μm emission is normalized to the total infrared. It is possible that a portion of these increases in dispersion and range are due to the inapplicability of Equation 4 to late-type spirals, but it should be noted that Equation 4 is based on a detailed analysis of NGC 300, a local system with an Sd morphological classification. Another possibility is that the late-type spirals and irregulars within LVL are on average less abundant in heavy metals, and thus either the formation of PAH molecules is starved or the relatively fragile PAHs are photo-dissociated in the hard radiation fields typically associated with low-metallicity environments (Engelbracht et al. 2005; Madden et al 2006; Wu et al. 2006; Dale et al. 2009; Sloan et al. 2008). Additional data and detailed follow-up utilizing LVL metallicities would be required to address this issue.

In contrast to the 8.0 μm -to-*TIR* measures, the $\nu f_\nu(24\mu\text{m})/TIR$ ratio (Panel d of Figure 11) shows a range less than an order of magnitude and a dispersion of 0.15 dex; the 70 μm -to-*TIR* and 160 μm -to-*TIR* ratios have even smaller dispersions (Panels c & f and Table 4). The implication is that, compared to the 8.0 μm emission from galaxies, the infrared emission from very small grains at 24 μm and from large grains at 70 and 160 μm are far more tightly coupled to the bolometric infrared emission. Such a conclusion may naturally arise from inspection of the global spectral energy distributions in Figure 10, but it is nonetheless important to emphasize the differences between what is being emitted in the mid-infrared versus the far-infrared. This result conceptually follows work by Calzetti et al. (2007) and Kennicutt et al. (2007; 2009), who show that 24 μm and

total infrared fluxes are more effective than $8.0\ \mu\text{m}$ fluxes at tracing a galaxy’s current star formation rate (they also show that these infrared fluxes correlate even better with star formation, to within ~ 0.1 dex, if they are coupled with $\text{H}\alpha$ to capture the unobscured portion of star formation).

The $70\ \mu\text{m}$ -to- TIR and $160\ \mu\text{m}$ -to- TIR cling remarkably closely to the model SED predictions, with dispersions of 0.038 and 0.031 dex, respectively. However, there is evidence for a slightly increasing mismatch between model and data at the warmest far-infrared colors. This inconsistency presumably reflects the paucity of galaxies with extremely high star formation rates in the sample used to construct the models (see Dale et al. 2000).

5.5. The Infrared-to-Ultraviolet Ratio and Ultraviolet Spectral Slope

The infrared-to-ultraviolet ratio is a coarse measure of dust extinction in the ultraviolet, and thus should be related to the amount of reddening in ultraviolet spectra. Indeed, starbursting galaxies follow a tight correlation between the ratio of infrared-to-ultraviolet emission and the ultraviolet spectral slope (e.g., Calzetti et al. 1994; Calzetti et al. 1997; Meurer et al. 1999). Compared to the relation defined by starbursts, normal star-forming galaxies are offset to redder ultraviolet spectral slopes, exhibit lower infrared-to-ultraviolet ratios, and show significantly larger scatter (Buat et al. 2002, 2005; Bell 2002; Kong et al. 2004; Gordon et al. 2004; Burgarella et al. 2005; Calzetti et al. 2005; Seibert et al. 2005; Cortese et al. 2006; Boissier et al. 2007; Gil de Paz et al. 2007; Dale et al. 2007). Offsets from the locus formed by starbursting and normal star-forming galaxies can be particularly pronounced for systems lacking significant current star formation, such as elliptical galaxies, systems for which the luminosity is more dominated by a passively evolving older, redder stellar population. The LVL survey provides a unique sample for exploring the relationship between the infrared-to-ultraviolet ratio and the ultraviolet slope, as it consists of a statistically complete set of star-forming galaxies, approximately half of which are dwarf/irregular systems.

Figure 12 displays the LVL infrared-to-ultraviolet ratios as a function of the ultraviolet spectral slope. As expected, the well-known starbursts in the LVL sample lie close to the starburst curve: NGC 0253, NGC 4631, NGC 4449, NGC 1705, and NGC 4736, with the latter formally known as a post-starburst galaxy (Walker, Lebofsky, & Rieke 1988). Overall, the LVL population is broadly segregated in the infrared-to-ultraviolet ratio according to optical morphology, with Sb and earlier-type galaxies showing relatively high values, Sc/Sd/Sm systems exhibiting intermediate values, and irregulars appearing near the bottom of the diagram. To explore this distribution further, in Figure 13 we plot two observable tracers of the “birthrate parameter” as a function of the (perpendicular) distance to the starburst curve in Figure 13. Following Carlos-Muñoz et al. (2009), the ratio of far-ultraviolet-to-near-infrared luminosity is used as a measure of the ratio of past-to-present star formation, sometimes referred to as the birthrate parameter (see also, for example, Boselli et al. 2001; Cortese et al. 2006). This ratio represents the birthrate parameter since the far-ultraviolet traces star formation over 100 Myr timescales whereas the near-infrared probes the

total stellar mass built up over much longer timescales. Here the far-ultraviolet emission is corrected for extinction using the infrared-to-ultraviolet-based recipe formulated in Buat et al. (2005). The distribution of far-ultraviolet extinctions estimated by this method is provided in Figure 14. Ninety percent of the sources have far-ultraviolet extinctions less than 1.7 mag, or equivalently, ninety percent have optical extinctions $A_V \lesssim 0.6$ mag using the Li & Draine (2001) extinction curve. The bottom panel of Figure 13 incorporates an observable indicator of the birthrate parameter that is much less affected by extinction: the $H\alpha$ equivalent width (taken from Kennicutt et al. 2008). This parameter is also a measure of the birthrate, since the $H\alpha$ flux is a measure of H II line emission primarily produced by massive ($> 10 M_\odot$) stars on ~ 3 –20 Myr timescales (e.g., Kennicutt 1998; Meynet & Maeder 2000) while the red continuum emission near 6563 Å that provides the normalization for the equivalent width traces the total mass of stars built up over much longer timescales.

Both panels of Figure 13 show a clear trend, with lower birthrate systems exhibiting larger distances from the starburst trend, consistent with the study of Kong et al (2004). The deviations from the starburst curve are presumably driven by the differential effects young and old stellar populations and their local dust opacities have on the intrinsic and dust-reddened luminosities, suggesting that a galaxy’s star formation history plays an important role in determining its location within Figure 12. To more directly interpret these deviations from the starburst curve as a function of the age of the stellar population, the righthand axis of the upper panel of Figure 13 is quantified according to the age inferred from theoretical spectra. This comparison is accomplished by convolving *GALEX* far-ultraviolet and *Spitzer* 3.6 μm filter transmission profiles with stellar spectra similar to those described in § 5.3 but for a wide range of ages (1 Myr to 10 Gyr). The ages for the respective simulated spectra are shown along the righthand axis at levels corresponding to the computed theoretical far-ultraviolet-to-near-infrared ratios along the lefthand axis. Assuming these theoretical spectra are broadly applicable to the LVL sample, the star formation timescales range from several million years up to a few billion years, with the longest-lasting star formation episodes corresponding to the largest deviations from the starburst curve. It should be stressed that this comparison with theoretical stellar population ages is indicative—if the actual star formation rates have been declining with time instead of remaining constant, then the age axis in Figure 13 overestimates the true ages.

6. Summary

In this contribution we describe the Local Volume Legacy, a *Spitzer Space Telescope* infrared imaging program built upon a foundation of *GALEX* ultraviolet and ground-based $H\alpha$ imaging of 258 galaxies within 11 Mpc, two-thirds of which are irregulars or dwarf spheroidals. The proximity and nearly volume-limited nature of the survey are key aspects to this program, enabling multi-wavelength analyses of star formation with high spatial resolution in a manner that is statistically representative of the nearby galaxy population. First results based primarily on the infrared data

are reported here. Whereas monochromatic tracers of the far-infrared at 70 and 160 μm closely track the 3-1100 μm total-infrared emission, the mid-infrared-to-total-infrared ratios show large dispersions. The large scatter in comparing dust emission at 8.0 μm and total dust emission is likely due to the notable deficiency of PAH emission from the low-metallicity galaxies prevalent in the LVL survey. The LVL sample shows a correlation between infrared-to-ultraviolet ratio and ultraviolet spectral slope, but it is shifted to redder colors than what is seen for starbursting galaxies and most star-forming galaxies. Theoretical models are utilized to buttress the idea that deviations from the starburst relation correspond to the age of the stellar population.

Support for this work, part of the *Spitzer Space Telescope* Legacy Science Program, was provided by NASA through Contract Number XXX issued by the Jet Propulsion Laboratory, California Institute of Technology under NASA contract 1407. This research has made use of the NASA/IPAC Extragalactic Database which is operated by JPL/Caltech, under contract with NASA. This publication makes use of data products from the Two Micron All Sky Survey, which is a joint project of the University of Massachusetts and the Infrared Processing and Analysis Center/California Institute of Technology, funded by the National Aeronautics and Space Administration and the National Science Foundation. IRAF, the Image Reduction and Analysis Facility, has been developed by the National Optical Astronomy Observatories and the Space Telescope Science Institute. We gratefully acknowledge NASA’s support for construction, operation, and science analysis for the GALEX mission, developed in cooperation with the Centre National d’Etudes Spatiales of France and the Korean Ministry of Science and Technology.

REFERENCES

- Bavouzet, N., Dole, H., Le Floch, E., Caputi, K.I., Lagache, G., & Kochanek, C.S. 2008, *A&A*, 479, 83
- Bell, E.F. 2002, *ApJ*, 577, 150
- Bell, E.F. 2003, *ApJ*, 586, 794
- Bernard, J.-P. et al. 2008, *AJ*, 136, 919
- Boissier, S. et al. 2007, *ApJS*, 173, 524
- Boselli, A., Gavazzi, G., Donas, J., & Scodeggio, M. 2001, 121, 753
- Buat, V. et al. 2001, *ApJ*, 619, L51
- Buat, V., Boselli, A., Gavazzi, G., & Bonfanti, C. 2002, *A&A*, 383, 801
- Buat, V. et al. 2005, *ApJ*, 619, L51

- Burgarella, D., Buat, V., & Iglesias-Páramo, J. 2005, MNRAS, 360, 1413
- Calzetti, D. 1995, Bohlin, R.C., Kinney, A.L., Storchi-Bergmann, T., & Heckman, T.M. 1995, ApJ, 443, 136
- Calzetti, D. 1997, AJ, 113, 162
- Calzetti, D. et al. 2005, ApJ, 633, 871
- Calzetti, D. et al. 2007, ApJ, 666, 870
- Carlos-Muñoz, J. et al. 2009, in preparation
- Cortese, L., Boselli, A., Buat, V., Gavazzi, G., Boissier, S., Gil de Paz, A., Seibert, M., Madore, B.F., & Martin, C. 2006, ApJ, 637, 242
- Cortese, L., 2006, ApJ, 636, 242
- Dalcanton, J. et al. 2009, ApJ, in press
- Dale, D.A. et al. 2000, AJ, 120, 583
- Dale, D.A., Helou, G., Contursi, A., Silbermann, N.A., & Kolhatkar, S. 2001, ApJ, 549, 215
- Dale, D.A. & Helou, G. 2002, ApJ, 576, 159
- Dale, D.A. et al. 2007, ApJ, 655, 863
- Dale, D.A. et al. 2009, ApJ, in press
- Dole, H. et al. 2006, A&A, 451, 417
- Draine, B.T., & Li, A. 2007, ApJ, 657, 810
- Draine, B.T. et al. 2009, in preparation
- Engelbracht, C.W., Gordon, K.D., Rieke, G.H., Werner, M.W., Dale, D.A., & Latter, W.B. 2005, ApJ, 628, L29
- Engelbracht, C.W. et al. 2007, PASP, 119, 914
- Fazio, G.G. et al. 2004, ApJS, 154, 10
- Gil de Paz, A. et al. 2007, ApJS, 173, 185
- Gil de Paz, A. et al. 2009, in preparation
- Gordon, K. et al. 2004, ApJS, 154, 215
- Gordon, K. et al. 2005, PASP, 117, 503

- Gordon, K. et al. 2007, PASP, 119, 1019
- Gordon, K. et al. 2009, in preparation
- Helou, G. et al. 2004, ApJS, 154, 253
- Jarrett, T.H., Chester, T., Cutri, R., Schneider, S.E., & Huchra, J.P. 2003, AJ, 125, 525
- Johnson, B. et al. 2009, in preparation
- Kennicutt, R.C. 1998, ARA&A, 36, 189
- Kennicutt, R.C. et al. 2003, PASP, 115, 928
- Kennicutt, R.C. et al. 2007, ApJ, 671, 333
- Kennicutt, R.C., Lee, J.C., Funes, J.G., Sakai, S., & Akiyama, S. 2008, ApJS, 178, 247
- Kennicutt, R.C. et al. 2009, ApJ, submitted
- Kirby, E.M., Jerjen, H., Ryder, S.D., & Driver, S.P. 2008, AJ, 136, 1866
- Kong, X., Charlot, S., Brinchmann, J., & Fall, S.M. 2004, MNRAS, 349, 769
- Kroupa, P. 2002, Science, 295, 82
- Lee, J.C. 2006, Ph.D. thesis, University of Arizona
- Lee, J.C., Kennicutt, R.C., Funes, J.G., Sakai, S., & Akiyama, S. 2007, ApJ, 671, 113
- Lee, J.C., Kennicutt, R.C., Funes, J.G., Sakai, S., & Akiyama, S. 2009a, ApJ, in press
- Lee, J.C. et al. 2009b, in preparation
- Leroy, A., Bolatto, A., Stanimirovic, S., Mizuno, N., Israel, F., & Bot, C. 2007, ApJ, 658, 1027
- Li, A. & Draine, B.T. 2001, ApJ, 554, 778
- Lisenfeld, U. 2007, A&A, 462, 507
- Madden, S.C., Galliano, F., Jones, A.P., & Sauvage, M. 2006, A&A, 446, 877
- Marble, A.R.. et al. 2009, in preparation
- Meurer, G.R., Heckman, T.M., & Calzetti, D. 1999, ApJ, 521, 64
- Meynet, G. & Maeder, A. 2000, A&A, 361, 101
- Moshir, M. et al. 1990, IRAS Faint Source Catalog, version 2.0
- Papovich, C. & Bell, E.F. 2002, ApJ, 579, L1

- Regan, M. et al. 2006, *ApJ*, 652, 1112
- Rice, W., Lonsdale, C.J., Soifer, B.T., Neugebauer, G., Kopan, E.L., Lloyd, L.A., de Jong, T., & Habing, H.J. 1988, *ApJS*, 68, 91
- Rieke, G.H. et al. 2004, *ApJS*, 154, 25
- Ryan-Weber, E. et al. 2002, *AJ*, 124, 1954
- Sanders, D.B., Mazzarella, J.M., Kim, D.-C., Surace, J.A., & Soifer, B.T. 2003, *AJ*, 126, 1607
- Schlegel, D.J., Finkbeiner, D.P., & Davis, M. 1998, *ApJ*, 500, 525
- Seibert, M. et al. 2005, *ApJ*, 619, L55
- Sloan, G.C., Kraemer, K.E., Wood, P.R., Zijlstra, A.A., Bernard-Salas, J., Devost, D., & Houck, J.R. 2008, *ApJ*, 686, 1056
- Skrutskie, M.F. et al. 2006, *AJ*, 131, 1163
- Stansberry, J.A. et al. 2007, *PASP*, 119, 1038
- Staudaher, S. et al. 2009, in preparation
- Tully, R.B. 1988, *AJ*, 96, 73
- Walker, C.E., Lebofsky, M.J., & Rieke, G.H. 1988, *ApJ*, 325, 687
- Wu, Y., Charmandaris, V., Hao, H., Brandl, B.R., Bernard-Salas, J., Spoon, H.W.W., & Houck, J.R. 2006, *ApJ*, 639, 157
- Vazquez, G.A. & Leitherer, C. 2005, *ApJ*, 621, 695
- Yan, L. et al. 2004, *ApJS*, 154, 60

Table 1. Galaxy Sample and Infrared Photometry Apertures

Galaxy	m_B (mag)	cz (km s ⁻¹)	D (Mpc)	T	$E(B-V)$ (mag)	α_0 & δ_0 (J2000)	$2a$ ($''$)	$2b$ ($''$)	PA ($^\circ$)
WLM	11.03	-116	0.92	10	0.04	000158.9–152655	672	340	0
NGC0024	12.19	554	8.13	5	0.02	000955.9–245755	301	216	225
NGC0045	11.32	471	7.07	8	0.02	001404.6–231101	577	456	336
NGC0055	8.42	129	2.17	9	0.01	001508.2–391256	2251	714	106
NGC0059	13.12	382	5.30	-3	0.02	001525.8–212646	256	180	302
ESO410-G005	14.95	...	1.90	-1	0.01	001531.0–321048	193	144	308
Sculptor-dE1	17.78	...	4.20	10	0.02	002351.6–244204	160	103	0
ESO294-G010	15.52	117	1.90	-3	0.01	002633.7–415120	165	102	0
IC1574	14.50	361	4.92	10	0.02	004303.9–221444	202	123	0
NGC0247	9.67	160	3.65	7	0.02	004708.9–204456	1476	581	352
NGC0253	8.04	241	3.94	5	0.02	004733.2–251734	2050	808	50
ESO540-G030	16.46	...	3.40	-1	0.02	004920.8–180406	168	148	0
UGCA015	15.38	301	3.34	10	0.02	004949.1–210049	150	78	28
ESO540-G032	16.55	...	3.40	-3	0.02	005024.6–195427	100	91	0
UGC00521	15.31	659	11.32	10	0.07	005112.2+120129	107	107	90
SMC ^a	2.70	158	0.06	9	0.42
NGC0300	8.72	144	2.00	7	0.01	005458.1–374054	1507	1128	114
UGC00668	9.88	-234	0.65	10	0.02	010450.5+020720	682	547	60
UGC00685	14.20	157	4.70	9	0.06	010723.2+164101	179	147	122
UGC00695	15.28	664	10.20	6	0.03	010746.5+010347	129	109	0
NGC404	11.51	-48	3.10	-1	0.06	010927.7+354307	234	229	0
UGC00891	14.72	643	10.84	9	0.03	012118.9+122438	194	118	42
UGC01056	14.87	595	10.32	10	0.07	012847.6+164117	125	117	0
UGC01104	14.41	686	7.50	9	0.06	013242.5+181906	166	103	0
NGC0598	6.27	-179	0.84	6	0.04	013350.8+303920	4453	2762	12
NGC0625	11.71	405	4.07	9	0.02	013504.4–412624	499	256	90
NGC0628	9.95	657	7.30	5	0.07	013641.8+154717	721	717	338
UGC01176	14.40	633	9.00	10	0.06	014010.0+155426	202	168	25
ESO245-G005	12.70	395	4.43	10	0.02	014503.6–433528	358	253	318
UGC01249	12.07	338	7.20	9	0.08	014729.0+271960	524	290	331
NGC0672	11.47	421	7.20	6	0.08	014752.7+272550	556	361	67
ESO245-G007	13.33	56	0.44	10	0.02	015106.1–442647	288	240	0
NGC0784	12.23	198	5.19	8	0.06	020116.7+285005	480	191	3
NGC855	13.30	595	9.73	-5	0.07	021403.9+275239	190	171	68
ESO115-G021	13.34	513	4.99	8	0.03	023746.8–612018	332	147	221
ESO154-G023	12.69	578	5.76	8	0.02	025652.4–543359	486	248	39
NGC1291	9.39	839	9.37	0	0.01	031719.1–410632	840	804	0
NGC1313	9.20	475	4.15	7	0.11	031810.0–662908	896	694	338
NGC1311	13.18	571	5.45	9	0.02	032006.9–521114	300	141	36
UGC02716	14.64	379	6.23	8	0.14	032407.9+174512	174	123	90
IC1959	13.26	640	6.06	9	0.01	033312.4–502445	253	114	330
NGC1487	12.34	848	9.08	7	0.01	035545.5–422200	391	260	63
NGC1510	13.47	913	9.84	-2	0.01	040332.7–432359	126	122	0
NGC1512	11.13	896	9.64	1	0.01	040355.0–432044	491	288	55
NGC1522	13.93	905	9.32	11	0.01	040607.6–524011	151	99	37

Table 1—Continued

Galaxy	m_B (mag)	cz (km s ⁻¹)	D (Mpc)	T	$E(B-V)$ (mag)	α_0 & δ_0 (J2000)	$2a$ ($''$)	$2b$ ($''$)	PA ($^\circ$)
IC2049	15.19	869	16.73	7	0.02	041204.2–583327	119	106	0
ESO483-G013	14.18	823	10.43	–3	0.05	041240.9–230928	205	147	322
ESO158-G003	14.01	975	9.96	9	0.01	044615.6–572044	199	172	0
ESO119-G016	14.79	969	9.84	10	0.02	045128.6–613905	221	116	26
NGC1705	12.77	628	5.10	11	0.01	045413.5–532137	167	120	220
NGC1744	11.60	748	7.65	7	0.04	045957.8–260116	410	225	349
NGC1796	12.86	987	10.32	5	0.02	050242.8–610822	256	205	99
ESO486-G021	14.47	865	8.89	2	0.03	050319.9–252524	115	99	90
MCG-05-13-004 ^b	13.22	686	6.63	9	0.01
NGC1800	13.07	803	8.24	9	0.01	050625.7–315715	229	163	107
UGCA106	13.05	933	9.77	9	0.02	051159.2–325817	323	245	14
LMC ^a	0.91	278	0.05	9	0.92
KKH037	16.40	–148	3.39	10	0.07	064744.2+800723	105	81	90
NGC2366	11.43	100	3.19	10	0.04	072850.9+691248	501	298	31
UGCA133	15.80	...	3.20	–3	0.04	073412.2+665313	215	153	0
NGC2403	8.93	131	3.22	6	0.04	073655.0+653554	1164	848	130
NGC2500	12.20	514	7.63	7	0.04	080152.4+504405	274	234	75
NGC2537	12.82	447	6.90	9	0.05	081314.7+455936	211	199	0
UGC04278	13.07	565	7.59	7	0.05	081358.7+454445	319	79	351
UGC04305	11.10	157	3.39	10	0.03	081906.8+704309	442	430	90
NGC2552	12.56	524	7.65	9	0.05	081920.0+500038	312	205	54
M81dwA	18.69	113	3.55	10	0.02	082356.0+710145	78	78	90
UGC04426	15.00	397	10.28	10	0.04	082828.4+415124	206	145	10
UGC04459	14.78	19	3.56	10	0.04	083406.8+661036	134	111	120
UGC04483	15.27	178	3.21	10	0.03	083703.5+694632	94	58	0
NGC2683	10.64	411	7.70	3	0.03	085241.0+332516	822	420	41
UGC04704	15.33	596	7.75	8	0.03	085902.5+391223	303	108	296
UGC04787	15.41	552	6.53	8	0.02	090735.1+331638	211	107	5
UGC04998	14.72	623	10.50	10	0.06	092512.9+682258	187	162	71
NGC2903	9.68	556	8.90	4	0.03	093210.9+213005	824	461	17
UGC05076	15.21	571	8.31	10	0.02	093236.5+515216	165	139	90
CGCG035-007	15.46	574	5.17	5	0.04	093444.9+062532	126	96	63
UGC05139	14.17	143	3.84	10	0.05	094030.5+711033	265	228	210
IC0559	14.82	513	4.93	5	0.03	094443.9+093655	135	124	63
F8D1	16.14	...	3.80	–3	0.11	094447.1+672619	254	254	90
[FM2000]1	17.80	...	3.40	–3	0.08	094510.0+684547	89	89	90
NGC2976	11.24	3	3.56	5	0.07	094715.9+675507	457	312	322
LEDA166101	16.94	...	3.50	–3	0.14	095013.0+673037	219	152	33
UGC05272	15.41	520	7.10	10	0.02	095023.1+312917	196	96	112
UGC05288	14.32	557	6.80	8	0.03	095116.9+074939	164	141	331
BK03N	18.78	–40	4.02	10	0.08	095348.5+685808	41	41	90
NGC3031	7.89	–34	3.63	2	0.08	095531.8+690403	1629	1123	154
NGC3034	9.30	203	3.53	7	0.16	095552.1+694057	698	581	65
UGC05340	14.76	503	5.90	10	0.02	095645.8+284932	115	81	0
KDG061	15.17	–135	3.60	8	0.07	095704.5+683536	214	119	49

Table 1—Continued

Galaxy	m_B (mag)	cz (km s ⁻¹)	D (Mpc)	T	$E(B-V)$ (mag)	α_0 & δ_0 (J2000)	$2a$ ($''$)	$2b$ ($''$)	PA ($^\circ$)
UGC05336	14.30	46	3.70	10	0.08	095729.2+690250	248	181	220
Arp'sLoop	16.76	99	3.90	10	0.08	095732.7+691700	137	137	90
UGC05364	12.92	20	0.69	10	0.02	095926.5+304458	311	192	67
UGC05373	11.85	301	1.44	10	0.03	095959.5+051957	333	268	90
KKH057	17.95	...	3.90	-3	0.02	100014.6+631058	73	53	45
UGCA193	14.84	662	9.70	7	0.04	100236.4-060031	284	69	14
NGC3109	10.39	403	1.34	9	0.07	100307.6-260948	900	334	90
NGC3077	10.61	14	3.82	6	0.07	100319.2+684401	576	483	64
AM1001-270	16.51	362	1.30	10	0.08	100403.0-271948	169	96	319
BK05N	17.77	...	3.80	-3	0.06	100441.6+681526	207	102	330
UGC5428	15.95	-129	3.50	10	0.10	100507.5+663339	196	168	90
UGC05423	15.20	350	5.30	10	0.08	100531.3+702152	107	70	140
UGC5442	15.78	-18	3.70	-3	0.05	100701.2+674938	197	124	34
UGC05456	13.72	544	3.80	5	0.04	100719.4+102151	161	121	322
IKN	17.31	...	3.70	-3	0.06	100805.9+682357	180	156	180
SextansA	11.86	324	1.32	10	0.04	101100.8-044134	285	258	0
[HS98]117	17.01	-37	4.00	10	0.12	102125.5+710652	213	129	0
NGC3239	11.73	753	8.29	9	0.03	102504.7+170856	315	272	63
DDO078	15.84	55	3.70	-3	0.02	102627.4+673916	141	141	90
UGC05672	15.14	531	6.30	5	0.02	102820.9+223409	289	104	340
UGC05666	10.80	57	4.02	9	0.04	102822.7+682448	827	377	230
UGC05692	13.71	180	4.00	9	0.04	103036.4+703713	306	211	0
NGC3274	13.21	537	6.50	7	0.02	103216.6+274007	186	135	90
BK06N	16.85	...	3.80	-3	0.01	103432.4+660036	231	108	304
NGC3299	14.11	641	10.40	8	0.02	103623.8+124231	264	207	0
UGC05764	15.21	586	7.08	10	0.02	103643.1+313245	150	85	44
UGC05797	15.00	713	6.84	10	0.03	103925.4+014302	141	138	0
UGC05829	13.73	629	7.88	10	0.02	104241.6+342657	270	204	57
NGC3344	10.45	586	6.64	4	0.03	104332.3+245524	396	394	0
NGC3351	10.53	778	10.00	3	0.03	104357.5+114219	586	457	10
NGC3368	10.11	897	10.52	2	0.03	104645.5+114905	511	349	346
UGC05889	14.22	572	9.30	9	0.03	104722.2+140416	202	190	0
UGC05923	14.03	712	7.16	0	0.03	104907.5+065504	113	70	353
UGC05918	15.22	340	7.40	10	0.01	104936.5+653149	140	113	65
NGC3432	11.67	616	7.89	9	0.01	105232.7+363747	476	187	38
KDG73	17.28	-132	3.70	10	0.02	105256.5+693317	126	100	345
NGC3486	11.05	681	8.24	5	0.02	110023.2+285834	495	389	83
NGC3510	14.30	705	8.57	8	0.03	110343.6+285301	310	136	345
NGC3521	9.83	805	8.03	4	0.06	110548.7-000222	767	494	343
NGC3593	11.86	628	6.52	0	0.02	111436.7+124903	373	211	86
NGC3623	10.25	807	8.95	1	0.02	111856.0+130525	663	331	352
NGC3627	9.65	727	10.05	3	0.03	112013.4+125927	746	487	347
NGC3628	10.28	843	9.45	3	0.03	112014.8+133518	1039	619	102
UGC06457	15.00	963	10.24	10	0.03	112712.4-005944	150	111	19
UGC06541	14.40	249	3.89	11	0.02	113328.1+491428	124	87	316

Table 1—Continued

Galaxy	m_B (mag)	cz (km s ⁻¹)	D (Mpc)	T	$E(B-V)$ (mag)	α_0 & δ_0 (J2000)	$2a$ ($''$)	$2b$ ($''$)	PA ($^\circ$)
NGC3738	11.97	229	4.90	10	0.01	113548.6+543129	220	175	343
NGC3741	14.49	229	3.19	10	0.02	113606.0+451709	137	108	7
UGC06782	15.07	525	14.00	9	0.03	114857.2+235016	120	120	90
UGC06817	13.56	242	2.64	10	0.03	115054.1+385259	233	174	39
UGC06900	14.80	590	7.47	10	0.02	115539.9+313106	204	145	107
NGC4020	13.82	760	9.68	7	0.02	115856.5+302442	222	136	18
NGC4068	13.02	210	4.31	10	0.02	120402.8+523523	255	178	22
NGC4080	14.28	567	6.92	10	0.03	120451.8+265932	153	131	312
NGC4096	11.48	566	8.28	5	0.02	120600.3+472847	556	243	18
NGC4144	12.05	265	9.80	6	0.01	120958.9+462730	437	189	103
NGC4163	13.75	165	2.96	10	0.02	121208.9+361008	213	164	4
NGC4190	13.90	228	3.50	10	0.03	121344.6+363808	210	164	45
ESO321-G014	15.63	610	3.20	10	0.09	121349.3–381347	171	105	22
UGC07242	14.65	68	5.42	6	0.02	121408.4+660541	157	85	0
UGCA276	15.70	284	3.18	10	0.02	121459.9+361301	161	143	301
UGC07267	15.29	472	7.33	8	0.02	121523.9+512104	189	98	45
NGC4214	10.24	291	2.92	10	0.02	121538.4+361943	476	452	0
CGCG269-049	15.30	159	3.23	10	0.02	121547.3+522315	94	67	319
NGC4236	10.05	0	4.45	8	0.01	121635.9+692808	1129	420	155
NGC4244	10.88	244	4.49	6	0.02	121729.8+374825	1182	242	47
NGC4242	11.37	517	7.43	8	0.01	121730.4+453710	410	312	28
UGC07321	14.15	408	20.00	7	0.03	121734.3+223225	370	78	81
NGC4248	13.21	484	7.24	3	0.02	121750.7+472432	251	170	107
NGC4258	9.10	448	7.98	4	0.02	121854.9+471824	1160	529	333
ISZ399	14.72	900	8.97	11	0.06	121959.5–172331	132	102	314
NGC4288	13.26	535	7.67	7	0.01	122038.3+461737	190	163	139
UGC07408	13.35	462	6.87	9	0.01	122115.5+454900	220	192	90
UGC07490	13.05	465	8.40	9	0.02	122424.6+701958	226	220	0
NGC4395	10.64	319	4.61	9	0.02	122552.2+333315	1008	790	328
UGCA281	15.36	281	5.70	11	0.01	122616.7+482939	87	73	81
UGC07559	14.20	218	4.87	10	0.01	122706.1+370830	154	108	336
UGC07577	12.84	196	2.74	10	0.02	122743.4+432926	312	218	301
NGC4449	9.99	207	4.21	10	0.02	122810.4+440525	473	354	57
UGC07599	14.88	278	6.90	8	0.02	122828.2+371401	92	70	312
UGC07605	14.79	309	4.43	10	0.01	122838.4+354301	141	86	17
NGC4455	13.80	637	7.75	7	0.02	122844.0+224918	200	90	198
UGC07608	13.67	538	7.76	10	0.02	122845.2+431332	156	138	0
NGC4460	12.78	490	9.59	–1	0.02	122845.9+445157	338	147	37
UGC07639	13.99	382	8.00	10	0.01	122953.3+473154	231	140	334
NGC4485	12.32	493	7.07	10	0.02	123031.8+414202	180	134	343
NGC4490	10.22	565	8.03	7	0.02	123034.4+413841	418	232	121
UGC07690	13.10	537	7.73	10	0.03	123226.8+424225	195	151	36
UGC07699	13.60	496	6.85	6	0.01	123248.0+373718	270	105	32
UGC07698	13.00	331	6.10	10	0.02	123254.0+313218	217	127	342
UGC07719	15.33	678	9.39	8	0.02	123400.6+390116	158	86	347

Table 1—Continued

Galaxy	m_B (mag)	cz (km s ⁻¹)	D (Mpc)	T	$E(B-V)$ (mag)	α_0 & δ_0 (J2000)	$2a$ ($''$)	$2b$ ($''$)	PA ($^\circ$)
UGC07774	15.02	526	7.44	7	0.02	123622.8+400019	201	57	100
UGCA292	16.10	307	3.10	10	0.02	123840.1+324601	60	42	325
NGC4594	8.98	1024	9.33	1	0.05	123959.4–113714	555	233	90
NGC4605	10.89	143	5.47	5	0.01	123958.9+613628	498	330	303
NGC4618	11.22	544	7.79	8	0.02	124133.3+410841	335	267	22
NGC4625	12.92	609	8.65	9	0.02	124152.3+411618	198	191	140
NGC4631	9.75	606	8.05	7	0.02	124203.7+323205	953	540	80
UGC07866	13.71	354	4.57	10	0.02	124215.0+383020	162	125	357
NGC4656	10.96	646	8.59	9	0.01	124356.2+320930	719	255	220
UGC07916	15.00	607	8.21	10	0.02	124425.1+342312	150	102	90
UGC07950	15.10	502	7.91	10	0.02	124656.2+513649	144	124	0
UGC07949	15.12	333	9.90	10	0.02	124700.7+362850	124	85	90
NGC4707	13.40	468	7.44	9	0.01	124823.3+510952	207	177	20
NGC4736	8.99	308	4.66	2	0.02	125056.7+410706	1033	825	100
UGC08024	13.94	374	4.30	10	0.01	125405.2+270854	199	126	213
NGC4826	9.36	408	7.50	2	0.04	125642.8+214050	723	449	113
UGC08091	14.68	214	2.13	10	0.03	125839.7+141306	125	92	32
UGCA319	14.96	747	7.40	9	0.08	130214.4–171417	130	90	24
UGCA320	13.52	744	7.24	9	0.08	130317.0–172529	491	163	114
UGC08188	12.40	321	4.49	9	0.01	130550.8+373615	379	326	90
UGC08201	12.80	37	4.57	10	0.02	130625.0+674226	268	150	90
MCG-03-34-002	14.79	922	10.16	4	0.08	130756.6–164120	130	80	320
UGC08245	15.22	70	3.64	10	0.03	130835.3+785612	201	105	70
NGC5023	12.85	407	5.40	6	0.02	131211.7+440221	410	127	26
CGCG217-018	15.10	570	8.21	10	0.01	131251.6+403232	114	87	35
UGC08313	14.78	625	8.72	5	0.01	131354.3+421231	191	114	30
UGC08320	13.11	192	4.33	10	0.02	131426.5+455527	292	198	341
UGC08331	14.31	260	8.20	10	0.01	131529.6+473004	236	115	323
NGC5055	9.31	504	7.55	4	0.02	131548.3+420142	893	683	101
NGC5068	10.70	673	6.24	6	0.10	131855.4–210212	613	593	90
IC4247	14.57	274	4.97	2	0.06	132644.2–302143	129	78	333
NGC5204	11.73	201	4.65	9	0.01	132936.0+582510	338	211	351
NGC5194	8.96	463	8.00	4	0.04	132950.6+471307	1699	1130	15
NGC5195	10.45	465	8.00	2	0.04	132959.4+471556	203	192	0
UGC08508	13.94	62	2.69	10	0.02	133043.1+545436	160	120	305
NGC5229	14.18	364	5.10	7	0.02	133402.9+475452	279	102	347
NGC5238	13.60	235	5.20	8	0.01	133442.8+513650	216	166	0
[KK98]208	14.30	381	4.68	10	0.04	133635.5–293417	360	150	57
NGC5236	8.20	516	4.47	5	0.07	133700.8–295224	1100	1055	0
ESO444-G084	15.48	587	4.61	10	0.07	133720.2–280244	84	78	0
UGC08638	15.10	274	4.27	10	0.01	133919.4+244634	179	132	73
UGC08651	14.45	201	3.02	10	0.01	133953.5+404423	194	140	59
NGC5253	10.87	404	3.15	11	0.06	133956.1–313832	351	193	44
NGC5264	12.60	478	4.53	9	0.05	134136.0–295448	268	226	66
UGC08760	14.45	193	3.24	10	0.02	135051.3+380113	216	113	29

Table 1—Continued

Galaxy	m_B (mag)	cz (km s ⁻¹)	D (Mpc)	T	$E(B-V)$ (mag)	α_0 & δ_0 (J2000)	$2a$ ($''$)	$2b$ ($''$)	PA ($^\circ$)
KKH086	16.99	287	2.60	10	0.03	135433.8+041443	131	83	0
UGC08837	13.71	144	8.30	10	0.01	135444.0+535347	364	148	17
UGC08833	15.15	228	3.20	10	0.01	135448.4+355018	121	115	0
NGC5457	8.31	241	6.70	6	0.01	140312.2+542307	1450	1039	37
NGC5474	11.82	273	7.20	6	0.01	140459.9+533913	386	335	210
NGC5477	14.24	304	7.70	9	0.01	140533.0+542732	169	124	64
[KK98]230	17.84	62	2.14	10	0.01	140710.4+350335	67	49	0
UGC09128	14.46	154	2.24	10	0.02	141556.8+230321	127	88	36
NGC5585	11.20	305	5.70	7	0.02	141948.4+564349	392	266	38
UGC09240	13.31	150	2.80	10	0.01	142443.4+443134	222	182	90
UGC09405	14.57	222	8.00	10	0.01	143524.0+571516	199	136	333
MRK475	15.46	583	9.02	11	0.01	143905.5+364819	72	71	196
NGC5832	14.09	447	8.74	3	0.03	145747.6+714056	293	180	49
NGC5949	13.37	435	8.53	4	0.02	152800.3+644548	219	135	324
UGC09992	14.86	427	8.56	10	0.04	154147.9+671515	156	109	340
KKR25	16.53	-139	1.90	10	0.01	161347.6+542216	94	87	0
NGC6503	10.91	60	5.27	6	0.03	174927.5+700838	394	217	120
IC4951	13.91	794	9.34	8	0.04	200931.8-615104	225	92	355
DDO210	14.14	-137	0.94	10	0.05	204651.6-125044	155	72	103
IC5052	11.79	598	5.86	7	0.05	205206.0-691201	450	168	323
NGC7064	13.10	797	9.86	5	0.01	212903.4-524605	250	81	90
NGC7090	11.33	857	10.41	5	0.02	213628.8-543320	539	161	308
IC5152	10.68	124	1.97	10	0.03	220242.0-511741	312	274	90
IC5256	14.58	950	10.76	8	0.03	224945.4-684127	124	76	22
UGCA438	14.67	62	2.22	10	0.01	232627.4-322317	189	163	0
ESO347-G017	14.41	690	9.37	9	0.02	232655.9-372050	212	129	90
UGC12613	12.50	-183	0.76	10	0.07	232833.7+144437	461	269	113
IC5332	11.21	706	9.53	7	0.02	233427.6-360601	645	573	0
NGC7713	11.51	689	9.28	7	0.02	233615.4-375616	370	227	345
UGCA442	13.60	267	4.27	9	0.02	234346.7-315724	245	117	43
KKH098	17.22	-137	2.50	10	0.12	234534.1+384301	126	79	5
ESO149-G003	15.04	594	6.40	10	0.01	235202.4-523428	249	100	332
NGC7793	9.63	230	3.91	7	0.02	235750.4-323530	755	499	90

Note. — Magnitudes, redshifts, distances, and optical morphologies are from Kennicutt et al. (2008), and the Milky Way foreground extinctions are from Schlegel, Finkbeiner, & Davis(1998). The position angles in the above ellipse parameters are measured east of north.

^aInfrared photometry for the Large and Small Magellanic Clouds are from Bernard et al. (2008) and Leroy et al. (2007), respectively.

^bNGC 1800 and MCG-05-13-004 spatially overlap so separate photometry for MCG-05-13-004 is not provided.

Table 2. Infrared Flux Densities

Galaxy	2MASS J 1.25 μm (Jy)	2MASS H 1.65 μm (Jy)	2MASS K _s 2.17 μm (Jy)	IRAC 3.6 μm (Jy)	IRAC 4.5 μm (Jy)	IRAC 5.8 μm (Jy)	IRAC 8.0 μm (Jy)	MIPS 24 μm (Jy)	MIPS 70 μm (Jy)	MIPS 160 μm (Jy)
WLM ^{e f}	2.45±0.24E-1	3.13±0.31E-1	1.17±0.12E-1	9.09±1.23E-2	6.28±0.86E-2	4.87±0.62E-2	5.07±0.63E-2	7.58±0.82E-2	2.00±0.25E 0	3.88±0.61E-1
NGC0024 ^{e f}	2.32±0.23E-1	2.49±0.25E-1	1.90±0.19E-1	1.04±0.14E-1	7.06±1.01E-2	8.81±1.16E-2	1.28±0.16E-1	1.30±0.07E-1	2.23±0.19E 0	7.00±1.05E-1
NGC0045	2.08±0.21E-1	2.29±0.23E-1	1.67±0.17E-1	2.00±0.27E-1	1.27±0.17E-1	6.56±0.83E-2	1.69±0.21E-1	1.87±0.20E-1	3.87±0.47E 0	1.23±0.19E-1
NGC0055 ^{e f}	3.31±0.33E 0	3.08±0.31E 0	2.63±0.26E 0	2.03±0.27E 0	1.40±0.19E 0	1.50±0.19E 0	2.28±0.28E 0	6.29±0.68E 0	1.20±0.15E 2	2.53±0.40E-1
NGC0059	8.48±0.85E-2	1.13±0.11E-1	6.36±0.64E-2	3.29±0.45E-2	2.23±0.31E-2	1.56±0.20E-2	1.18±0.15E-2	4.40±0.47E-2	5.15±0.63E-1	4.07±0.66E-1
ESO410-G005	<6.18E-2	<9.05E-2	<1.11E-1	1.58±0.21E-2	6.46±0.89E-3	1.12±0.15E-2	6.40±0.81E-3	4.43±0.46E-3	5.98±0.81E-2	2.26±0.31E-1
Sculptor-dE1	<3.66E-2	<5.35E-2	<6.59E-2	<3.40E-4	<5.10E-4	<1.88E-3	<2.06E-3	<3.42E-3	<4.63E-2	<1.75E-1
ESO294-G010	1.73±0.17E-2	2.12±0.21E-2	1.35±0.14E-2	4.79±0.65E-3	3.12±0.43E-3	<1.89E-3	<2.06E-3	<3.44E-3	<4.64E-2	<1.75E-1
IC1574	1.96±0.20E-2	2.18±0.22E-2	1.55±0.16E-2	5.93±0.80E-3	3.94±0.54E-3	2.62±0.36E-3	1.73±0.24E-3	<1.22E-3	<5.65E-2	<2.13E-1
NGC0247	1.47±0.15E 0	1.30±0.13E 0	1.02±0.10E 0	8.54±1.15E-1	5.89±0.81E-1	6.12±0.77E-1	8.48±1.06E-1	9.89±1.06E-1	1.57±0.19E 1	6.88±1.07E-1
NGC0253 ^e	2.11±0.21E 1	2.53±0.25E 1	2.23±0.22E 1	1.23±0.17E 1	8.25±1.13E 0	1.94±0.24E 1	3.86±0.48E 1	8.00±0.86E 1	1.18±0.14E 3	1.87±0.29E-1
ESO540-G030	<5.54E-2	<8.08E-2	<9.94E-2	2.17±0.29E-3	1.58±0.22E-3	<1.66E-3	<1.81E-3	<3.42E-3	<4.07E-2	<1.53E-1
UGCA015	6.42±0.64E-3	9.01±0.90E-3	4.27±0.43E-3	2.11±0.29E-3	1.67±0.23E-3	1.58±0.18E-3	1.73±0.19E-3	<2.87E-3	<3.86E-2	<1.47E-1
ESO540-G032	4.75±0.48E-3	1.15±0.12E-2	<3.64E-2	1.46±0.20E-3	7.60±1.10E-4	<7.00E-4	<7.60E-4	<2.54E-3	<3.43E-2	<1.30E-1
UGC00521	8.60±0.86E-3	9.60±0.96E-3	5.42±0.54E-3	3.01±0.41E-3	2.24±0.31E-3	1.04±0.14E-3	1.16±0.15E-3
SMC ^{a e f}	3.51±0.52E 2	1.25±0.26E 4	1.90±0.49E-1
NGC0300	3.26±0.33E 0	3.27±0.33E 0	2.52±0.25E 0	1.63±0.22E 0	1.20±0.16E 0	1.25±0.16E 0	2.02±0.25E 0	2.50±0.27E 0	4.61±0.56E 1	1.62±0.25E-1
UGC00668 ^{e f}	3.05±0.30E-1	4.74±0.47E-1	2.32±0.23E-1	1.24±0.17E-1	9.09±1.25E-2	3.34±0.42E-2	7.13±0.89E-2	8.63±0.93E-2	2.46±0.30E 0	5.99±0.94E-1
UGC00685	4.20±0.42E-2	2.28±0.23E-2	<1.04E-1	1.14±0.16E-2	7.47±1.03E-3	4.27±0.57E-3	5.28±0.67E-3
UGC00695	9.45±0.95E-3	9.99±1.00E-3	<5.51E-2	4.46±0.61E-3	3.01±0.41E-3	1.84±0.25E-3	1.47±0.20E-3
NGC0404 ^e	8.10±0.81E-1	8.41±0.84E-1	6.76±0.68E-1	4.72±0.64E-1	2.53±0.35E-1	2.29±0.30E-1	1.57±0.20E-1	1.46±0.16E-1	2.84±0.35E 0	3.52±0.55E-1
UGC00891	2.43±0.24E-2	1.34±0.13E-2	1.55±0.16E-2	6.11±0.83E-3	4.19±0.58E-3	1.83±0.26E-3	3.69±0.47E-3
UGC01056	1.77±0.18E-2	2.60±0.26E-2	2.91±0.29E-2	5.59±0.76E-3	4.14±0.57E-3	2.60±0.35E-3	4.22±0.54E-3
UGC01104	2.02±0.20E-2	2.11±0.21E-2	1.58±0.16E-2	8.45±1.15E-3	5.70±0.78E-3	3.44±0.46E-3	5.01±0.64E-3
NGC0598 ^{e f}	2.12±0.21E 1	2.12±0.21E 1	1.67±0.17E 1	1.97±0.27E 1	1.39±0.19E 1	1.29±0.16E 1	2.78±0.35E 1	4.81±0.52E 1	7.81±0.95E 2	2.32±0.36E-1
NGC0625	2.83±0.28E-1	2.97±0.30E-1	2.42±0.24E-1	1.23±0.17E-1	8.83±1.21E-2	9.22±1.17E-2	1.37±0.17E-1	8.79±0.95E-1	6.49±0.79E 0	8.52±1.33E-1
NGC0628 ^{e f}	1.66±0.17E 0	1.67±0.17E 0	1.32±0.13E 0	8.72±1.18E-1	5.45±0.75E-1	1.15±0.15E 0	2.70±0.34E 0	3.13±0.13E 0	3.38±0.25E 1	1.19±0.15E-1
UGC01176	<7.90E-2	<1.10E-1	<1.35E-1	8.28±1.12E-3	6.22±0.85E-3	4.43±0.59E-3	4.37±0.56E-3
ESO245-G005	5.02±0.50E-2	5.90±0.59E-2	4.14±0.41E-2	2.18±0.30E-2	1.53±0.21E-2	1.81±0.23E-2	7.77±0.98E-3	2.47±0.27E-2	5.95±0.74E-1	1.08±0.17E-1
UGC01249	1.05±0.11E-1	1.73±0.17E-1	8.91±0.89E-2	6.19±0.84E-2	3.86±0.53E-2	3.79±0.48E-2	1.94±0.24E-2	9.50±1.03E-2	1.87±0.23E 0	4.25±0.66E-1
NGC0672	3.59±0.36E-1	3.66±0.37E-1	2.96±0.30E-1	1.52±0.21E-1	1.18±0.16E-1	1.16±0.15E-1	1.16±0.14E-1	3.38±0.36E-1	5.90±0.72E 0	1.50±0.23E-1
ESO245-G007 ^f	4.34±0.43E-2	3.61±0.36E-2	<5.00E-2	1.72±0.23E-2	1.25±0.17E-2	<4.32E-3	<5.45E-3	<6.98E-3	<9.41E-2	<3.55E-1
NGC0784	1.03±0.10E-1	1.02±0.10E-1	7.22±0.72E-2	4.98±0.67E-2	3.50±0.48E-2	2.69±0.34E-2	1.52±0.19E-2	4.94±0.53E-2	1.15±0.14E 0	1.92±0.30E-1

Table 2—Continued

Galaxy	2MASS J 1.25 μm (Jy)	2MASS H 1.65 μm (Jy)	2MASS K _s 2.17 μm (Jy)	IRAC 3.6 μm (Jy)	IRAC 4.5 μm (Jy)	IRAC 5.8 μm (Jy)	IRAC 8.0 μm (Jy)	MIPS 24 μm (Jy)	MIPS 70 μm (Jy)	MIPS 160 μm (Jy)
NGC0855 ^{e f}	9.07±0.91E-2	9.78±0.98E-2	7.97±0.80E-2	4.24±0.60E-2	2.75±0.39E-2	1.83±0.30E-2	4.57±0.57E-2	8.65±0.42E-2	1.64±0.14E 0	2.29±0.30E-1
ESO115-G021	5.85±0.58E-2	6.67±0.67E-2	4.17±0.42E-2	1.87±0.25E-2	1.24±0.17E-2	8.90±1.16E-3	7.73±0.97E-3	1.71±0.19E-2	3.85±0.48E-1	7.04±1.15E-1
ESO154-G023	1.32±0.13E-1	1.41±0.14E-1	1.05±0.10E-1	3.76±0.51E-2	3.08±0.42E-2	1.59±0.20E-2	1.86±0.23E-2	4.99±0.54E-2	1.03±0.13E 0	1.84±0.25E-1
NGC1291 ^{e f}	4.37±0.44E 0	4.56±0.46E 0	3.98±0.40E 0	2.11±0.28E 0	1.27±0.18E 0	9.47±1.22E-1	6.35±0.80E-1	5.60±0.24E-1	6.17±0.46E 0	2.76±0.30E-1
NGC1313	9.81±0.98E-1	1.04±0.10E 0	7.41±0.74E-1	6.43±0.87E-1	4.87±0.67E-1	6.18±0.77E-1	1.22±0.15E 0	2.85±0.31E 0	5.15±0.63E 1	9.62±1.50E-1
NGC1311	5.13±0.51E-2	5.25±0.52E-2	4.08±0.41E-2	2.37±0.32E-2	1.68±0.23E-2	1.27±0.16E-2	1.23±0.16E-2	2.90±0.31E-2	7.20±0.88E-1	1.16±0.18E-1
UGC02716	2.53±0.25E-2	2.56±0.26E-2	2.22±0.22E-2	1.20±0.16E-2	7.58±1.04E-3	7.23±0.95E-3	8.67±1.09E-3	8.68±0.96E-3	1.56±0.20E-1	1.48±0.20E-1
IC1959	3.45±0.34E-2	3.54±0.35E-2	2.77±0.28E-2	1.91±0.26E-2	1.31±0.18E-2	9.81±1.28E-3	1.00±0.13E-2	3.24±0.35E-2	8.99±1.10E-1	1.08±0.17E-1
NGC1487	1.32±0.13E-1	1.78±0.18E-1	1.20±0.12E-1	7.10±0.96E-2	4.61±0.63E-2	7.63±0.98E-2	1.37±0.17E-1	2.94±0.32E-1	4.68±0.57E 0	7.60±1.15E-1
NGC1510	3.77±0.38E-2	3.71±0.37E-2	3.09±0.31E-2	1.71±0.23E-2	1.19±0.16E-2	1.41±0.19E-2	2.20±0.28E-2	1.35±0.15E-1	9.19±1.12E-1	6.08±0.90E-1
NGC1512 ^{e f}	8.12±0.81E-1	8.57±0.86E-1	7.30±0.73E-1	3.88±0.53E-1	2.43±0.34E-1	2.64±0.34E-1	4.37±0.55E-1	4.38±0.21E-1	6.34±0.48E 0	2.24±0.25E-1
NGC1522	2.61±0.26E-2	2.28±0.23E-2	1.99±0.20E-2	1.10±0.15E-2	7.87±1.08E-3	9.83±1.29E-3	1.51±0.19E-2	9.66±1.04E-2	9.41±1.15E-1	8.03±1.20E-1
IC2049	1.08±0.11E-2	1.26±0.13E-2	8.79±0.88E-3	4.39±0.60E-3	2.83±0.39E-3	1.10±0.16E-3	3.04±0.39E-3	4.70±0.53E-3	6.16±0.88E-2	1.25±0.25E-2
ESO483-G013	3.93±0.39E-2	3.85±0.39E-2	3.37±0.34E-2	1.68±0.23E-2	1.14±0.16E-2	1.22±0.16E-2	1.12±0.14E-2	3.46±0.37E-2	5.40±0.66E-1	4.77±0.70E-1
ESO158-G003	3.84±0.38E-2	3.54±0.35E-2	2.74±0.27E-2	1.64±0.22E-2	1.14±0.16E-2	1.11±0.14E-2	2.04±0.26E-2	2.91±0.31E-2	5.37±0.66E-1	1.02±0.10E-1
ESO119-G016	1.89±0.19E-2	2.21±0.22E-2	1.51±0.15E-2	7.40±1.00E-3	5.37±0.74E-3	2.81±0.38E-3	2.91±0.38E-3	6.11±0.70E-3	7.33±1.11E-2	1.63±0.25E-2
NGC1705 ^{e f}	5.75±0.57E-2	5.40±0.54E-2	4.44±0.44E-2	2.57±0.36E-2	1.79±0.25E-2	1.01±0.19E-2	1.68±0.20E-2	5.45±0.22E-2	1.26±0.10E 0	1.44±0.25E-1
NGC1744	1.12±0.11E-1	1.13±0.11E-1	8.94±0.89E-2	8.32±1.13E-2	6.44±0.88E-2	4.96±0.63E-2	9.56±1.19E-2	1.10±0.12E-1	1.98±0.24E 0	6.27±0.90E-1
NGC1796	1.02±0.10E-1	1.12±0.11E-1	9.55±0.95E-2	5.51±0.75E-2	3.76±0.52E-2	8.48±1.09E-2	1.91±0.24E-1	2.22±0.24E-1	3.38±0.41E 0	6.86±1.07E-1
ESO486-G021	1.87±0.19E-2	2.07±0.21E-2	1.32±0.13E-2	6.57±0.89E-3	4.25±0.58E-3	4.96±0.66E-3	6.12±0.78E-3
MCG-05-13-004 ^b
NGC1800	8.96±0.90E-2	1.03±0.10E-1	8.34±0.83E-2	3.14±0.43E-2	2.08±0.29E-2	2.58±0.33E-2	3.57±0.45E-2	6.02±0.65E-2	1.21±0.15E 0	1.88±0.25E-1
UGCA106	1.19±0.12E-1	6.95±0.69E-2	4.99±0.50E-2	2.69±0.37E-2	1.93±0.26E-2	1.75±0.22E-2	2.51±0.31E-2	5.05±0.55E-2	8.88±1.09E-1	2.36±0.37E-1
LMC ^{a e f}	2.05±0.29E 3	1.41±0.20E 3	1.77±0.25E 3	4.81±0.75E 3	5.96±0.60E 3	1.11±0.13E 5	2.60±0.40E-1
kkh037	5.43±0.54E-3	6.24±0.62E-3	6.43±0.64E-3	2.50±0.34E-3	1.58±0.22E-3	1.35±0.18E-3	1.48±0.17E-3	2.45±0.20E-3	3.30±0.46E-2	1.25±0.17E-2
NGC2366 ^e	1.45±0.15E-1	1.47±0.15E-1	1.10±0.11E-1	6.43±0.87E-2	4.90±0.67E-2	4.95±0.63E-2	5.50±0.69E-2	6.79±0.73E-1	5.40±0.66E 0	5.05±0.70E-1
UGCA133	1.79±0.18E-2	1.65±0.17E-2	9.06±0.91E-3	4.09±0.55E-3	3.10±0.43E-3	<2.65E-3	<2.89E-3	4.81±0.44E-3	6.48±1.23E-2	2.45±0.30E-2
NGC2403 ^{e f}	2.94±0.29E 0	2.91±0.29E 0	2.39±0.24E 0	1.88±0.25E 0	1.31±0.18E 0	2.10±0.27E 0	4.11±0.51E 0	5.84±0.24E 0	8.64±0.62E 1	2.41±0.30E-1
NGC2500 ^e	1.71±0.17E-1	1.80±0.18E-1	1.39±0.14E-1	8.76±1.19E-2	5.65±0.77E-2	1.13±0.15E-1	1.69±0.21E-1	2.09±0.23E-1	3.93±0.48E 0	8.80±1.37E-1
NGC2537 ^e	1.93±0.19E-1	1.95±0.19E-1	1.60±0.16E-1	7.72±1.05E-2	5.11±0.70E-2	7.67±0.99E-2	1.41±0.18E-1	2.92±0.31E-1	4.02±0.49E 0	5.70±0.80E-1
UGC04278 ^{e f}	4.79±0.48E-2	4.52±0.45E-2	3.58±0.36E-2	2.18±0.30E-2	1.57±0.22E-2	1.65±0.22E-2	1.56±0.20E-2	3.80±0.41E-2	8.96±1.10E-1	1.58±0.25E-1
UGC04305 ^{e f}	1.66±0.17E-1	2.91±0.29E-1	2.16±0.22E-1	7.13±0.98E-2	5.66±0.78E-2	3.05±0.47E-2	2.39±0.48E-2	2.04±0.08E-1	3.60±0.26E 0	4.10±0.50E-1
NGC2552	6.62±0.66E-2	8.70±0.87E-2	5.49±0.55E-2	3.35±0.45E-2	2.27±0.31E-2	2.17±0.28E-2	1.78±0.22E-2	5.77±0.62E-2	9.79±1.20E-1	2.35±0.37E-1

Table 2—Continued

Galaxy	2MASS J 1.25 μm (Jy)	2MASS H 1.65 μm (Jy)	2MASS K _s 2.17 μm (Jy)	IRAC 3.6 μm (Jy)	IRAC 4.5 μm (Jy)	IRAC 5.8 μm (Jy)	IRAC 8.0 μm (Jy)	MIPS 24 μm (Jy)	MIPS 70 μm (Jy)	MIPS 160 μm (Jy)
M81dwA ^{e f}	3.77±0.38E-3	3.88±0.39E-3	2.92±0.29E-3	1.86±0.90E-3	9.50±9.00E-4	<3.73E-3	<2.37E-3	<1.73E-2	<1.49E-1	<1.43E-1
UGC04426	1.15±0.12E-2	1.61±0.16E-2	8.91±0.89E-3	4.58±0.62E-3	3.29±0.45E-3	<2.53E-3	3.22±0.42E-3
UGC04459 ^{e f}	7.54±0.75E-3	1.38±0.14E-2	7.93±0.79E-3	4.71±1.00E-3	3.88±1.00E-3	2.65±0.90E-3	7.32±1.00E-3	2.81±0.11E-2	3.48±0.34E-1	3.41±1.11E-1
UGC04483 ^e	5.95±0.60E-3	7.63±0.76E-3	4.19±0.42E-3	1.84±0.25E-3	9.60±1.30E-4	6.40±1.00E-4	1.13±0.15E-3	7.05±0.77E-3	1.05±0.13E-1	2.01±0.25E-1
NGC2683	2.16±0.22E 0	2.46±0.25E 0	2.10±0.21E 0	1.08±0.15E 0	6.92±0.95E-1	7.49±0.94E-1	1.18±0.15E 0
UGC04704	2.11±0.21E-2	2.76±0.28E-2	2.63±0.26E-2	8.88±1.20E-3	5.81±0.80E-3	6.18±0.81E-3	2.14±0.29E-3
UGC04787	2.59±0.26E-2	2.40±0.24E-2	1.93±0.19E-2	8.55±1.16E-3	5.86±0.81E-3	2.96±0.40E-3	5.29±0.67E-3
UGC04998	2.55±0.26E-2	3.08±0.31E-2	1.77±0.18E-2	1.08±0.15E-2	7.49±1.03E-3	5.72±0.75E-3	6.57±0.83E-3	<4.64E-3	<6.23E-2	<2.36E-1
NGC2903	3.00±0.30E 0	3.14±0.31E 0	2.74±0.27E 0	1.61±0.22E 0	1.09±0.15E 0	2.20±0.28E 0	5.11±0.64E 0	7.00±0.75E 0	7.26±0.89E 1	1.82±0.28E 1
UGC05076	1.62±0.16E-2	1.26±0.13E-2	9.06±0.91E-3	5.02±0.68E-3	3.29±0.45E-3	1.49±0.22E-3	4.59±0.58E-3
CGCG035-007	1.23±0.12E-2	1.41±0.14E-2	1.35±0.14E-2	4.27±0.58E-3	2.89±0.40E-3	1.83±0.25E-3	2.03±0.26E-3	4.46±0.50E-3	1.18±0.15E-1	1.00±0.18E-1
UGC05139 ^{e f}	3.09±0.31E-2	3.97±0.40E-2	1.60±0.16E-2	1.19±0.14E-2	7.55±1.20E-3	7.31±1.80E-3	7.54±1.60E-3	1.31±0.20E-2	4.02±0.79E-1	7.97±1.70E-1
IC0559	1.92±0.19E-2	1.72±0.17E-2	2.37±0.24E-2	8.10±1.10E-3	5.56±0.76E-3	5.24±0.69E-3	2.35±0.30E-3	5.01±0.57E-3	9.31±1.26E-2	1.49±0.26E-1
F8D1	2.96±0.30E-2	7.01±0.70E-2	1.88±0.19E-2	1.08±0.15E-2	8.75±1.20E-3	<5.59E-3	<6.15E-3	<6.78E-3	<9.11E-2	<3.44E-1
[FM2000]1	<1.85E-2	<2.56E-2	<3.14E-2	<3.60E-4	<5.30E-4	<1.95E-3	<2.13E-3	<2.36E-3	<3.18E-2	<1.20E-1
NGC2976 ^{e f}	8.60±0.86E-1	8.93±0.89E-1	7.07±0.71E-1	4.34±0.59E-1	2.84±0.39E-1	5.04±0.65E-1	1.02±0.13E 0	1.38±0.06E 0	1.99±0.14E 1	4.83±0.64E 1
LEDA166101	<8.21E-2	<1.12E-1	<1.35E-1	6.13±0.83E-3	4.10±0.56E-3	<2.68E-3	<2.94E-3	<4.87E-3	<6.53E-2	<2.46E-1
UGC05272	1.99±0.20E-2	2.57±0.26E-2	1.58±0.16E-2	7.36±1.00E-3	5.12±0.70E-3	3.78±0.50E-3	1.84±0.24E-3	1.31±0.14E-2	3.09±0.38E-1	3.09±0.50E-1
UGC05288	2.91±0.29E-2	2.34±0.23E-2	2.44±0.24E-2	8.50±1.15E-3	5.69±0.78E-3	4.95±0.65E-3	3.13±0.40E-3	1.12±0.12E-2	1.79±0.23E-1	4.27±0.68E-1
BK03N	<3.81E-3	<5.29E-3	<6.48E-3	<1.70E-4	<2.50E-4	<9.10E-4	<1.00E-3	<1.10E-3	<1.48E-2	<5.61E-2
NGC3031 ^{e f}	2.35±0.24E 1	2.55±0.25E 1	2.13±0.21E 1	1.09±0.15E 1	6.53±0.90E 0	5.88±0.75E 0	8.04±1.00E 0	5.09±0.20E 0	8.52±0.60E 1	3.56±0.43E 1
NGC3034 ^{c e f}	9.29±0.93E 0	1.08±0.11E 1	1.01±0.10E 1	7.51±1.02E 0	5.93±0.81E 0	2.45±0.31E 1	6.42±0.80E 1	>8.72E 1	>1.29E 3	>8.58E 3
UGC05340 ^e	8.67±0.87E-3	7.35±0.73E-3	<8.58E-3	2.54±0.35E-3	1.61±0.22E-3	<1.41E-3	<1.54E-3	<2.60E-3	<3.51E-2	<1.32E-1
KDG061	9.81±0.98E-3	7.28±0.73E-3	1.18±0.12E-2	4.66±0.63E-3	2.89±0.40E-3	<2.33E-3	<2.56E-3	<4.25E-3	<7.05E-2	<2.66E-1
UGC05336	2.47±0.25E-2	2.05±0.20E-2	1.47±0.15E-2	7.38±1.10E-3	3.79±1.00E-3	<1.30E-2	<1.20E-2	<3.64E-2	<2.28E-1	<4.58E-1
ArpsLoop	<4.43E-2	<6.12E-2	<7.51E-2	<3.70E-4	<5.50E-4	<2.01E-3	<2.20E-3	<3.66E-3	<4.91E-2	<1.85E-1
UGC05364 ^f	<1.35E-1	<1.90E-1	<2.36E-1	1.95±0.26E-2	1.36±0.19E-2	<7.13E-3	<7.77E-3	<6.49E-3	<8.75E-2	<3.30E-1
UGC05373 ^f	1.22±0.12E-1	1.32±0.13E-1	1.36±0.14E-1	4.97±0.67E-2	3.61±0.50E-2	1.51±0.19E-2	1.55±0.19E-2	2.10±0.23E-2	1.21±0.19E-1	1.88±0.39E-1
kkh057	<8.50E-3	<1.20E-2	<1.49E-2	6.00±0.80E-4	2.20±0.30E-4	<4.60E-4	<5.00E-4	<1.65E-3	<2.23E-2	<8.30E-2
UGCA193	1.58±0.16E-2	1.21±0.12E-2	1.91±0.19E-2	5.72±0.78E-3	3.83±0.53E-3	2.75±0.37E-3	2.35±0.31E-3	3.64±0.44E-3	4.08±0.76E-2	6.20±1.55E-2
NGC3109	5.77±0.58E-1	3.56±0.36E-1	3.44±0.34E-1	2.34±0.32E-1	1.73±0.24E-1	1.10±0.14E-1	1.20±0.15E-1	2.56±0.28E-1	6.75±0.82E 0	1.21±0.19E 1
NGC3077 ^f	1.05±0.11E 0	1.04±0.10E 0	8.70±0.87E-1	5.54±0.75E-1	3.75±0.51E-1	4.34±0.55E-1	8.11±1.01E-1
AM1001-270 ^f	<8.51E-3	<1.22E-2	<1.48E-2	3.26±0.44E-3	2.25±0.31E-3	2.80±0.29E-3	3.08±0.33E-3	3.41±0.30E-3	4.58±0.74E-2	1.73±0.25E-1

Table 2—Continued

Galaxy	2MASS J 1.25 μm (Jy)	2MASS H 1.65 μm (Jy)	2MASS K _s 2.17 μm (Jy)	IRAC 3.6 μm (Jy)	IRAC 4.5 μm (Jy)	IRAC 5.8 μm (Jy)	IRAC 8.0 μm (Jy)	MIPS 24 μm (Jy)	MIPS 70 μm (Jy)	MIPS 160 μm (Jy)
BK05N	<4.85E-2	<6.74E-2	<8.30E-2	1.69±0.23E-3	7.90±1.10E-4	<1.06E-3	<1.17E-3	<3.86E-3	<5.20E-2	<1.96E-1
UGC05428	1.41±0.14E-2	1.28±0.13E-2	1.03±0.10E-2	4.22±0.57E-3	2.63±0.36E-3	<2.42E-3	<2.64E-3	<4.85E-3	<6.51E-2	<2.46E-1
UGC05423 ^{e f}	1.20±0.12E-2	1.37±0.14E-2	1.36±0.14E-2	4.86±1.00E-3	3.43±1.00E-3	2.65±0.90E-3	2.52±0.80E-3	8.30±1.20E-3	1.40±0.34E-1	2.55±1.79E-1
UGC05442	1.51±0.15E-2	1.46±0.15E-2	1.33±0.13E-2	5.09±0.69E-3	3.55±0.49E-3	1.51±0.22E-3	3.11±0.40E-3	2.60±2.20E-4	<5.60E-2	<2.11E-1
UGC05456	3.80±0.38E-2	5.01±0.50E-2	3.10±0.31E-2	1.33±0.18E-2	9.09±1.25E-3	8.98±1.18E-3	1.04±0.13E-2	5.67±0.61E-2	6.28±0.77E-1	6.88±1.08E-1
IKN	<6.58E-2	<9.17E-2	<1.13E-1	<2.20E-4	<3.30E-4	<1.22E-3	<1.34E-3	<4.45E-3	<6.00E-2	<2.27E-1
SextansA ^{e f}	<1.69E-1	<2.44E-1	<2.98E-1	3.24±0.44E-2	2.18±0.30E-2	2.66±0.34E-2	1.77±0.22E-2	3.05±0.33E-2	7.05±0.87E-1	9.76±1.55E-1
[HS98]117	5.42±0.54E-3	6.82±0.68E-3	9.03±0.90E-3	2.87±0.39E-3	1.57±0.22E-3	<1.22E-3	<1.33E-3	<4.42E-3	<5.93E-2	<2.24E-1
NGC3239	1.60±0.16E-1	1.72±0.17E-1	1.25±0.12E-1	7.42±1.00E-2	4.97±0.68E-2	7.47±0.96E-2	8.72±1.09E-2	3.58±0.39E-1	4.95±0.60E 0	7.40±1.16E 0
DDO078	<4.45E-2	<6.27E-2	<7.79E-2	<1.90E-4	<2.80E-4	<1.03E-3	<1.12E-3	<3.74E-3	<5.04E-2	<1.91E-1
UGC05672	4.06±0.41E-2	3.45±0.34E-2	2.53±0.25E-2	1.19±0.16E-2	7.71±1.06E-3	7.16±0.94E-3	6.96±0.88E-3	8.49±0.95E-3	7.49±1.16E-2	3.93±0.63E-1
UGC05666 ^{e f}	3.36±0.34E-1	2.31±0.23E-1	1.65±0.16E-1	1.51±0.21E-1	9.05±1.27E-2	6.48±0.87E-2	6.63±0.89E-2	2.74±0.13E-1	5.19±0.43E 0	1.05±0.15E 0
UGC05692	9.28±0.93E-2	8.24±0.82E-2	6.64±0.66E-2	2.69±0.36E-2	1.77±0.24E-2	1.66±0.21E-2	1.12±0.14E-2	1.12±0.13E-2	2.98±0.38E-1	6.14±0.98E-1
NGC3274	4.24±0.42E-2	4.15±0.41E-2	3.59±0.36E-2	2.02±0.27E-2	1.35±0.19E-2	1.73±0.22E-2	2.24±0.28E-2	6.23±0.67E-2	1.25±0.15E 0	1.61±0.25E 0
BK06N	8.54±0.85E-3	<1.16E-2	<1.23E-2	2.06±0.28E-3	1.50±0.21E-3	<1.15E-3	<1.26E-3	<4.19E-3	<5.66E-2	<2.14E-1
NGC3299	8.22±0.82E-2	7.11±0.71E-2	6.80±0.68E-2	2.99±0.40E-2	2.04±0.28E-2	1.83±0.24E-2	2.83±0.35E-2	2.48±0.27E-2	3.03±0.38E-1	1.03±0.16E 0
UGC05764	6.61±0.66E-3	6.87±0.69E-3	7.29±0.73E-3	2.66±0.36E-3	1.89±0.26E-3	1.25±0.18E-3	1.02±0.14E-3	3.45±0.40E-3	6.03±0.87E-2	8.71±1.67E-1
UGC05797	1.91±0.19E-2	1.48±0.15E-2	1.17±0.12E-2	6.48±0.88E-3	4.08±0.56E-3	3.74±0.50E-3	3.01±0.39E-3	4.29±0.50E-3	1.11±0.15E-1	2.27±0.37E-1
UGC05829	5.48±0.55E-2	3.74±0.37E-2	2.22±0.22E-2	1.36±0.18E-2	9.20±1.26E-3	5.90±0.77E-3	6.46±0.82E-3	3.16±0.34E-2	7.17±0.88E-1	9.06±1.43E-1
NGC3344 ^e	9.42±0.94E-1	8.91±0.89E-1	6.94±0.69E-1	4.01±0.54E-1	2.49±0.34E-1	4.74±0.60E-1	9.74±1.21E-1	1.18±0.13E 0	1.51±0.18E 1	5.12±0.80E 1
NGC3351 ^{e f}	1.68±0.17E 0	1.77±0.18E 0	1.54±0.15E 0	8.13±1.10E-1	5.14±0.71E-1	7.20±0.93E-1	1.34±0.16E 0	2.49±0.12E 0	2.29±0.19E 1	6.11±0.83E 1
NGC3368 ^e	2.29±0.23E 0	2.52±0.25E 0	2.11±0.21E 0	1.09±0.15E 0	6.65±0.91E-1	6.84±0.87E-1	8.86±1.10E-1	7.82±0.84E-1	1.41±0.17E 1	4.77±0.75E 1
UGC05889	3.39±0.34E-2	3.91±0.39E-2	3.03±0.30E-2	1.34±0.18E-2	8.66±1.19E-3	6.37±0.83E-3	4.35±0.56E-3	8.05±0.91E-3	<7.03E-2	<2.66E-1
UGC05923 ^e	2.63±0.26E-2	2.92±0.29E-2	2.18±0.22E-2	9.64±1.31E-3	6.38±0.88E-3	6.03±0.80E-3	9.36±1.19E-3	1.09±0.12E-2	2.46±0.30E-1	2.33±0.37E-1
UGC05918	<3.53E-2	<4.00E-2	<4.97E-2	3.00±0.41E-3	2.00±0.28E-3	<1.83E-3	<2.00E-3	<3.33E-3	<4.50E-2	<1.70E-1
NGC3432	2.03±0.20E-1	2.10±0.21E-1	1.71±0.17E-1	1.02±0.14E-1	7.38±1.01E-2	1.36±0.17E-1	2.29±0.29E-1	5.99±0.65E-1	9.67±1.18E 0	1.85±0.29E 0
KDG073	<2.85E-2	<4.02E-2	<5.00E-2	1.94±0.26E-3	6.10±0.80E-4	<8.20E-4	<9.00E-4	<2.98E-3	<4.03E-2	<1.52E-1
NGC3486 ^e	4.80±0.48E-1	5.82±0.58E-1	4.47±0.45E-1	2.36±0.32E-1	1.58±0.22E-1	2.60±0.33E-1	5.88±0.73E-1	6.41±0.69E-1	9.65±1.18E 0	2.70±0.42E 0
NGC3510	5.82±0.58E-2	3.81±0.38E-2	2.32±0.23E-2	2.07±0.28E-2	1.45±0.20E-2	1.52±0.20E-2	2.31±0.29E-2	5.34±0.58E-2	1.18±0.14E 0	1.82±0.28E 0
NGC3521 ^{e f}	3.74±0.37E 0	4.22±0.42E 0	3.50±0.35E 0	2.05±0.28E 0	1.36±0.19E 0	2.53±0.32E 0	6.27±0.76E 0	5.51±0.22E 0	6.26±0.45E 1	2.12±0.27E 1
NGC3593 ^e	7.76±0.78E-1	9.45±0.94E-1	7.66±0.77E-1	3.75±0.51E-1	2.51±0.34E-1	5.26±0.67E-1	1.21±0.15E 0	1.69±0.18E 0	2.22±0.27E 1	3.31±0.52E 1
NGC3623	2.89±0.29E 0	3.20±0.32E 0	2.65±0.27E 0	1.27±0.17E 0	7.95±1.09E-1	7.43±0.94E-1	7.67±0.96E-1	5.55±0.60E-1	7.01±0.86E 0	3.57±0.56E 0
NGC3627 ^{e f}	3.34±0.33E 0	3.73±0.37E 0	3.17±0.32E 0	1.87±0.25E 0	1.25±0.17E 0	2.35±0.30E 0	5.58±0.69E 0	7.43±0.30E 0	9.22±0.70E 1	2.20±0.28E 1

Table 2—Continued

Galaxy	2MASS J 1.25 μm (Jy)	2MASS H 1.65 μm (Jy)	2MASS K _s 2.17 μm (Jy)	IRAC 3.6 μm (Jy)	IRAC 4.5 μm (Jy)	IRAC 5.8 μm (Jy)	IRAC 8.0 μm (Jy)	MIPS 24 μm (Jy)	MIPS 70 μm (Jy)	MIPS 160 μm (Jy)
NGC3628	2.43±0.24E 0	2.98±0.30E 0	2.66±0.27E 0	1.52±0.21E 0	1.04±0.14E 0	1.86±0.23E 0	4.08±0.51E 0	5.10±0.55E 0	6.26±0.76E 1	1.90±0.3
UGC06457	1.52±0.15E-2	1.65±0.17E-2	1.18±0.12E-2	5.52±0.75E-3	3.13±0.43E-3	2.92±0.39E-3	2.31±0.30E-3	2.07±0.29E-3	1.09±0.14E-1	1.39±0.2
UGC06541 ^e	1.13±0.11E-2	1.26±0.13E-2	1.26±0.13E-2	5.28±0.72E-3	3.88±0.53E-3	1.98±0.27E-3	2.29±0.30E-3	6.57±0.72E-3	1.95±0.24E-1	7.30±1.4
NGC3738 ^e	1.32±0.13E-1	1.40±0.14E-1	1.04±0.10E-1	6.03±0.82E-2	4.02±0.55E-2	4.22±0.55E-2	5.09±0.64E-2	1.24±0.13E-1	2.71±0.33E 0	3.21±0.5
NGC3741	1.13±0.11E-2	1.83±0.18E-2	1.12±0.11E-2	4.61±0.63E-3	3.19±0.44E-3	2.20±0.30E-3	1.16±0.16E-3	5.71±0.64E-3	1.75±0.22E-1	1.20±0.2
UGC06782	<3.29E-2	<4.63E-2	<5.74E-2	2.76±0.38E-3	1.90±0.26E-3	1.46±0.17E-3	1.58±0.25E-3	2.64±0.18E-3	3.57±0.49E-2	1.35±0.1
UGC06817	2.33±0.23E-2	2.62±0.26E-2	2.15±0.22E-2	9.23±1.25E-3	5.51±0.76E-3	4.28±0.57E-3	2.21±0.30E-3	7.25±0.83E-3	1.33±0.18E-1	2.28±0.4
UGC06900	2.38±0.24E-2	1.82±0.18E-2	1.81±0.18E-2	7.68±1.04E-3	5.39±0.74E-3	5.47±0.72E-3	4.25±0.54E-3	4.13±0.51E-3	<6.16E-2	<2.3
NGC4020	6.58±0.66E-2	5.44±0.54E-2	5.91±0.59E-2	3.12±0.42E-2	2.04±0.28E-2	3.40±0.44E-2	6.82±0.86E-2	9.39±1.01E-2	1.25±0.15E 0	3.66±0.5
NGC4068	5.05±0.50E-2	4.16±0.42E-2	3.72±0.37E-2	2.42±0.33E-2	1.69±0.23E-2	1.20±0.16E-2	9.10±1.15E-3	3.22±0.35E-2	7.02±0.86E-1	9.26±1.4
NGC4080	5.25±0.52E-2	5.12±0.51E-2	3.45±0.34E-2	1.85±0.25E-2	1.21±0.17E-2	1.77±0.23E-2	3.94±0.50E-2	3.47±0.38E-2	4.34±0.53E-1	1.46±0.2
NGC4096	5.58±0.56E-1	6.22±0.62E-1	5.35±0.54E-1	2.91±0.39E-1	2.00±0.27E-1	3.91±0.50E-1	8.77±1.09E-1	8.74±0.94E-1	1.09±0.13E 1	4.08±0.6
NGC4144 ^e	1.60±0.16E-1	1.55±0.16E-1	1.24±0.12E-1	7.01±0.95E-2	4.81±0.66E-2	4.45±0.57E-2	6.14±0.77E-2	1.13±0.12E-1	2.37±0.29E 0	5.12±0.8
NGC4163	5.98±0.60E-2	4.39±0.44E-2	3.26±0.33E-2	1.73±0.23E-2	1.15±0.16E-2	7.26±0.95E-3	5.64±0.71E-3	1.24±0.14E-2	1.78±0.23E-1	3.38±0.4
NGC4190	5.96±0.60E-2	4.99±0.50E-2	3.69±0.37E-2	1.83±0.25E-2	1.20±0.16E-2	9.91±1.29E-3	5.83±0.74E-3	1.78±0.19E-2	5.65±0.69E-1	9.94±1.1
ESO321-G014	1.18±0.12E-2	9.34±0.93E-3	<7.33E-2	5.08±0.69E-3	3.52±0.48E-3	9.10±1.50E-4	1.17±0.17E-3	4.00±1.90E-4	<4.79E-2	<1.8
UGC07242	<2.97E-2	<4.19E-2	<4.96E-2	<1.50E-4	<2.30E-4	<8.50E-4	<9.20E-4	<3.07E-3	<4.15E-2	<1.5
UGCA276	1.24±0.12E-2	7.66±0.77E-3	4.49±0.45E-3	2.69±0.36E-3	1.52±0.21E-3	<1.10E-3	<1.21E-3	<4.02E-3	<5.42E-2	<2.0
UGC07267	2.50±0.25E-2	1.98±0.20E-2	1.75±0.18E-2	7.27±0.99E-3	4.82±0.66E-3	2.65±0.36E-3	1.73±0.23E-3	3.57±0.43E-3	6.92±1.02E-2	1.80±0.3
NGC4214 ^e	5.86±0.59E-1	6.39±0.64E-1	4.88±0.49E-1	3.11±0.42E-1	2.14±0.29E-1	3.27±0.41E-1	5.43±0.68E-1	2.00±0.22E 0	2.20±0.27E 1	3.79±0.5
CGCG269-049 ^{e f}	4.91±0.49E-3	6.62±0.66E-3	3.31±0.33E-3	1.49±0.20E-3	1.16±0.16E-3	6.30±1.00E-4	6.20±0.90E-4	2.87±0.33E-3	4.63±0.65E-2	<1.0
NGC4236 ^{e f}	6.35±0.63E-1	8.31±0.83E-1	5.70±0.57E-1	2.50±0.34E-1	2.10±0.29E-1	1.07±0.14E-1	2.16±0.27E-1	5.47±0.22E-1	8.18±0.59E 0	1.96±0.2
NGC4244 ^{e f}	6.73±0.67E-1	6.86±0.69E-1	5.78±0.58E-1	3.05±0.41E-1	2.10±0.29E-1	2.08±0.26E-1	2.87±0.36E-1	4.58±0.49E-1	7.44±0.91E 0	2.35±0.3
NGC4242 ^e	1.94±0.19E-1	2.40±0.24E-1	1.60±0.16E-1	1.03±0.14E-1	6.15±0.84E-2	6.34±0.81E-2	9.90±1.23E-2	1.07±0.12E-1	1.98±0.24E 0	7.00±1.0
UGC07321 ^{e f}	4.37±0.44E-2	4.75±0.47E-2	3.86±0.39E-2	2.28±0.31E-2	1.46±0.20E-2	1.71±0.22E-2	2.37±0.30E-2	2.98±0.32E-2	5.87±0.72E-1	1.99±0.3
NGC4248	8.41±0.84E-2	7.31±0.73E-2	6.94±0.69E-2	4.13±0.56E-2	2.50±0.34E-2	2.43±0.31E-2	3.09±0.39E-2	3.43±0.37E-2	4.95±0.61E-1	1.28±0.2
NGC4258 ^e	5.03±0.50E 0	5.50±0.55E 0	4.63±0.46E 0	2.28±0.31E 0	1.50±0.21E 0	1.18±0.15E 0	2.52±0.31E 0	2.77±0.30E 0	3.95±0.48E 1	1.40±0.2
ISZ399	3.54±0.35E-2	3.99±0.40E-2	3.45±0.34E-2	2.26±0.31E-2	1.60±0.22E-2	4.91±0.65E-2	1.22±0.15E-1	4.36±0.47E-1	2.92±0.36E 0	2.22±0.3
NGC4288	5.35±0.54E-2	6.46±0.65E-2	3.25±0.33E-2	2.38±0.32E-2	1.53±0.21E-2	2.28±0.30E-2	4.15±0.52E-2	6.80±0.73E-2	1.37±0.17E 0	2.71±0.4
UGC07408	4.48±0.45E-2	3.67±0.37E-2	3.29±0.33E-2	1.31±0.18E-2	7.74±1.06E-3	6.22±0.81E-3	5.04±0.64E-3	<5.46E-3	<7.36E-2	<1.2
UGC07490	7.21±0.72E-2	8.07±0.81E-2	6.83±0.68E-2	2.48±0.34E-2	1.68±0.23E-2	1.57±0.20E-2	1.88±0.23E-2	2.24±0.24E-2	3.86±0.48E-1	1.39±0.2
NGC4395	4.68±0.47E-1	4.45±0.44E-1	3.20±0.32E-1	3.20±0.43E-1	2.54±0.35E-1	2.49±0.31E-1	2.59±0.32E-1	5.09±0.55E-1	1.06±0.13E 1	2.73±0.4
UGCA281 ^f	7.42±0.74E-3	8.22±0.82E-3	7.28±0.73E-3	3.64±0.50E-3	2.64±0.36E-3	1.79±0.25E-3	1.77±0.23E-3	6.12±0.66E-2	4.47±0.55E-1	1.73±0.2

Table 2—Continued

Galaxy	2MASS J 1.25 μm (Jy)	2MASS H 1.65 μm (Jy)	2MASS K _s 2.17 μm (Jy)	IRAC 3.6 μm (Jy)	IRAC 4.5 μm (Jy)	IRAC 5.8 μm (Jy)	IRAC 8.0 μm (Jy)	MIPS 24 μm (Jy)	MIPS 70 μm (Jy)	MIPS 160 μm (Jy)
UGC07559	1.50±0.15E-2	1.50±0.15E-2	1.12±0.11E-2	5.95±0.81E-3	3.78±0.52E-3	2.13±0.29E-3	1.83±0.24E-3	6.45±0.72E-3	1.51±0.19E-1	1.74±0.29E-
UGC07577	7.76±0.78E-2	7.78±0.78E-2	4.19±0.42E-2	2.60±0.35E-2	1.48±0.20E-2	7.79±1.01E-3	4.08±0.53E-3	7.97±0.93E-3	1.01±0.16E-1	4.69±0.77E-
NGC4449 ^e	1.03±0.10E 0	1.11±0.11E 0	8.93±0.89E-1	4.81±0.65E-1	3.14±0.43E-1	6.32±0.80E-1	1.35±0.17E 0	3.21±0.35E 0	4.49±0.55E 1	8.43±1.32E
UGC07599	6.60±0.66E-3	9.16±0.92E-3	4.01±0.40E-3	2.71±0.37E-3	1.49±0.21E-3	2.35±0.24E-3	2.56±0.26E-3	2.13±0.15E-3	2.88±0.40E-2	1.09±0.15E-
UGC07605	1.39±0.14E-2	1.11±0.11E-2	6.09±0.61E-3	4.31±0.59E-3	2.41±0.33E-3	1.61±0.19E-3	1.76±0.20E-3	1.63±0.23E-3	5.60±0.82E-2	1.49±0.21E-
NGC4455	5.22±0.52E-2	5.47±0.55E-2	4.28±0.43E-2	2.17±0.30E-2	1.46±0.20E-2	1.36±0.18E-2	1.62±0.20E-2	3.41±0.37E-2	9.52±1.16E-1	1.95±0.30E
UGC07608	2.12±0.21E-2	1.55±0.15E-2	1.49±0.15E-2	5.57±0.76E-3	3.62±0.50E-3	2.62±0.35E-3	3.49±0.45E-3	1.94±0.21E-2	2.36±0.29E-1	3.15±0.51E-
NGC4460 ^e	1.92±0.19E-1	2.03±0.20E-1	1.95±0.19E-1	8.35±1.13E-2	5.62±0.77E-2	7.77±1.00E-2	1.24±0.16E-1	3.05±0.33E-1	3.71±0.45E 0	5.42±0.85E
UGC07639	2.54±0.25E-2	2.67±0.27E-2	2.64±0.26E-2	1.14±0.15E-2	7.69±1.06E-3	4.53±0.60E-3	3.29±0.42E-3	5.57±0.65E-3	1.19±0.16E-1	1.19±0.24E-
NGC4485 ^e	9.47±0.95E-2	9.93±0.99E-2	6.95±0.69E-2	4.25±0.58E-2	2.97±0.41E-2	5.72±0.75E-2	9.46±1.19E-2	1.87±0.20E-1	3.09±0.38E 0	9.62±1.50E
NGC4490 ^e	9.34±0.93E-1	9.35±0.93E-1	8.14±0.81E-1	4.71±0.64E-1	3.23±0.44E-1	7.92±1.01E-1	1.69±0.21E 0	4.29±0.46E 0	6.29±0.77E 1	1.07±0.17E
UGC07690	4.76±0.48E-2	5.26±0.53E-2	2.77±0.28E-2	1.86±0.25E-2	1.26±0.17E-2	1.09±0.14E-2	1.18±0.15E-2	3.01±0.33E-2	7.88±0.96E-1	1.18±0.18E
UGC07699	5.39±0.54E-2	7.75±0.77E-2	5.35±0.54E-2	2.24±0.30E-2	1.43±0.20E-2	1.50±0.19E-2	2.00±0.25E-2	3.75±0.41E-2	7.21±0.88E-1	1.54±0.24E
UGC07698	2.61±0.26E-2	2.58±0.26E-2	2.11±0.21E-2	8.48±1.15E-3	6.98±0.96E-3	4.84±0.91E-3	1.08±0.14E-2	9.86±1.09E-3	1.81±0.23E-1	4.04±0.65E-
UGC07719	1.02±0.10E-2	1.76±0.18E-2	8.71±0.87E-3	4.66±0.63E-3	3.10±0.43E-3	1.71±0.24E-3	1.22±0.17E-3	1.34±0.14E-2	2.20±0.27E-1	1.31±0.23E-
UGC07774	2.03±0.20E-2	2.81±0.28E-2	1.48±0.15E-2	9.08±1.23E-3	5.52±0.76E-3	3.97±0.53E-3	5.24±0.67E-3	9.34±1.02E-3	1.44±0.18E-1	3.68±0.58E-
UGCA292 ^{e f}	<5.69E-3	<8.04E-3	<1.00E-2	1.68±0.23E-3	5.80±0.80E-4	<6.80E-4	3.00±0.39E-3	<2.47E-3	3.91±0.61E-2	<1.26E-
NGC4594 ^{e f}	8.07±0.81E 0	9.20±0.92E 0	7.56±0.76E 0	3.94±0.53E 0	2.31±0.32E 0	1.73±0.22E 0	1.30±0.16E 0	6.74±0.43E-1	7.36±0.68E 0	3.61±0.56E
NGC4605	6.49±0.65E-1	6.92±0.69E-1	5.61±0.56E-1	3.25±0.44E-1	2.27±0.31E-1	3.88±0.49E-1	7.36±0.92E-1	1.05±0.11E 0	2.04±0.25E 1	3.74±0.58E
NGC4618 ^e	2.81±0.28E-1	3.26±0.33E-1	2.44±0.24E-1	1.58±0.21E-1	1.04±0.14E-1	1.72±0.22E-1	3.27±0.41E-1	4.01±0.43E-1	7.89±0.96E 0	1.73±0.27E
NGC4625 ^{e f}	9.82±0.98E-2	1.13±0.11E-1	8.98±0.90E-2	4.85±0.64E-2	3.02±0.40E-2	5.85±0.76E-2	1.29±0.16E-1	1.36±0.06E-1	2.07±0.16E 0	5.07±0.68E
NGC4631 ^{e f}	1.75±0.17E 0	1.98±0.20E 0	1.84±0.18E 0	1.26±0.17E 0	8.36±1.15E-1	2.45±0.31E 0	5.86±0.73E 0	8.15±0.33E 0	1.30±0.10E 2	2.76±0.35E
UGC07866	2.26±0.23E-2	2.87±0.29E-2	3.16±0.32E-2	8.46±1.15E-3	5.12±0.70E-3	2.53±0.34E-3	2.86±0.37E-3	6.76±0.76E-3	2.42±0.30E-1	2.35±0.39E-
NGC4656	2.01±0.20E-1	1.90±0.19E-1	1.35±0.14E-1	9.54±1.29E-2	7.05±0.97E-2	7.65±0.97E-2	1.02±0.13E-1	5.41±0.58E-1	9.23±1.13E 0	1.23±0.19E
UGC07916	<3.46E-2	<4.89E-2	<6.08E-2	2.51±0.34E-3	1.71±0.24E-3	9.50±1.30E-4	1.06±0.14E-3	6.33±0.69E-3	6.98±0.91E-2	8.10±1.42E-
UGC07950	3.63±0.36E-2	4.17±0.42E-2	3.19±0.32E-2	1.07±0.14E-2	7.41±1.02E-3	7.12±0.94E-3	4.30±0.55E-3	1.16±0.13E-2	3.03±0.37E-1	4.16±0.66E-
UGC07949	9.22±0.92E-3	1.05±0.10E-2	6.88±0.69E-3	3.24±0.44E-3	<8.20E-4	<1.51E-3	<1.64E-3	2.19±0.28E-3	<3.68E-2	<1.39E-
NGC4707	2.39±0.24E-2	2.30±0.23E-2	1.62±0.16E-2	1.09±0.15E-2	6.28±0.86E-3	5.09±0.67E-3	4.30±0.55E-3	1.11±0.12E-2	2.28±0.29E-1	4.67±0.75E-
NGC4736 ^{e f}	6.95±0.69E 0	7.68±0.77E 0	6.44±0.64E 0	3.60±0.49E 0	2.32±0.32E 0	2.72±0.35E 0	5.17±0.64E 0	5.65±0.23E 0	9.39±0.73E 1	1.74±0.21E
UGC08024 ^{e f}	9.92±0.99E-3	1.24±0.12E-2	1.20±0.12E-2	4.07±1.00E-3	2.99±1.00E-3	<5.81E-3	<3.99E-3	7.40±1.10E-3	5.70±5.02E-2	2.62±1.25E-
NGC4826 ^{e f}	5.68±0.57E 0	6.31±0.63E 0	5.28±0.53E 0	2.52±0.34E 0	1.57±0.22E 0	1.64±0.21E 0	2.35±0.29E 0	2.52±0.15E 0	5.07±0.51E 1	8.70±1.27E
UGC08091 ^f	8.86±0.89E-3	1.21±0.12E-2	8.40±0.84E-3	3.06±0.42E-3	2.29±0.32E-3	1.57±0.22E-3	1.47±0.20E-3	4.29±0.49E-3	1.56±0.20E-1	1.48±0.25E-
UGCA319	1.22±0.12E-2	1.39±0.14E-2	1.28±0.13E-2	5.50±0.75E-3	3.51±0.48E-3	2.50±0.34E-3	5.15±0.65E-3	<2.55E-3	<3.43E-2	<1.30E-

Table 2—Continued

Galaxy	2MASS J 1.25 μm (Jy)	2MASS H 1.65 μm (Jy)	2MASS K _s 2.17 μm (Jy)	IRAC 3.6 μm (Jy)	IRAC 4.5 μm (Jy)	IRAC 5.8 μm (Jy)	IRAC 8.0 μm (Jy)	MIPS 24 μm (Jy)	MIPS 70 μm (Jy)	MIPS 160 μm (Jy)
UGCA320	3.51±0.35E-2	4.67±0.47E-2	<3.27E-1	1.80±0.24E-2	1.45±0.20E-2	3.23±0.42E-3	3.42±0.43E-3	2.33±0.25E-2	5.17±0.63E-1	4.92±0.70E-1
UGC08188	1.18±0.12E-1	1.70±0.17E-1	1.22±0.12E-1	5.96±0.81E-2	4.47±0.61E-2	4.11±0.52E-2	3.56±0.44E-2	6.88±0.74E-2	1.52±0.19E 0	2.88±0.43E-1
UGC08201 ^{e f}	3.20±0.32E-2	4.69±0.47E-2	3.73±0.37E-2	1.56±0.23E-2	1.18±0.15E-2	5.35±1.70E-3	4.08±0.80E-3	1.42±0.10E-2	1.43±0.69E-1	2.88±2.58E-1
MCG-03-34-002	1.72±0.17E-2	1.78±0.18E-2	2.22±0.22E-2	7.24±0.98E-3	5.10±0.70E-3	4.03±0.54E-3	2.93±0.38E-3	6.79±0.74E-3	1.15±0.15E-1	1.09±0.19E-1
UGC08245	1.78±0.18E-2	1.67±0.17E-2	1.39±0.14E-2	9.41±1.28E-3	5.98±0.82E-3	2.63±0.36E-3	2.89±0.37E-3	4.22±0.50E-3	9.64±1.32E-2	2.42±0.40E-1
NGC5023 ^e	9.86±0.99E-2	1.04±0.10E-1	8.98±0.90E-2	4.50±0.61E-2	2.87±0.39E-2	2.48±0.32E-2	1.99±0.25E-2	5.68±0.61E-2	9.49±1.16E-1	2.30±0.30E-1
CGCG217-018	1.60±0.16E-2	2.13±0.21E-2	1.62±0.16E-2	6.64±0.90E-3	4.24±0.58E-3	3.89±0.52E-3	4.72±0.60E-3	1.19±0.13E-2	1.70±0.21E-1	1.91±0.30E-1
UGC08313	1.81±0.18E-2	2.88±0.29E-2	2.41±0.24E-2	9.25±1.25E-3	5.89±0.81E-3	5.70±0.75E-3	7.10±0.90E-3	2.78±0.30E-2	2.36±0.29E-1	3.57±0.57E-1
UGC08320	5.83±0.58E-2	6.20±0.62E-2	5.02±0.50E-2	1.98±0.27E-2	1.47±0.20E-2	5.37±0.71E-3	7.10±0.90E-3	1.69±0.19E-2	5.64±0.70E-1	7.76±1.20E-1
UGC08331	2.18±0.22E-2	2.33±0.23E-2	1.58±0.16E-2	6.45±0.87E-3	4.49±0.62E-3	2.25±0.31E-3	2.21±0.29E-3	6.98±0.79E-3	1.67±0.22E-1	3.85±0.63E-1
NGC5055 ^{e f}	4.21±0.42E 0	4.96±0.50E 0	4.05±0.41E 0	2.38±0.32E 0	1.55±0.21E 0	2.63±0.34E 0	5.64±0.70E 0	5.74±0.23E 0	7.27±0.52E 1	2.95±0.37E-1
NGC5068	8.64±0.86E-1	8.12±0.81E-1	7.10±0.71E-1	4.59±0.62E-1	3.26±0.45E-1	4.87±0.61E-1	1.24±0.15E 0	1.37±0.15E 0	2.08±0.25E 1	5.42±0.80E-1
IC4247	1.85±0.19E-2	1.57±0.16E-2	1.39±0.14E-2	6.36±0.86E-3	4.33±0.60E-3	2.07±0.28E-3	1.90±0.25E-3
NGC5204 ^e	1.43±0.14E-1	1.48±0.15E-1	1.12±0.11E-1	6.80±0.92E-2	4.59±0.63E-2	5.04±0.65E-2	8.22±1.03E-2	1.78±0.19E-1	4.01±0.49E 0	7.36±1.14E-1
NGC5194 ^{e f}	4.99±0.50E 0	5.89±0.59E 0	4.52±0.45E 0	2.66±0.36E 0	1.80±0.26E 0	4.23±0.54E 0	1.06±0.13E 1	1.27±0.05E 1	1.47±0.11E 2	4.91±0.60E-1
NGC5195 ^{e f}	2.37±0.24E 0	2.80±0.28E 0	2.25±0.23E 0	8.34±1.13E-1	5.11±0.70E-1	4.62±0.61E-1	6.46±0.81E-1	1.39±0.27E 0	1.55±0.33E 1	1.34±0.30E-1
UGC08508	2.18±0.22E-2	2.13±0.21E-2	1.39±0.14E-2	8.43±1.14E-3	5.10±0.70E-3	3.91±0.52E-3	4.27±0.54E-3	6.27±0.70E-3	1.46±0.19E-1	1.95±0.33E-1
NGC5229	3.60±0.36E-2	4.76±0.48E-2	4.23±0.42E-2	1.31±0.18E-2	8.57±1.18E-3	7.39±0.97E-3	8.07±1.02E-3	1.66±0.18E-2	3.56±0.44E-1	5.54±0.80E-1
NGC5238	4.44±0.44E-2	5.07±0.51E-2	3.47±0.35E-2	1.23±0.17E-2	8.72±1.20E-3	8.29±1.08E-3	5.30±0.67E-3	1.63±0.18E-2	4.01±0.50E-1	7.38±1.10E-1
[KK98]208	<2.20E-1	<3.19E-1	<3.91E-1	<3.10E-4	<4.60E-4	<1.70E-3	<1.86E-3
NGC5236 ^f	1.13±0.11E 1	1.26±0.13E 1	1.04±0.10E 1	6.23±0.84E 0	4.11±0.56E 0	9.49±1.18E 0	2.41±0.30E 1	3.96±0.43E 1	3.50±0.43E 2	7.93±1.20E-1
ESO444-G084	<1.54E-2	<2.21E-2	<2.69E-2	2.79±0.38E-3	1.76±0.24E-3	1.59±0.22E-3	6.30±0.90E-4
UGC08638	1.32±0.13E-2	2.29±0.23E-2	1.52±0.15E-2	7.48±1.01E-3	5.01±0.69E-3	2.77±0.37E-3	2.24±0.29E-3	9.00±0.99E-3	1.41±0.18E-1	2.30±0.30E-1
UGC08651	2.09±0.21E-2	1.59±0.16E-2	1.59±0.16E-2	5.93±0.80E-3	3.91±0.54E-3	1.79±0.24E-3	1.35±0.18E-3	3.41±0.40E-3	7.38±1.13E-2	1.30±0.20E-1
NGC5253 ^e	4.40±0.44E-1	4.44±0.44E-1	3.54±0.35E-1	2.42±0.33E-1	2.62±0.36E-1	5.38±0.69E-1	8.07±1.01E-1
NGC5264	1.50±0.15E-1	1.15±0.12E-1	1.08±0.11E-1	5.31±0.72E-2	3.68±0.50E-2	3.60±0.46E-2	4.22±0.53E-2
UGC08760	1.48±0.15E-2	1.29±0.13E-2	1.59±0.16E-2	6.10±0.83E-3	4.36±0.60E-3	2.08±0.28E-3	1.35±0.18E-3	1.19±0.14E-3	<5.58E-2	<2.10E-1
kkh086	<2.53E-2	<3.56E-2	<4.41E-2	1.29±0.18E-3	7.20±1.00E-4	<7.60E-4	<8.30E-4	<2.76E-3	<3.72E-2	<1.40E-1
UGC08837	3.44±0.34E-2	2.27±0.23E-2	2.65±0.26E-2	1.56±0.21E-2	1.00±0.14E-2	7.17±0.94E-3	1.06±0.13E-2	1.90±0.21E-2	2.86±0.36E-1	7.69±1.20E-1
UGC08833	1.20±0.12E-2	6.30±0.63E-3	3.43±0.34E-3	2.45±0.33E-3	2.05±0.28E-3	<1.73E-3	<1.89E-3	<3.14E-3	<4.24E-2	<1.60E-1
NGC5457 ^{e f}	4.38±0.44E 0	5.04±0.50E 0	4.41±0.44E 0	2.52±0.34E 0	1.74±0.24E 0	3.40±0.42E 0	7.48±0.93E 0	1.03±0.11E 1	1.14±0.14E 2	3.96±0.63E-1
NGC5474 ^{e f}	1.43±0.14E-1	1.59±0.16E-1	1.14±0.11E-1	1.04±0.14E-1	7.34±1.02E-2	7.59±1.01E-2	1.17±0.15E-1	1.84±0.08E-1	3.72±0.27E 0	9.87±1.20E-1
NGC5477 ^f	2.39±0.24E-2	2.47±0.25E-2	2.20±0.22E-2	7.41±1.01E-3	5.16±0.71E-3	4.19±0.56E-3	2.60±0.34E-3	1.72±0.19E-2	4.25±0.52E-1	4.38±0.70E-1

Table 2—Continued

Galaxy	2MASS J 1.25 μm (Jy)	2MASS H 1.65 μm (Jy)	2MASS K _s 2.17 μm (Jy)	IRAC 3.6 μm (Jy)	IRAC 4.5 μm (Jy)	IRAC 5.8 μm (Jy)	IRAC 8.0 μm (Jy)	MIPS 24 μm (Jy)	MIPS 70 μm (Jy)	MIPS 160 μm (Jy)
[KK98]230	<7.67E-3	<1.08E-2	<1.35E-2	4.60±0.60E-4	3.30±0.50E-4	<8.60E-4	<9.40E-4	<3.44E-3	<4.64E-2	<1.75E-1
UGC09128 ^e	1.30±0.13E-2	9.19±0.92E-3	9.25±0.93E-3	3.10±0.42E-3	2.39±0.33E-3	<1.54E-3	<1.68E-3	<2.80E-3	<3.78E-2	<1.43E-1
NGC5585 ^e	1.45±0.14E-1	1.57±0.16E-1	1.12±0.11E-1	8.69±1.18E-2	5.87±0.81E-2	6.56±0.84E-2	8.89±1.11E-2	1.38±0.15E-1	3.00±0.37E 0	7.46±1.17E-1
UGC09240	4.80±0.48E-2	4.17±0.42E-2	3.32±0.33E-2	1.55±0.21E-2	1.07±0.15E-2	7.95±1.04E-3	7.80±0.98E-3	2.32±0.25E-2	3.60±0.45E-1	4.96±0.79E-1
UGC09405	1.51±0.15E-2	2.01±0.20E-2	1.29±0.13E-2	6.67±0.90E-3	3.98±0.55E-3	2.73±0.37E-3	3.74±0.48E-3	4.57±0.54E-3	5.66±0.97E-2	1.65±0.30E-1
MRK475	2.26±0.23E-3	2.00±0.20E-3	1.42±0.14E-3	9.80±1.30E-4	8.00±1.10E-4	5.40±0.90E-4	8.20±1.10E-4	9.27±1.00E-3	1.14±0.14E-1	4.15±0.89E-1
NGC5832	1.07±0.11E-1	1.09±0.11E-1	9.68±0.97E-2	4.50±0.61E-2	2.92±0.40E-2	2.98±0.38E-2	4.59±0.57E-2	4.39±0.47E-2	8.13±1.00E-1	2.68±0.42E-1
NGC5949	1.39±0.14E-1	1.47±0.15E-1	1.21±0.12E-1	7.01±0.95E-2	4.48±0.62E-2	7.55±0.98E-2	1.50±0.19E-1	1.44±0.16E-1	2.18±0.27E 0	6.11±0.95E-1
UGC09992	1.14±0.11E-2	9.90±0.99E-3	9.72±0.97E-3	4.80±0.65E-3	3.24±0.45E-3	1.51±0.21E-3	3.79±0.48E-3	6.79±0.75E-3	1.16±0.15E-1	1.37±0.24E-1
KKR25 ^{e f}	<1.89E-2	<2.68E-2	<3.34E-2	<2.40E-4	<3.60E-4	<1.32E-3	<1.44E-3	<2.40E-3	<3.24E-2	<1.22E-1
NGC6503 ^e	9.49±0.95E-1	1.05±0.10E 0	8.60±0.86E-1	4.34±0.59E-1	2.91±0.40E-1	5.01±0.64E-1	9.28±1.16E-1	8.65±0.93E-1	1.44±0.18E 1	3.58±0.56E-1
IC4951	3.47±0.35E-2	3.60±0.36E-2	3.44±0.34E-2	1.02±0.14E-2	7.20±0.99E-3	5.75±0.76E-3	3.53±0.45E-3
DDO210 ^f	<2.59E-2	<3.75E-2	<4.59E-2	2.80±0.38E-3	1.69±0.23E-3	<1.55E-3	<1.69E-3	<2.82E-3	<3.79E-2	<1.43E-1
IC5052 ^e	2.38±0.24E-1	2.47±0.25E-1	2.01±0.20E-1	1.24±0.17E-1	8.65±1.19E-2	9.01±1.16E-2	1.39±0.17E-1	3.82±0.41E-1	4.56±0.56E 0	8.52±1.33E-1
NGC7064	6.58±0.66E-2	4.87±0.49E-2	4.41±0.44E-2	2.37±0.32E-2	1.54±0.21E-2	1.12±0.15E-2	1.19±0.15E-2	3.24±0.35E-2	1.01±0.12E 0	1.93±0.21E-1
NGC7090 ^e	4.34±0.43E-1	4.83±0.48E-1	3.92±0.39E-1	2.18±0.30E-1	1.45±0.20E-1	2.49±0.32E-1	4.87±0.61E-1	6.53±0.70E-1	1.03±0.13E 1	2.84±0.44E-1
IC5152 ^{d e}	4.60±0.46E-1	3.37±0.34E-1	3.06±0.31E-1	...	1.66±0.23E-1	...	2.27±0.28E-1	2.09±0.23E-1	4.86±0.59E 0	1.13±0.18E-1
IC5256	2.85±0.28E-2	2.58±0.26E-2	2.10±0.21E-2	8.08±1.10E-3	5.37±0.74E-3	8.82±1.17E-3	1.75±0.22E-2	1.88±0.20E-2	2.79±0.34E-1	6.06±0.95E-1
UGCA438	2.18±0.22E-2	2.27±0.23E-2	1.68±0.17E-2	9.02±1.22E-3	6.34±0.87E-3	3.85±0.51E-3	4.23±0.53E-3	<4.66E-3	<6.29E-2	<2.38E-1
ESO347-G017	1.86±0.19E-2	2.00±0.20E-2	1.59±0.16E-2	8.80±1.19E-3	5.68±0.78E-3	3.21±0.43E-3	2.94±0.38E-3	8.51±0.95E-3	2.77±0.35E-1	2.91±0.48E-1
UGC12613 ^f	1.22±0.12E-1	9.81±0.98E-2	1.14±0.11E-1	5.55±0.75E-2	3.31±0.46E-2	1.84±0.24E-2	2.63±0.33E-2	2.57±0.28E-2	3.48±0.45E-1	1.21±0.19E-1
IC5332	4.14±0.41E-1	5.73±0.57E-1	3.86±0.39E-1	2.38±0.32E-1	1.64±0.23E-1	1.85±0.23E-1	2.93±0.37E-1	3.34±0.36E-1	4.61±0.56E 0	1.98±0.31E-1
NGC7713	1.79±0.18E-1	2.24±0.22E-1	1.51±0.15E-1	1.00±0.14E-1	6.85±0.94E-2	8.53±1.09E-2	1.40±0.17E-1	2.84±0.31E-1	5.69±0.69E 0	1.09±0.17E-1
UGCA442	2.32±0.23E-2	2.37±0.24E-2	1.34±0.13E-2	1.12±0.15E-2	7.51±1.03E-3	3.81±0.51E-3	2.63±0.34E-3	1.01±0.11E-2	1.20±0.16E-1	2.63±0.44E-1
kkh098	1.02±0.10E-2	1.07±0.11E-2	7.56±0.76E-3	2.42±0.33E-3	1.56±0.22E-3	<1.46E-3	<1.60E-3	<2.65E-3	<3.56E-2	<1.34E-1
ESO149-G003	1.03±0.10E-2	1.27±0.13E-2	<1.01E-1	3.55±0.48E-3	2.59±0.36E-3	6.90±1.00E-4	8.40±1.10E-4	8.90±1.60E-4	5.59±0.82E-2	<2.14E-1
NGC7793 ^{e f}	1.68±0.17E 0	1.70±0.17E 0	1.31±0.13E 0	7.71±1.04E-1	4.69±0.64E-1	1.02±0.13E 0	1.85±0.23E 0	2.03±0.08E 0	3.33±0.24E 1	1.17±0.15E-1

Note. — See § 4 for corrections that have been applied to the data. The uncertainties include both statistical and systematic effects ($\lesssim 10\%$ for the near-infrared data).

^aInfrared photometry for the Large and Small Magellanic Clouds are from Bernard et al. (2008) and Leroy et al. (2007), respectively.

^bNGC 1800 and MCG-05-13-004 spatially overlap so separate photometry for MCG-05-13-004 is not provided.

^cThe bright core of NGC 3034 (M 82) has rendered the *Spitzer* data extremely difficult to process; saturation effects severely limit our ability to extract reliable flux densities.

^dOnly 4.5 and 8.0 μm data were obtained for IC 5152.

^eIRAC imaging taken from the archives.

^fMIPS imaging taken from the archives.

Table 3. IRAC Aperture Correction Parameters

λ	A	B	C
3.5 μm	0.82	0.370	0.910
4.5 μm	1.16	0.443	0.940
5.8 μm	1.49	0.207	0.710
8.0 μm	1.37	0.330	0.740

Note. — See § 4 and
<http://ssc.spitzer.caltech.edu/irac/calib/extcal/>

Table 4. LVL Infrared Ratios and Dispersions

Ratio	Median	Dispersion (dex)
$f_\nu(70\mu\text{m})/f_\nu(160\mu\text{m})$	0.84	0.22
$f_\nu(8.0\mu\text{m})/f_\nu(24\mu\text{m})$	0.41	0.27
$\nu f_\nu(8.0\mu\text{m})/TIR$	0.098	0.23
$\nu f_\nu(8.0\mu\text{m})_{\text{dust}}/TIR$	0.19	0.44
$\nu f_\nu(24\mu\text{m})/TIR$	0.080	0.15
$\nu f_\nu(70\mu\text{m})/TIR$	0.60	0.11
$\nu f_\nu(160\mu\text{m})/TIR$	0.31	0.12

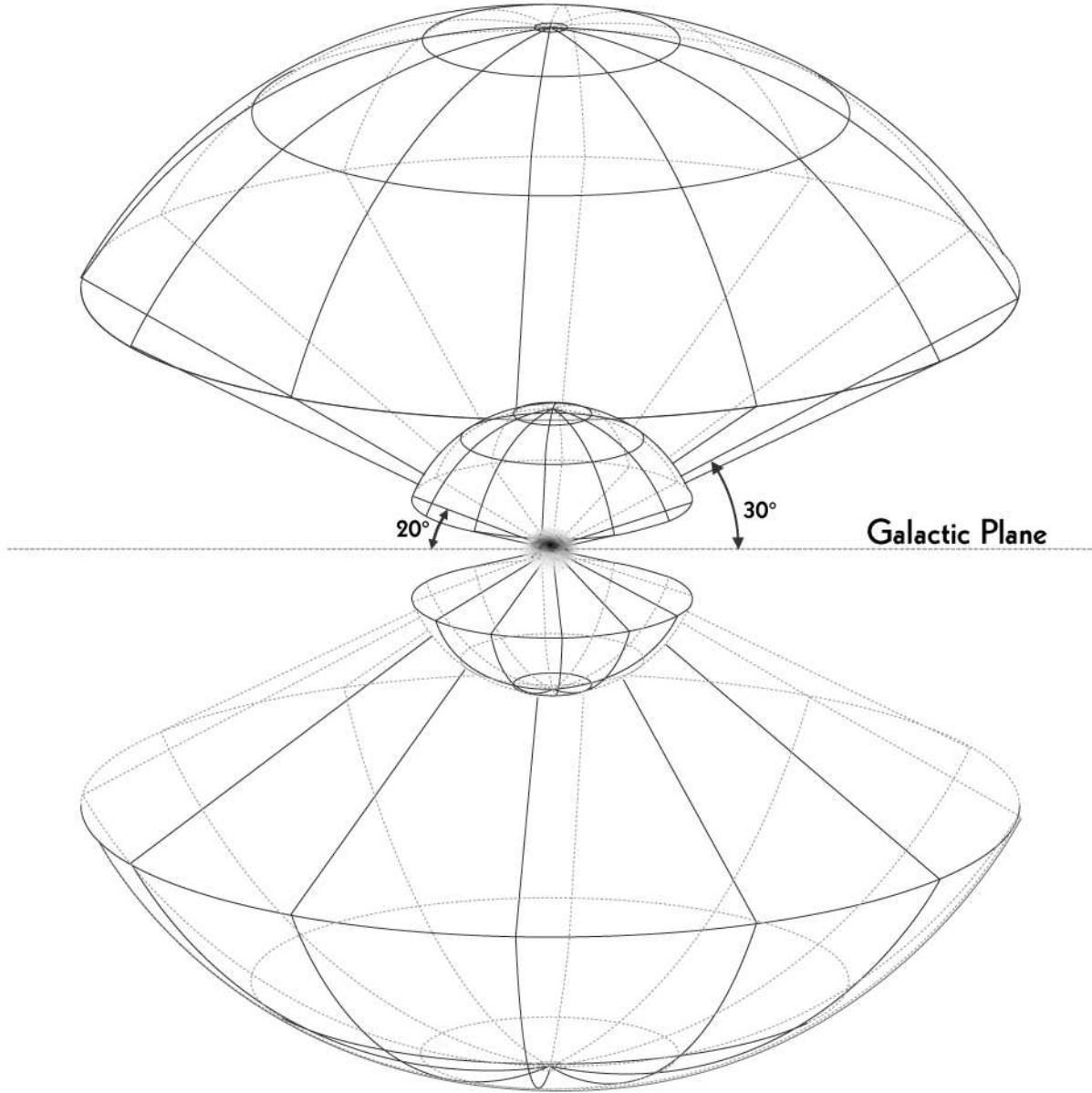


Fig. 1.— Schematic representation of the tiered volume coverage for the Local Volume Legacy survey. The 258 galaxies in the LVL sample include *i*) 69 early- and late-type galaxies primarily within the inner volume for which *HST* observations exist from the ANGST program, and *ii*) a magnitude-limited sample of spiral and irregular galaxies from 11HUGS out to 11 Mpc. The *Spitzer* infrared imaging data that are being collected by LVL complement the ground-based $H\alpha$ and *GALEX* ultraviolet imaging already available for the sample. Image credit: Pete Marenfeld (NOAO/AURA/NSF).

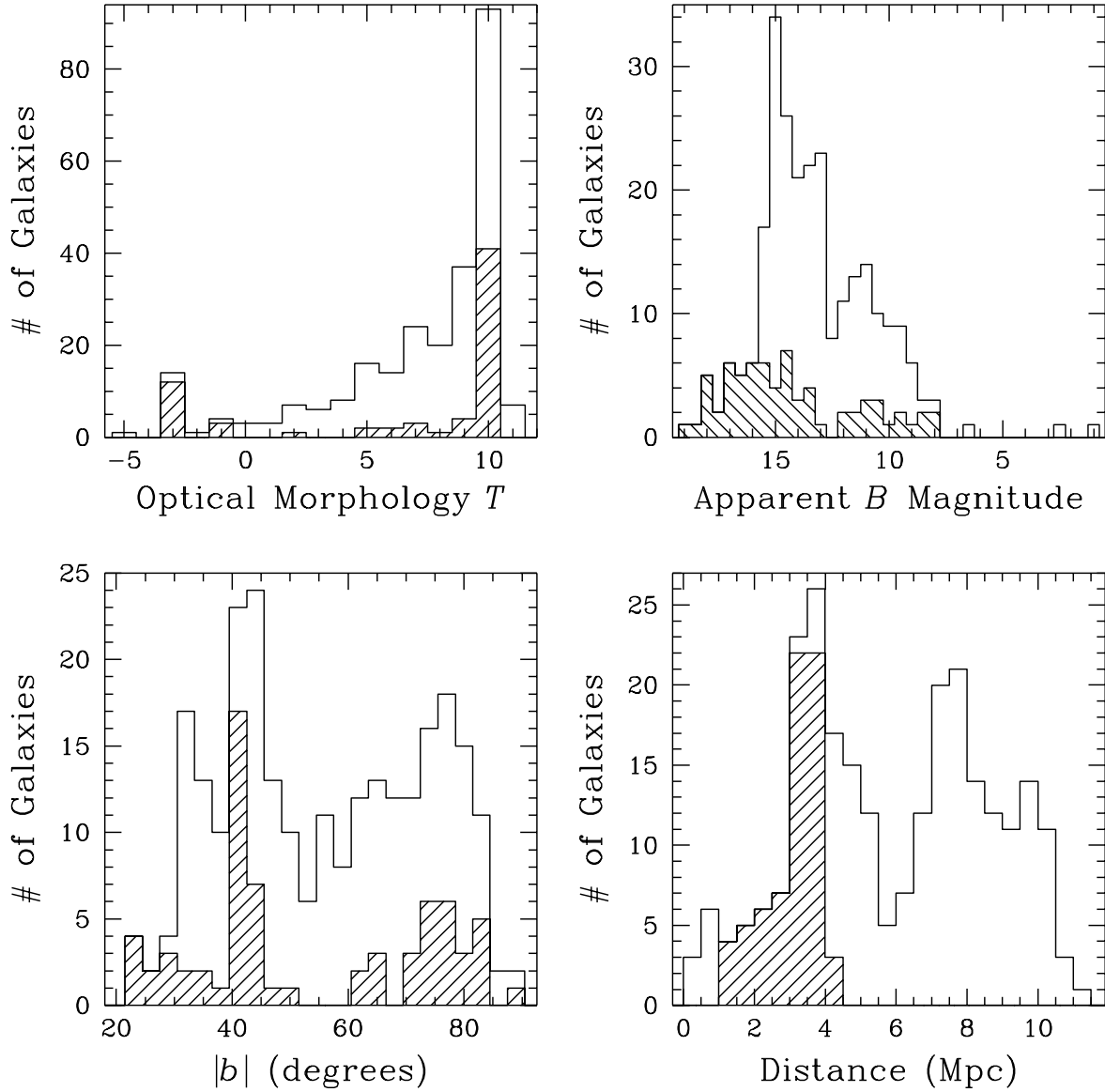


Fig. 2.— The distributions of RC3 morphological type (top left), apparent B magnitude (top right), Galactic latitude (bottom left) and distance (bottom right) for the LVL sample. The histograms outlined by the solid lines show the entire sample of 258 galaxies, whereas the shaded portions indicate the ANGST sub-sample for which *HST* resolved stellar populations observations are available.

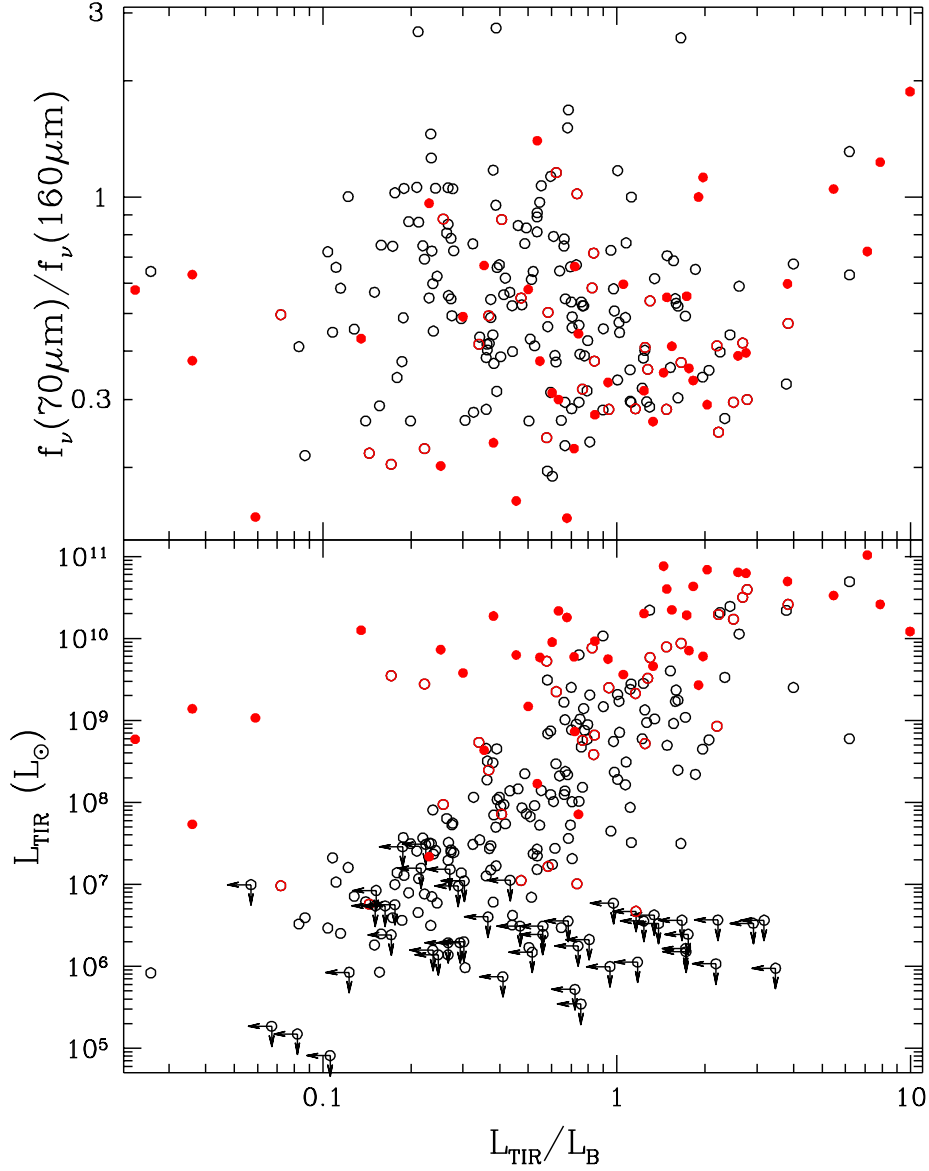


Fig. 3.— The range of total infrared and total infrared-to-optical properties in the LVL (open black circles) and SINGS (filled red circles) samples. Open red circles denote galaxies in both samples. SINGS data are taken from Dale et al. (2007).

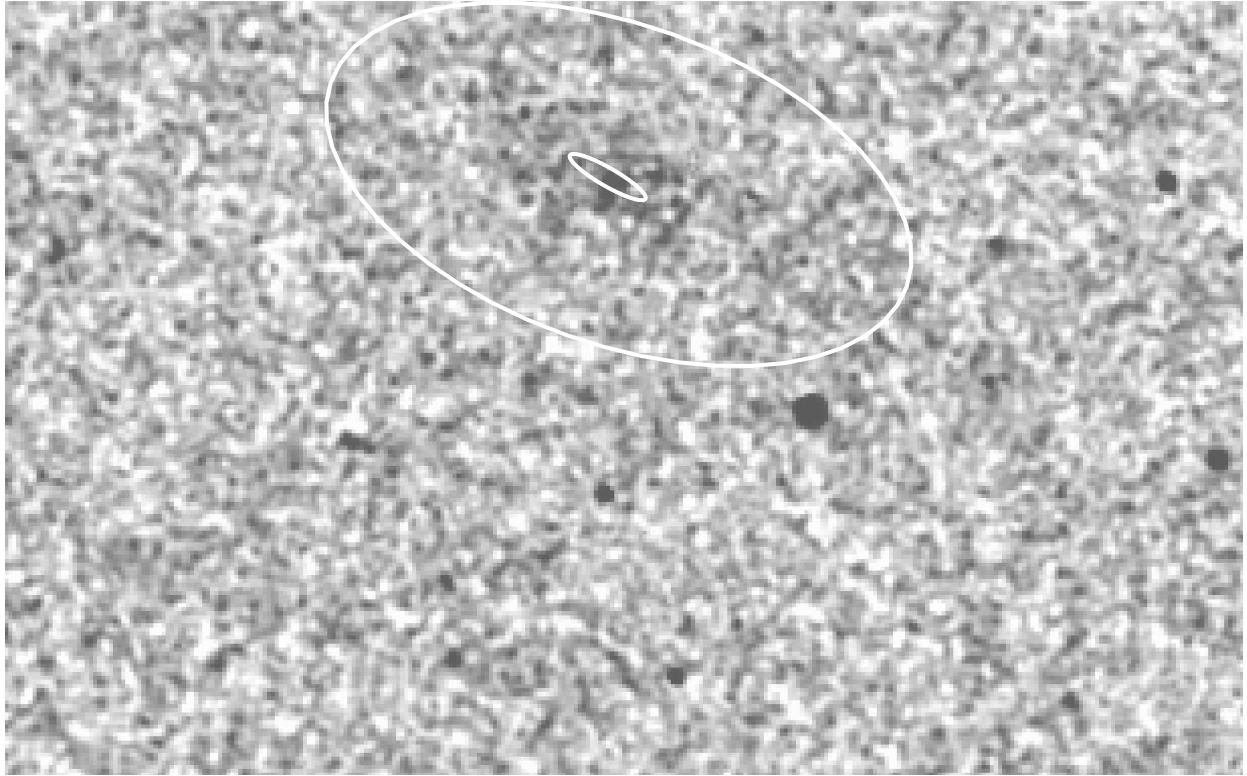


Fig. 4.— A comparison of extraction apertures for UGC 08245 from our work (large ellipse) and from the 2MASS Extended Source Catalog (small ellipse). The larger aperture captures more of the faint diffuse emission from the galaxy’s disk.

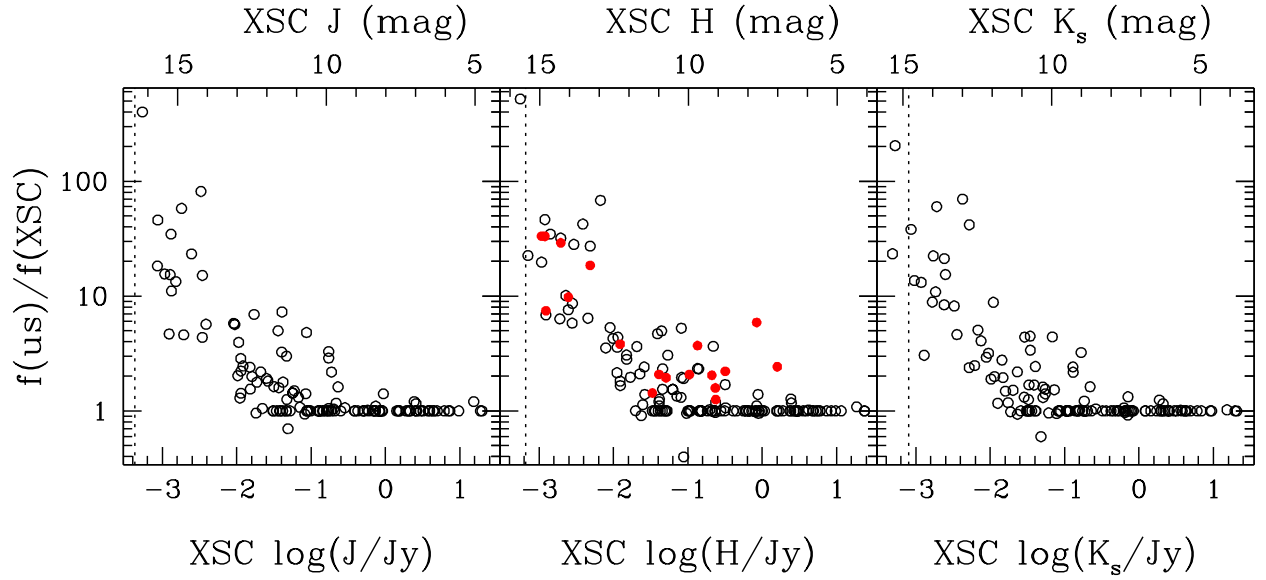


Fig. 5.— A comparison of near-infrared fluxes extracted from the 2MASS image archives using the apertures described in § 4.2 with those from the 2MASS Extended Source Catalog. The filled red circles are based on deep H band imaging of nearby galaxies with the 3.9 m Anglo-Australian Telescope (Kirby et al. 2008). The vertical dotted lines indicate the 2MASS 10σ point source detection limits.

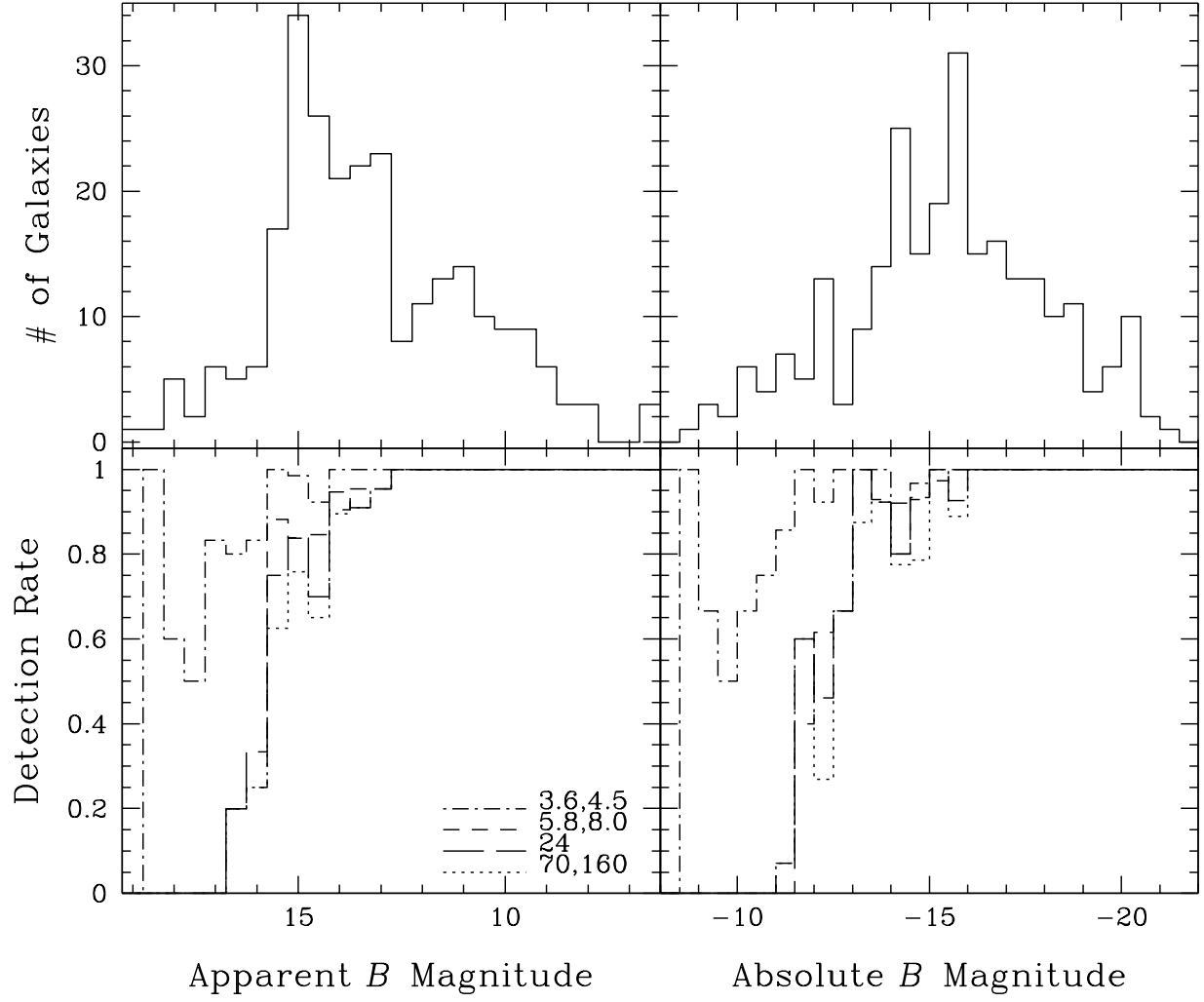


Fig. 6.— Top: The distribution of LVL galaxies as a function of apparent and absolute B -band magnitudes. Bottom: The imaging detection rates for different *Spitzer* wavelengths.

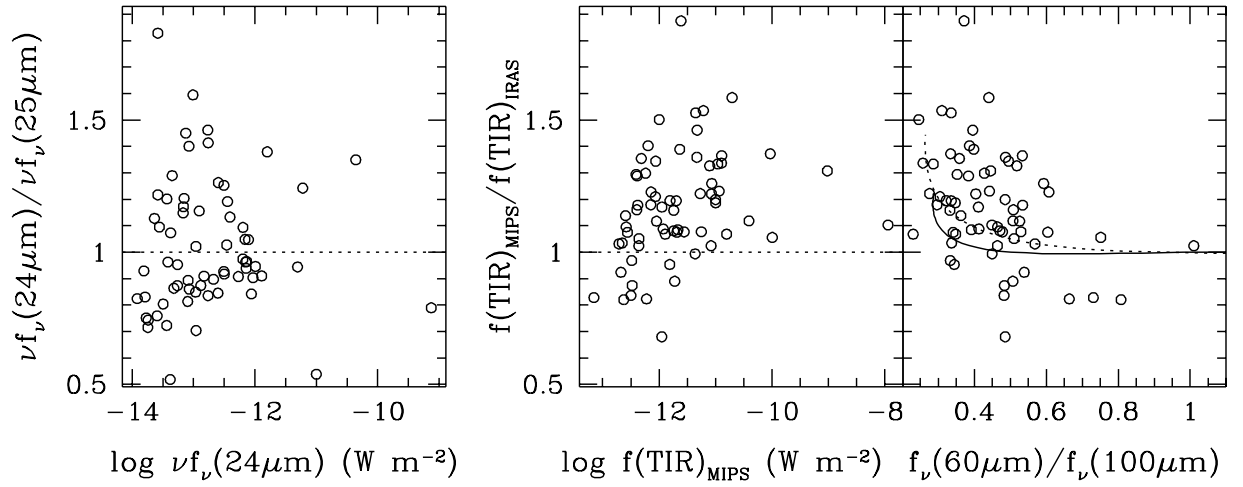


Fig. 7.— A comparison of *Spitzer* and *IRAS* data for the LVL sample. The left-most panel shows the ratio of *Spitzer* 24 μm and *IRAS* 25 μm data, and the right two panels compare the total infrared as measured from *Spitzer* and *IRAS*. The dotted line in the left two panels indicate a ratio of unity, whereas the solid and dotted line in the right-most panel indicate SED model predictions from Dale & Helou (2002) and Dale et al. (2001), respectively.

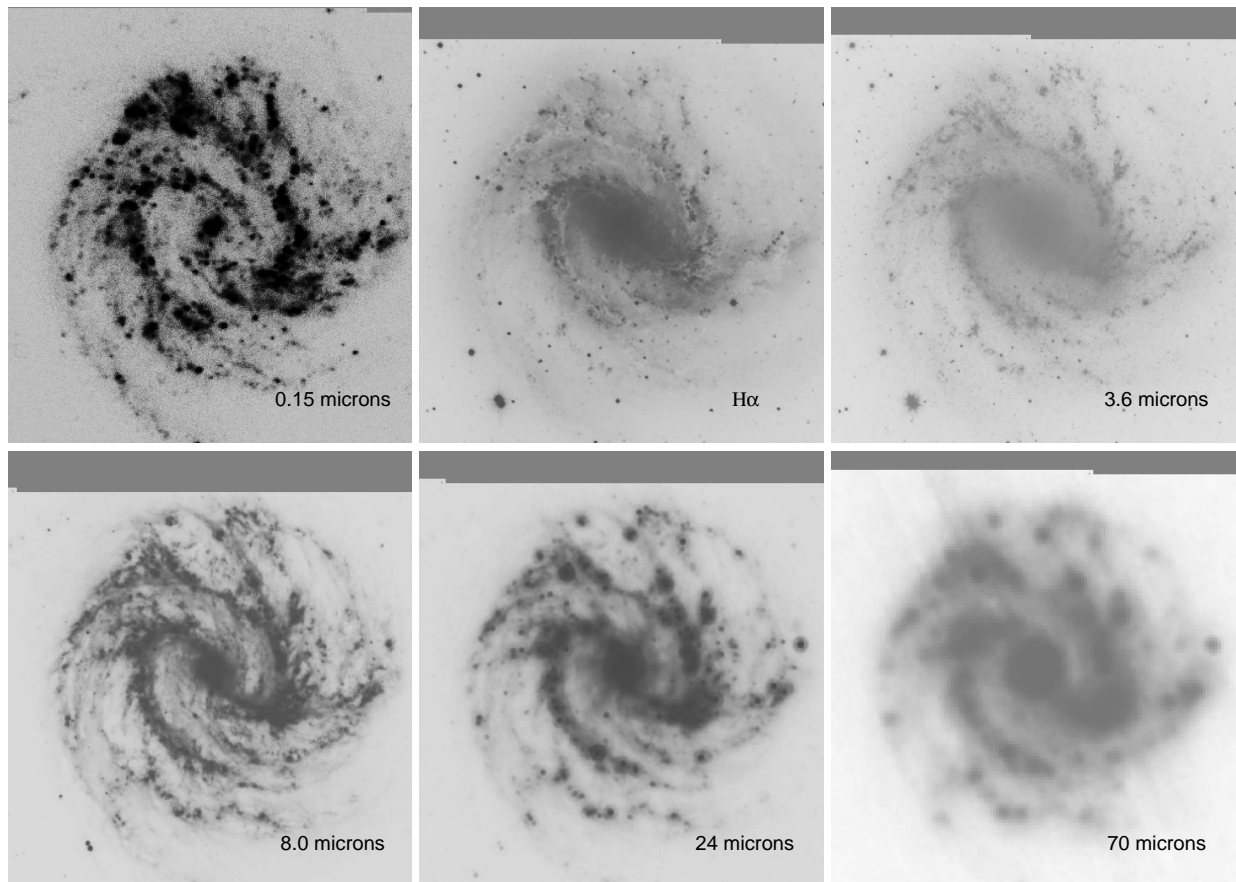


Fig. 8.— A multi-wavelength mosaic of spiral galaxy NGC 5236, displaying the range of imaging available for the LVL survey.

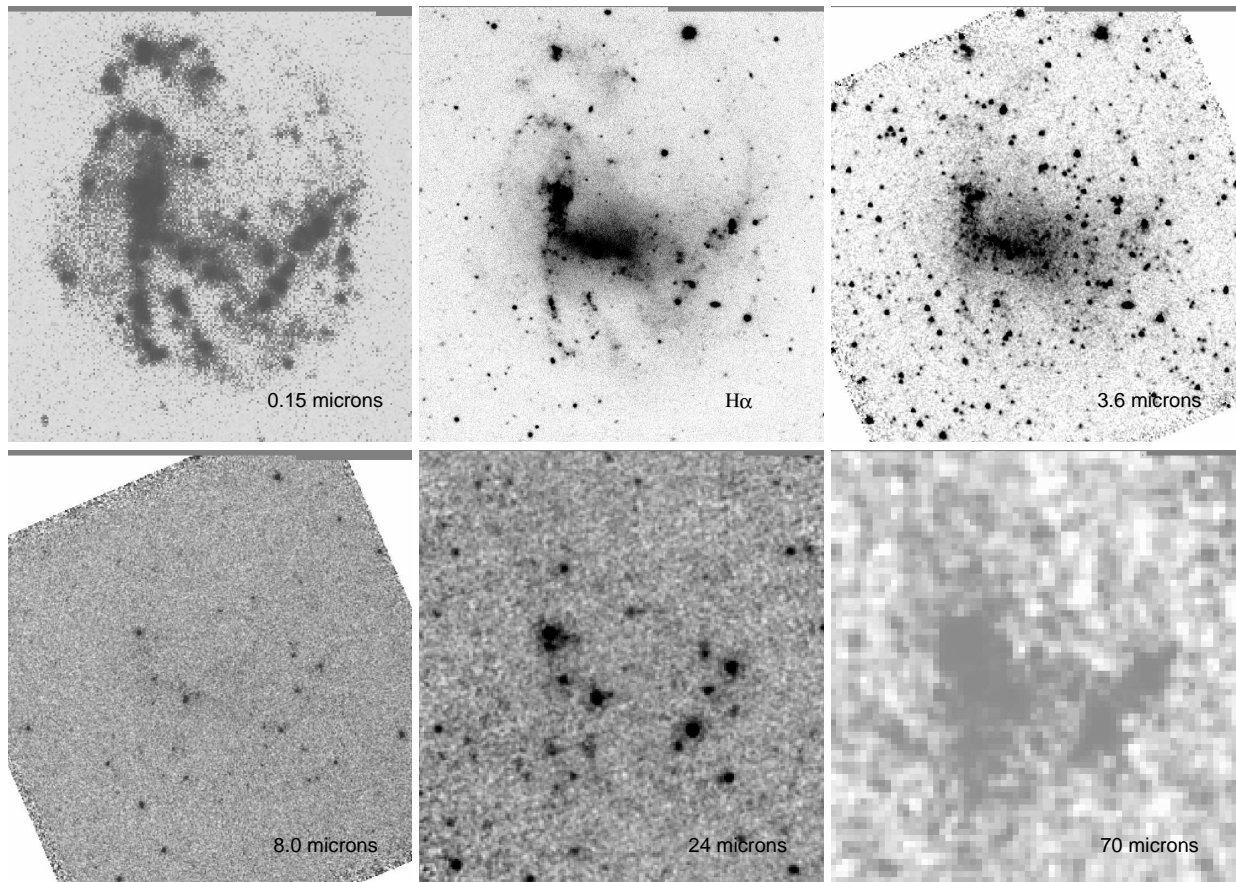


Fig. 9.— The same as Figure 8 but for the irregular galaxy UGC 05829.

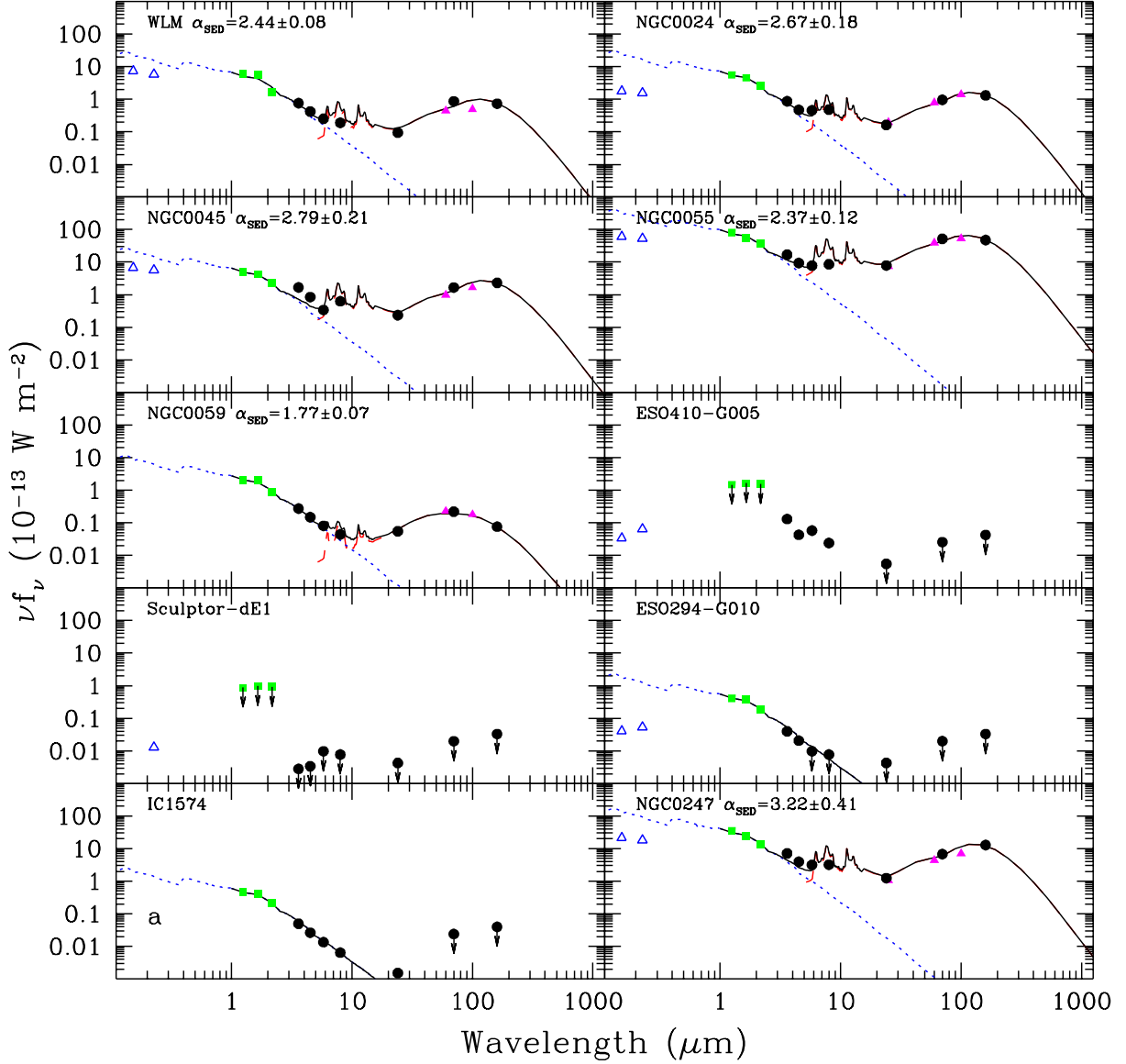


Fig. 10.— Globally-integrated 0.15-160 μm spectral energy distributions for the LVL sample. *GALEX* (Gil de Paz et al. 2009), 2MASS, *IRAS*, and *Spitzer* data are represented by open triangles, filled squares, filled triangles, and filled circles, respectively. Downward-pointing arrows, if present, indicate 3σ upper limits. The solid curve is the sum of a dust (dashed) and a stellar (dotted) model. The dust curve is a Dale & Helou (2002) model fitted to the amplitude and ratios of the observed 24, 70, and 160 μm fluxes; the α_{SED} listed within each panel parameterizes the distribution of dust mass as a function of heating intensity, as described in Dale & Helou (2002). The stellar curve, serving merely as a fiducial visual aid, is a 1 Gyr continuous star formation, solar metallicity curve from Vazquez & Leitherer (2005) fitted to the 2MASS data (see § 5.3 for details).

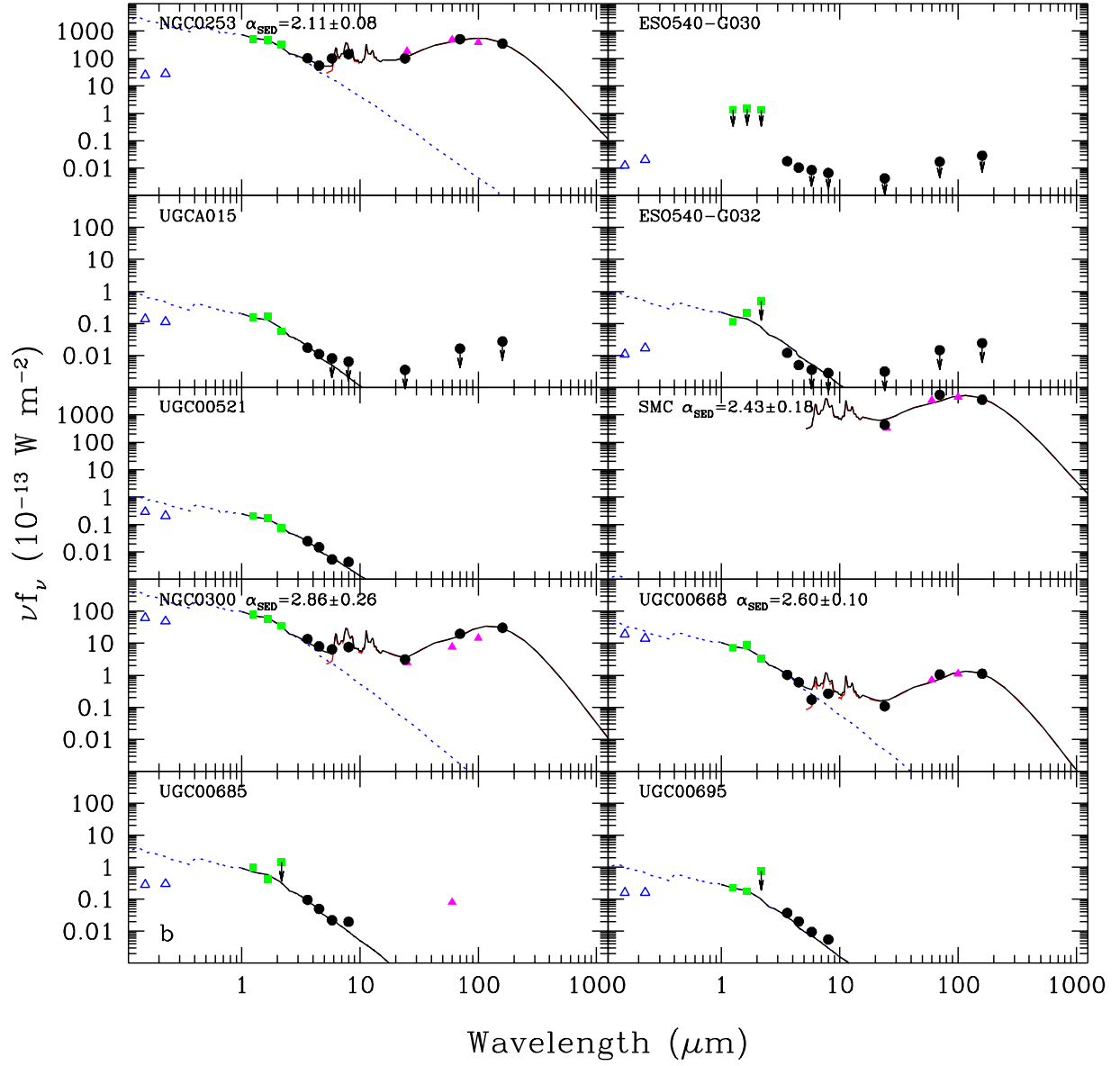


Fig. 10.— Globally-integrated 0.15-160 μm spectral energy distributions for the LVL sample (continued).

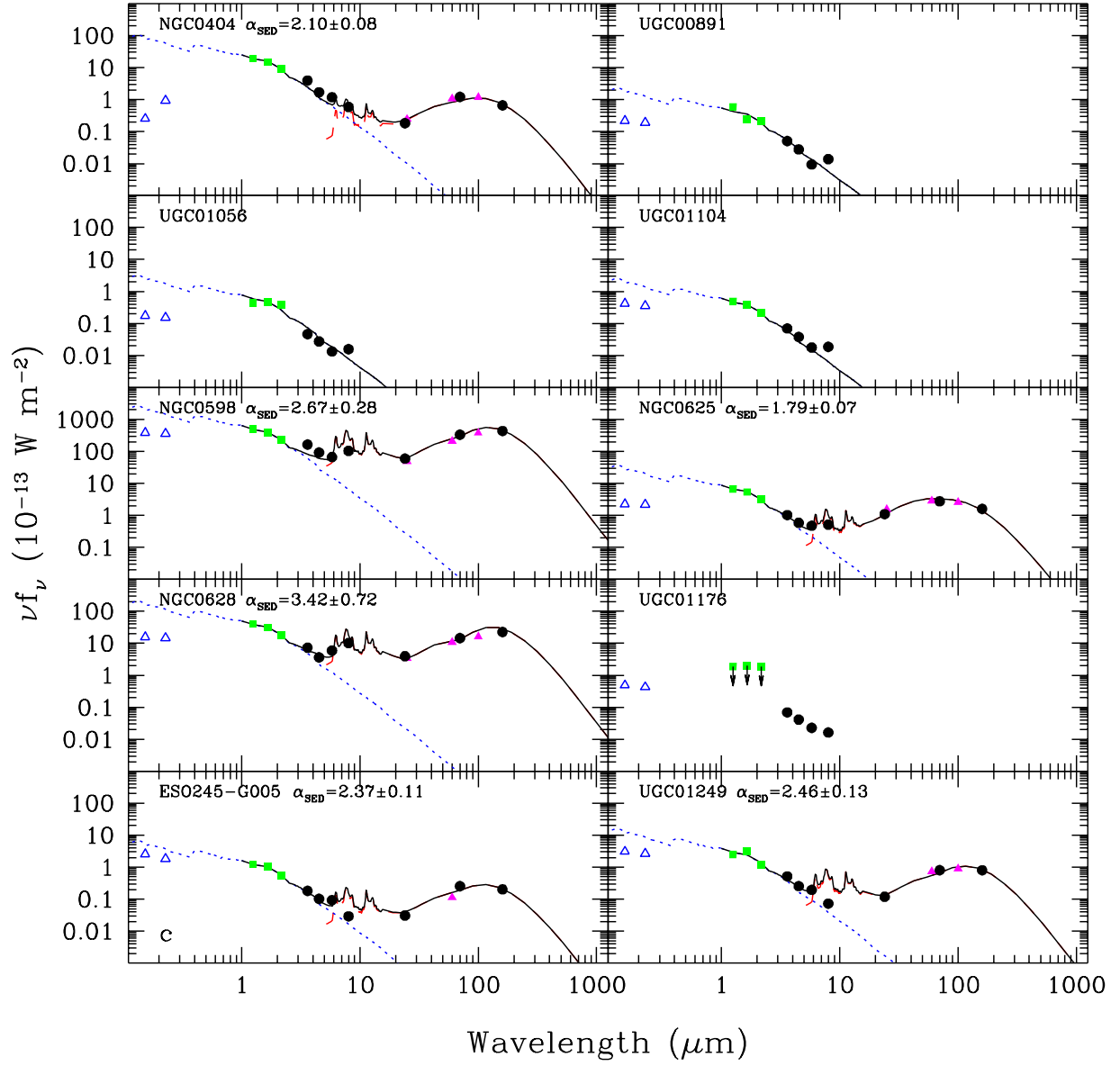


Fig. 10.— Globally-integrated 0.15-160 μm spectral energy distributions for the LVL sample (continued).

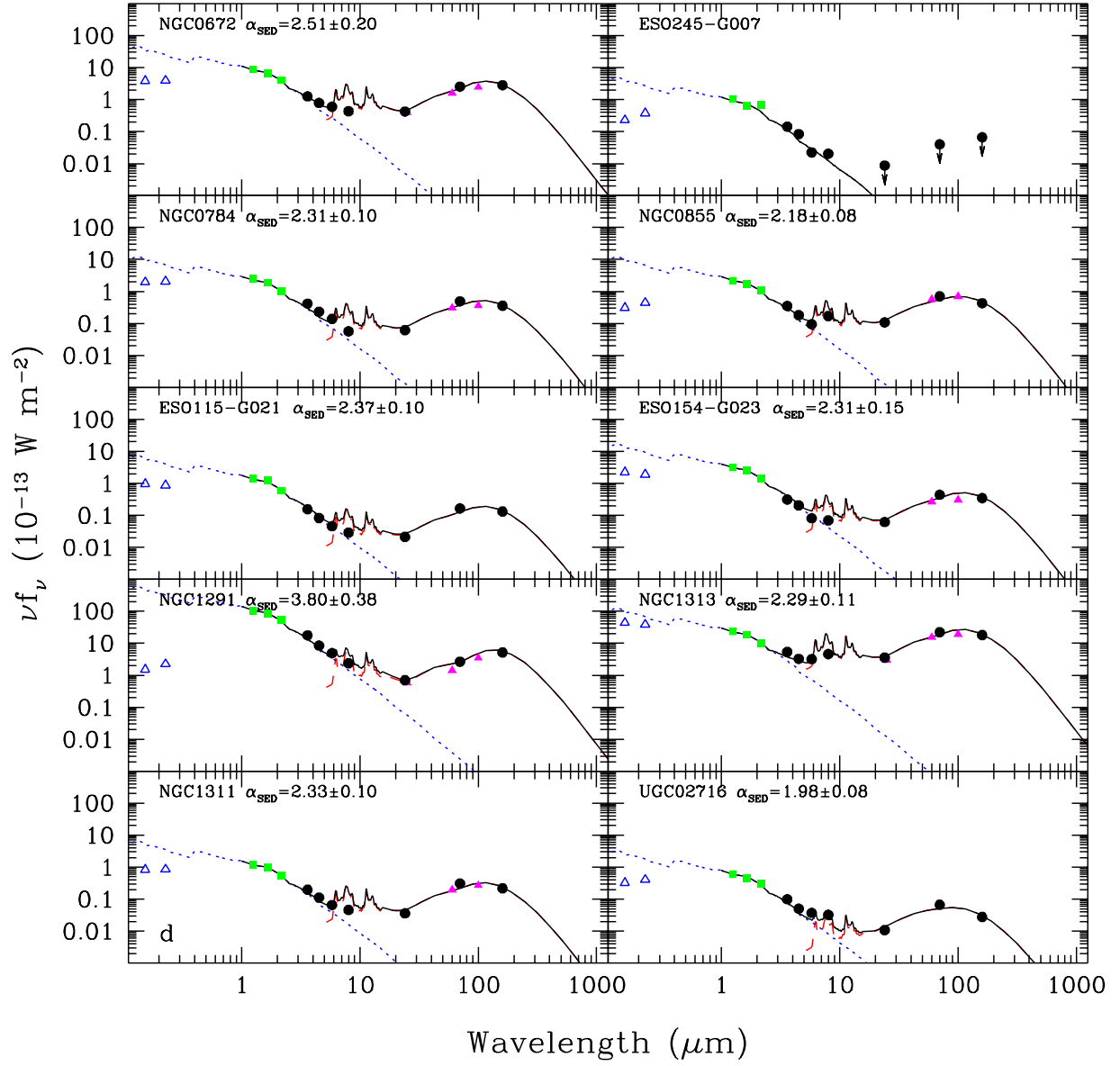


Fig. 10.— Globally-integrated 0.15-160 μm spectral energy distributions for the LVL sample (continued).

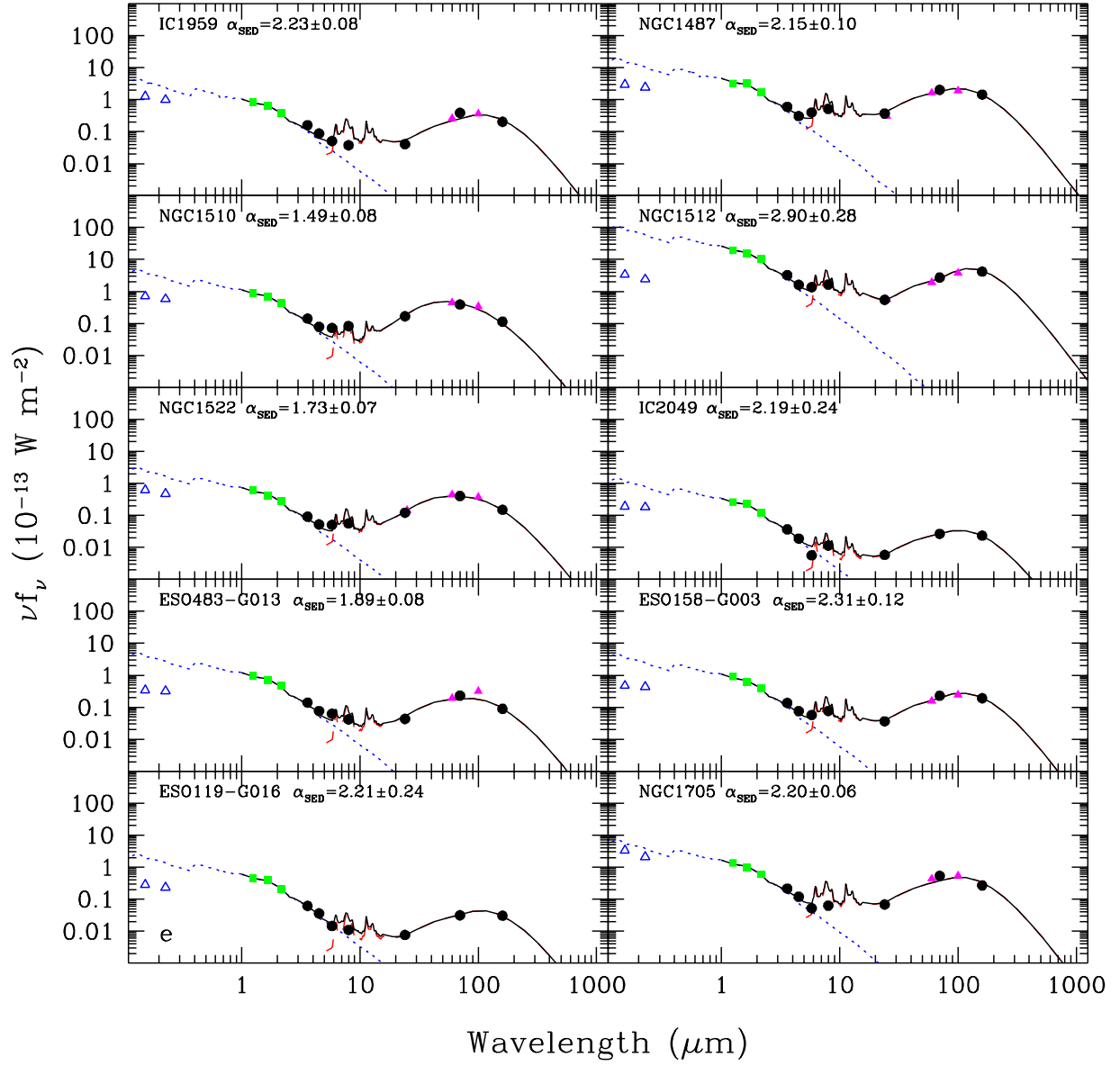


Fig. 10.— Globally-integrated 0.15-160 μm spectral energy distributions for the LVL sample (continued).

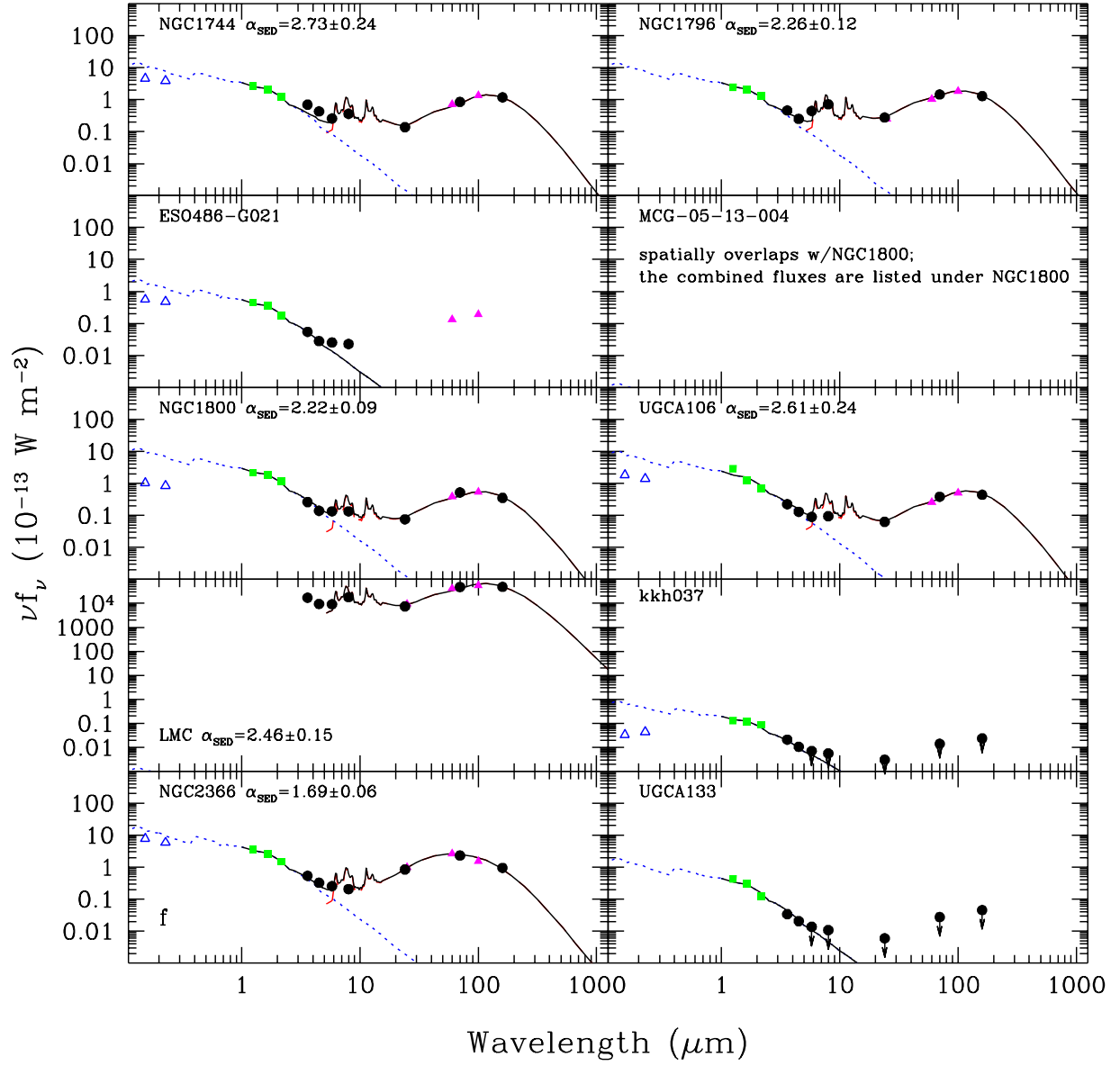


Fig. 10.— Globally-integrated 0.15-160 μm spectral energy distributions for the LVL sample (continued).

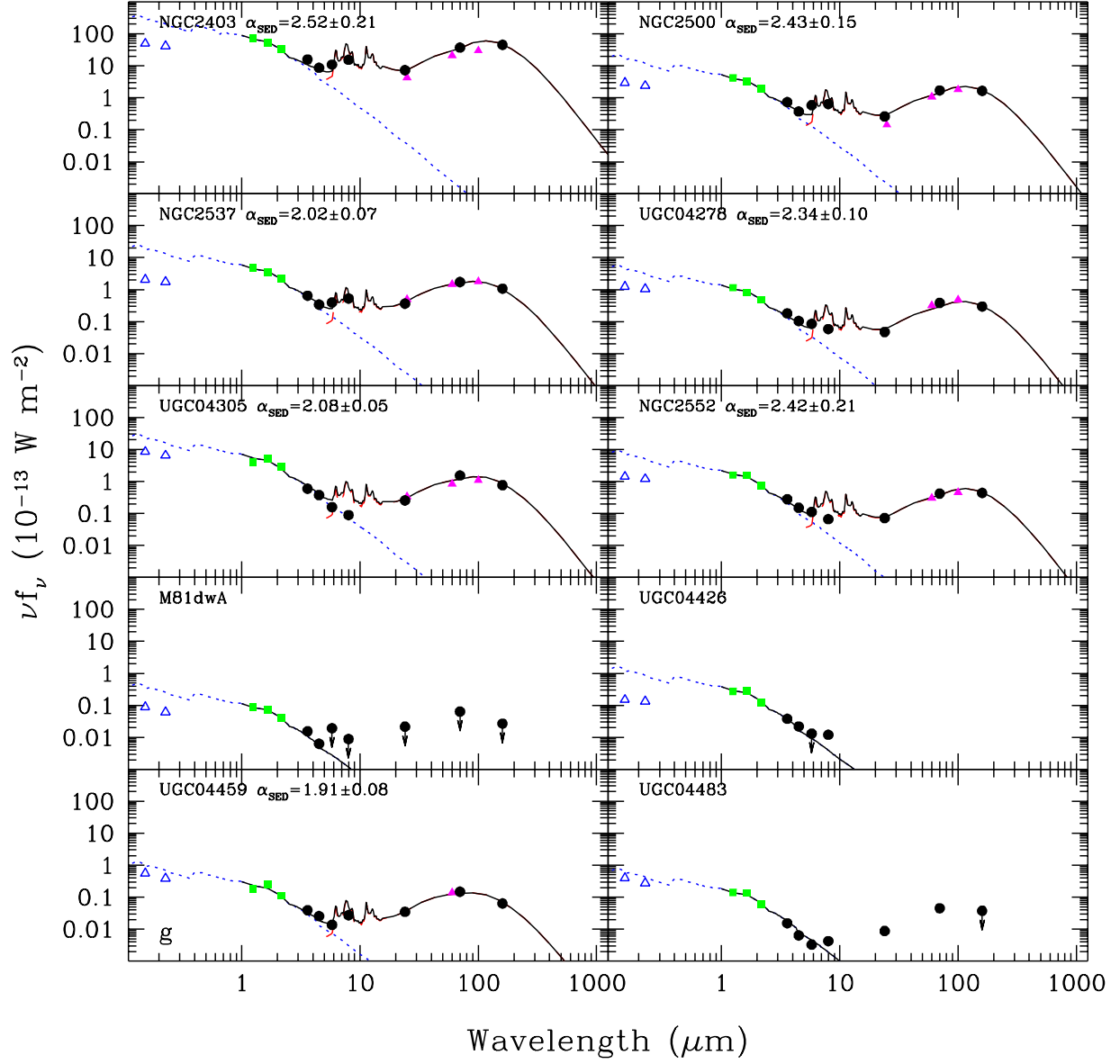


Fig. 10.— Globally-integrated 0.15-160 μm spectral energy distributions for the LVL sample (continued).

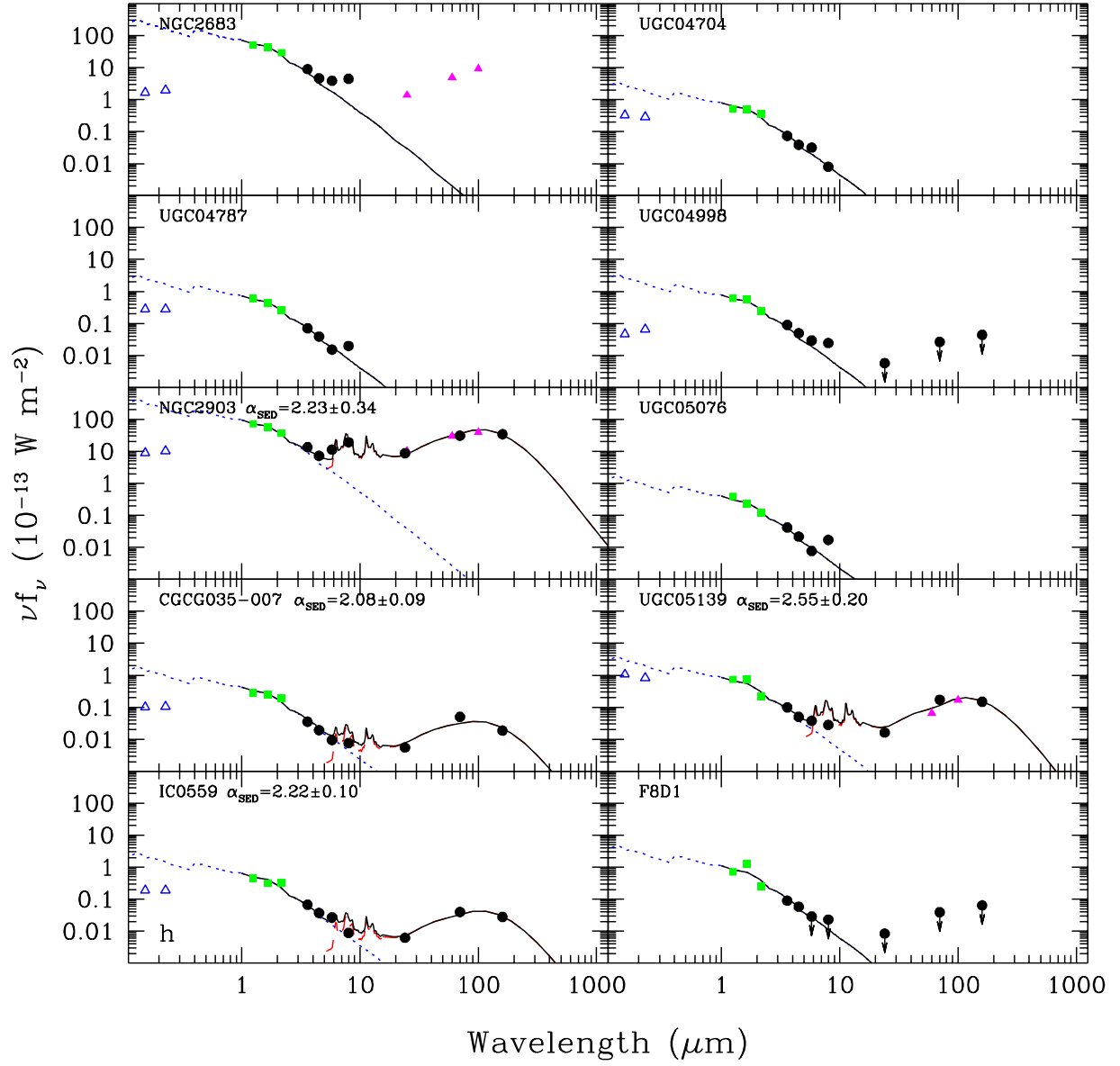


Fig. 10.— Globally-integrated 0.15-160 μm spectral energy distributions for the LVL sample (continued).

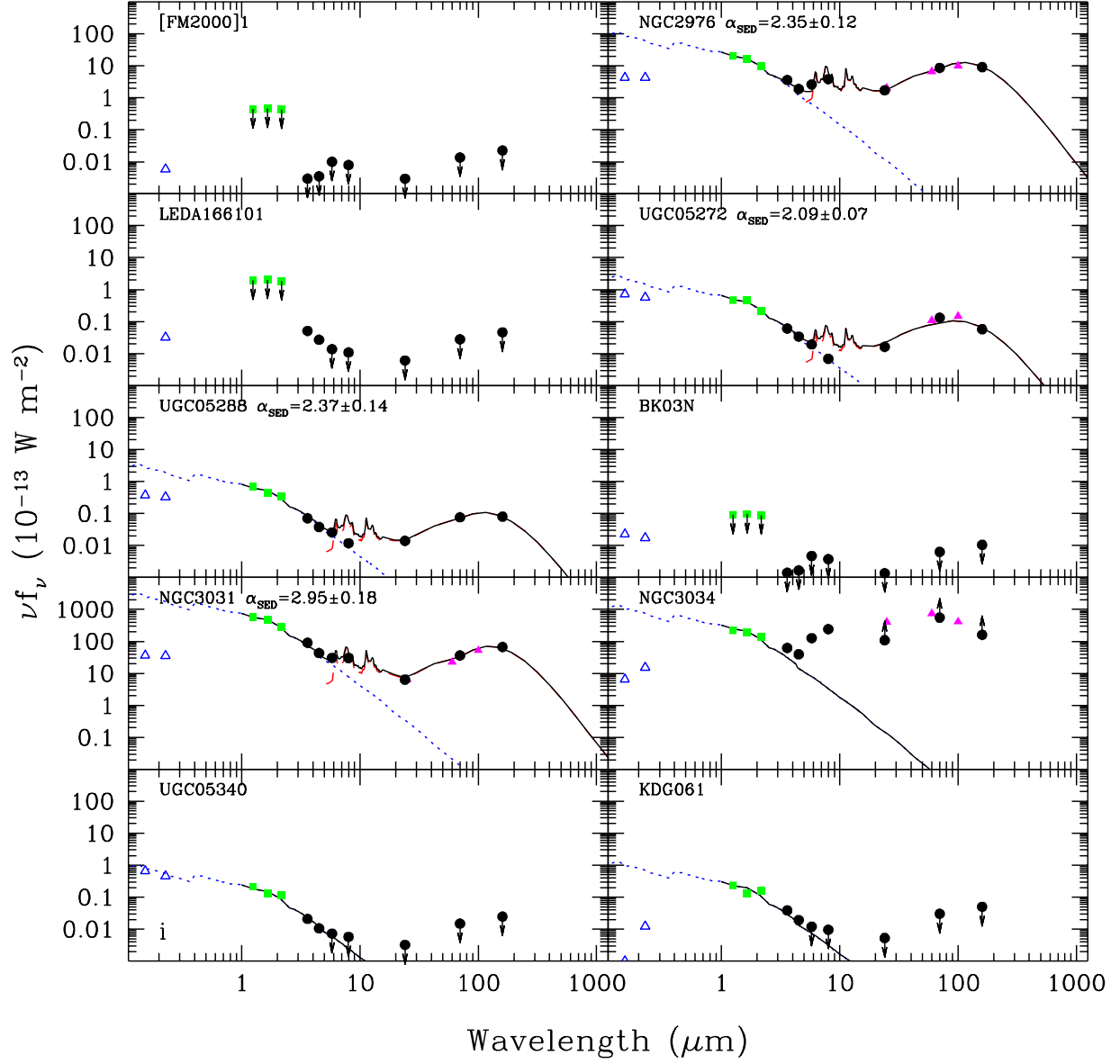


Fig. 10.— Globally-integrated 0.15-160 μm spectral energy distributions for the LVL sample (continued).

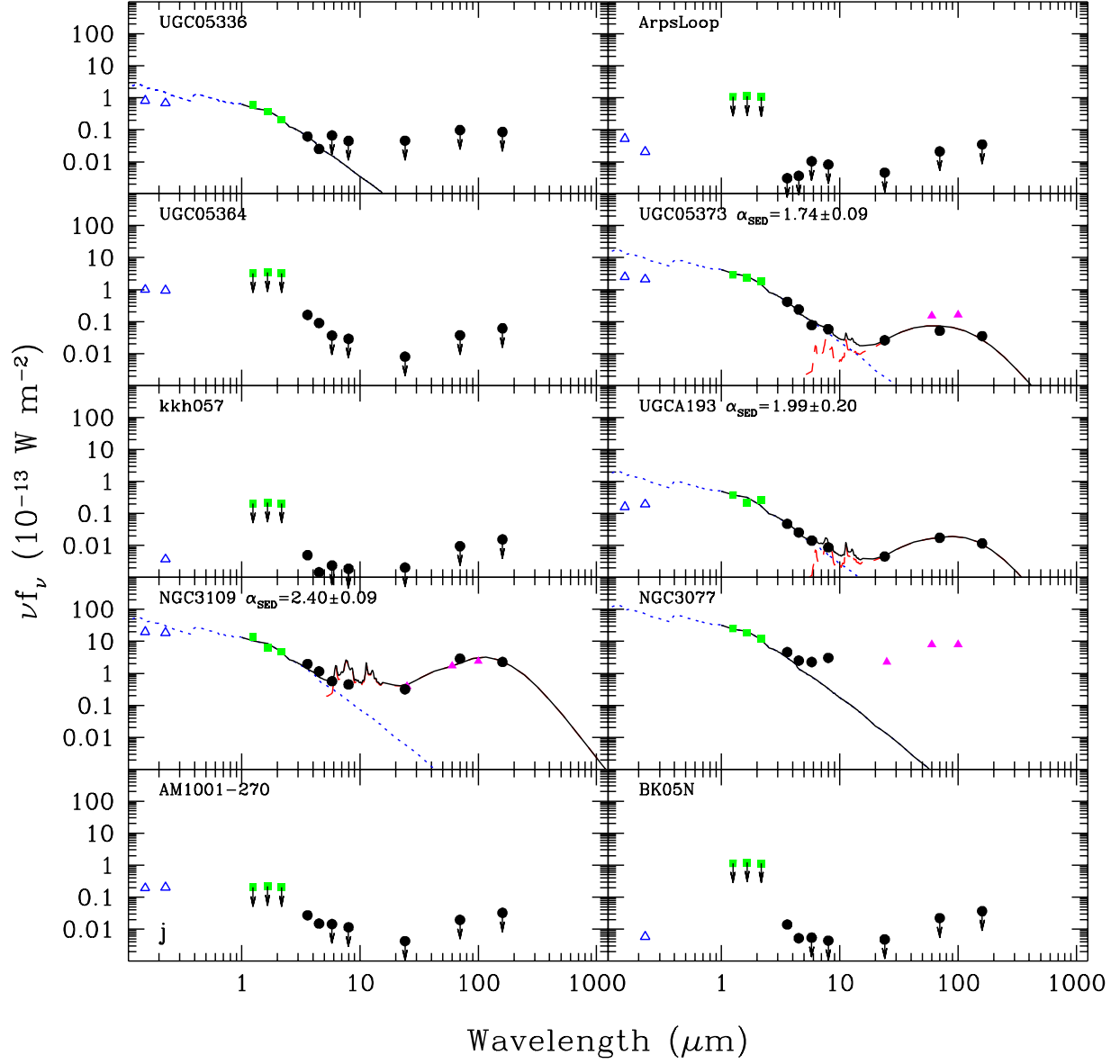


Fig. 10.— Globally-integrated 0.15-160 μm spectral energy distributions for the LVL sample (continued).

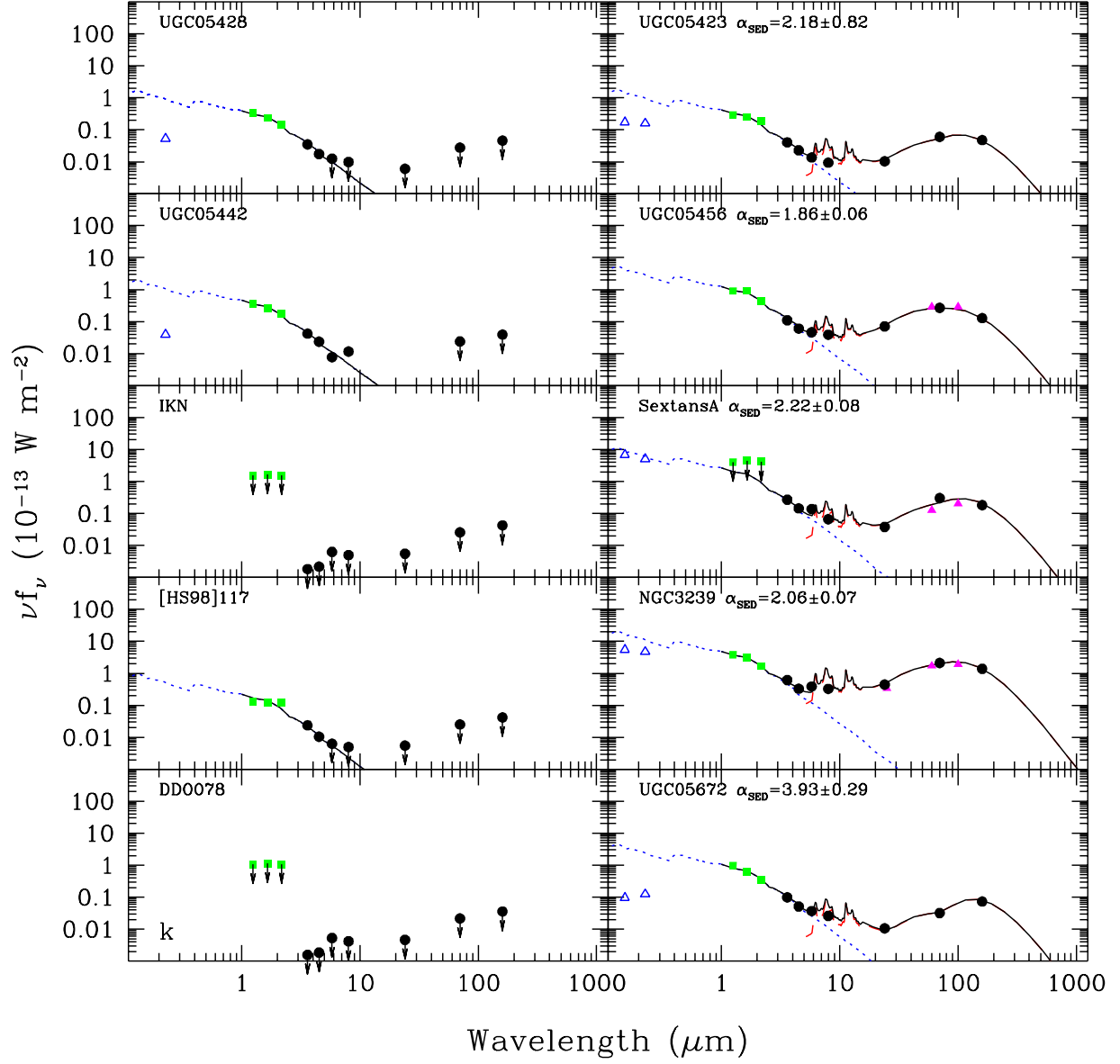


Fig. 10.— Globally-integrated 0.15-160 μm spectral energy distributions for the LVL sample (continued).

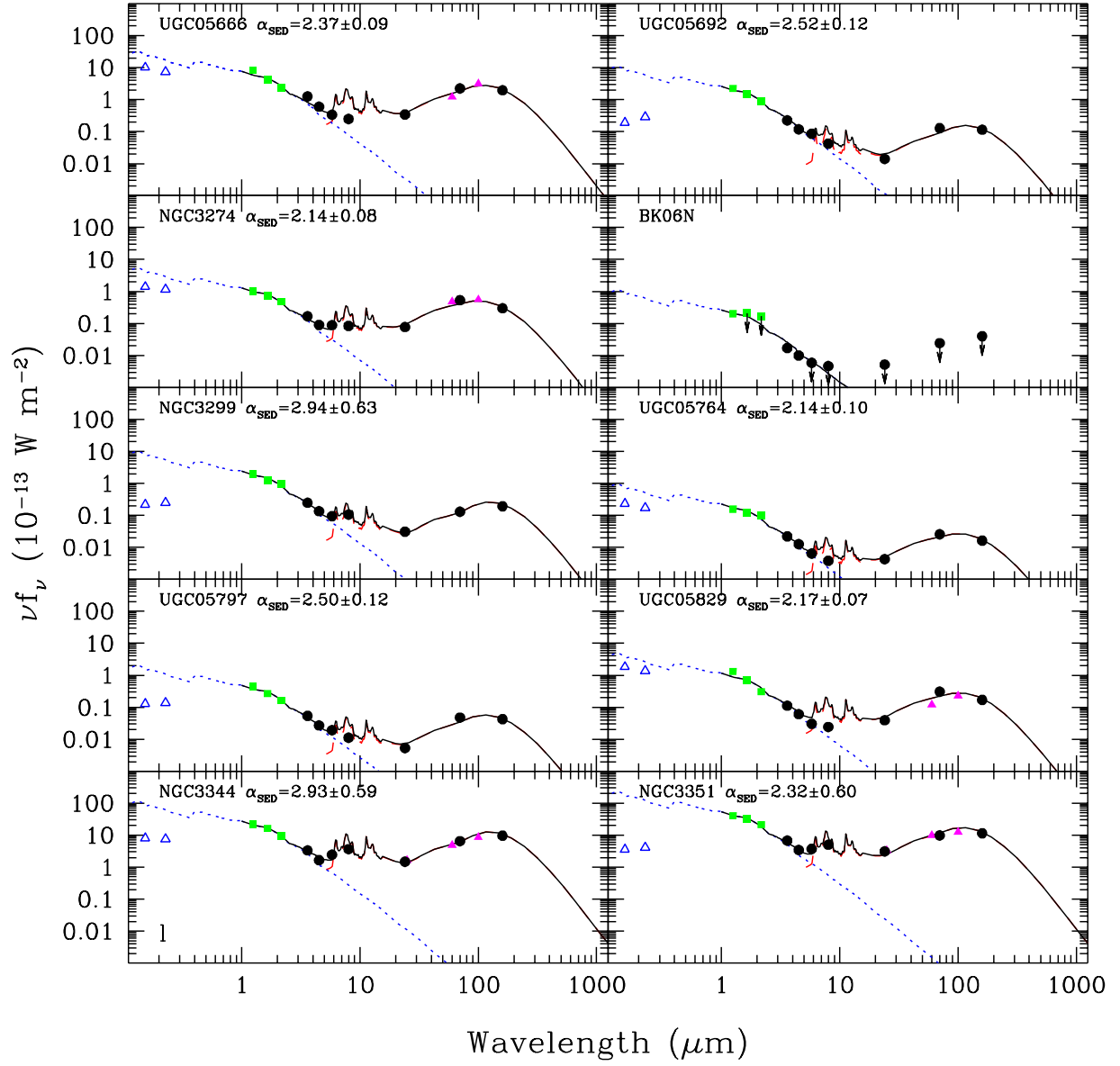


Fig. 10.— Globally-integrated 0.15–160 μm spectral energy distributions for the LVL sample (continued).

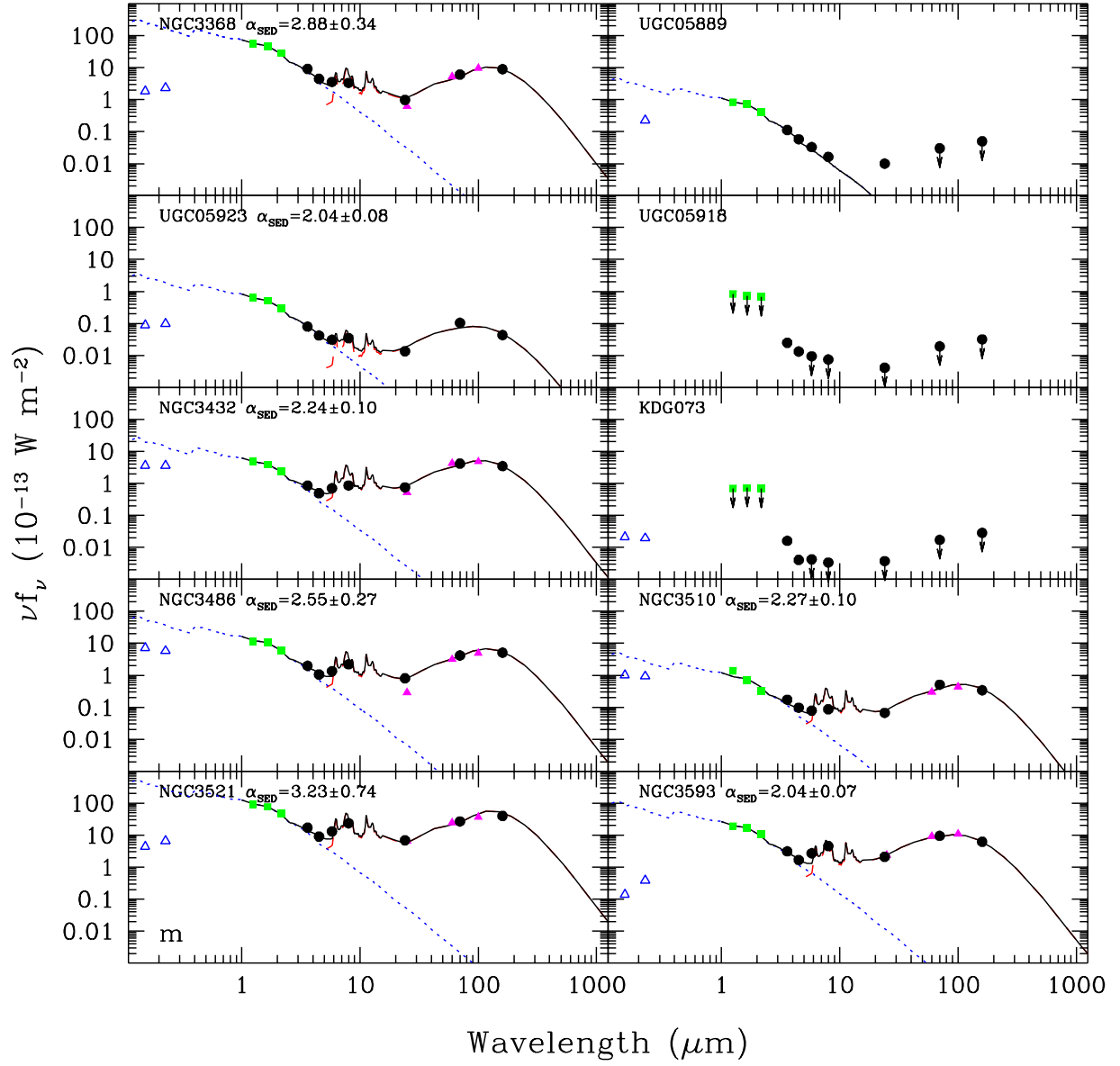


Fig. 10.— Globally-integrated 0.15-160 μm spectral energy distributions for the LVL sample (continued).

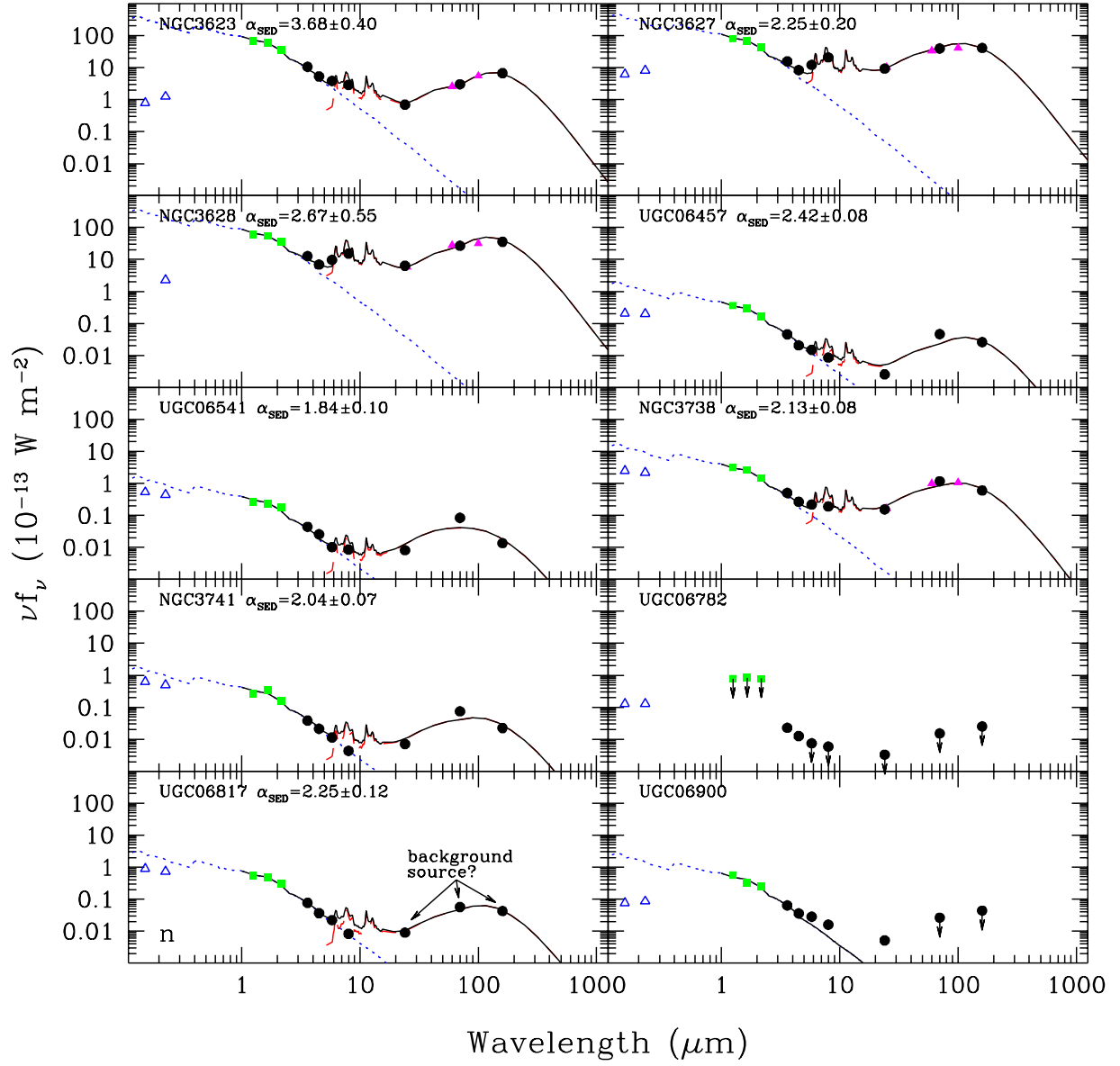


Fig. 10.— Globally-integrated 0.15-160 μm spectral energy distributions for the LVL sample (continued).

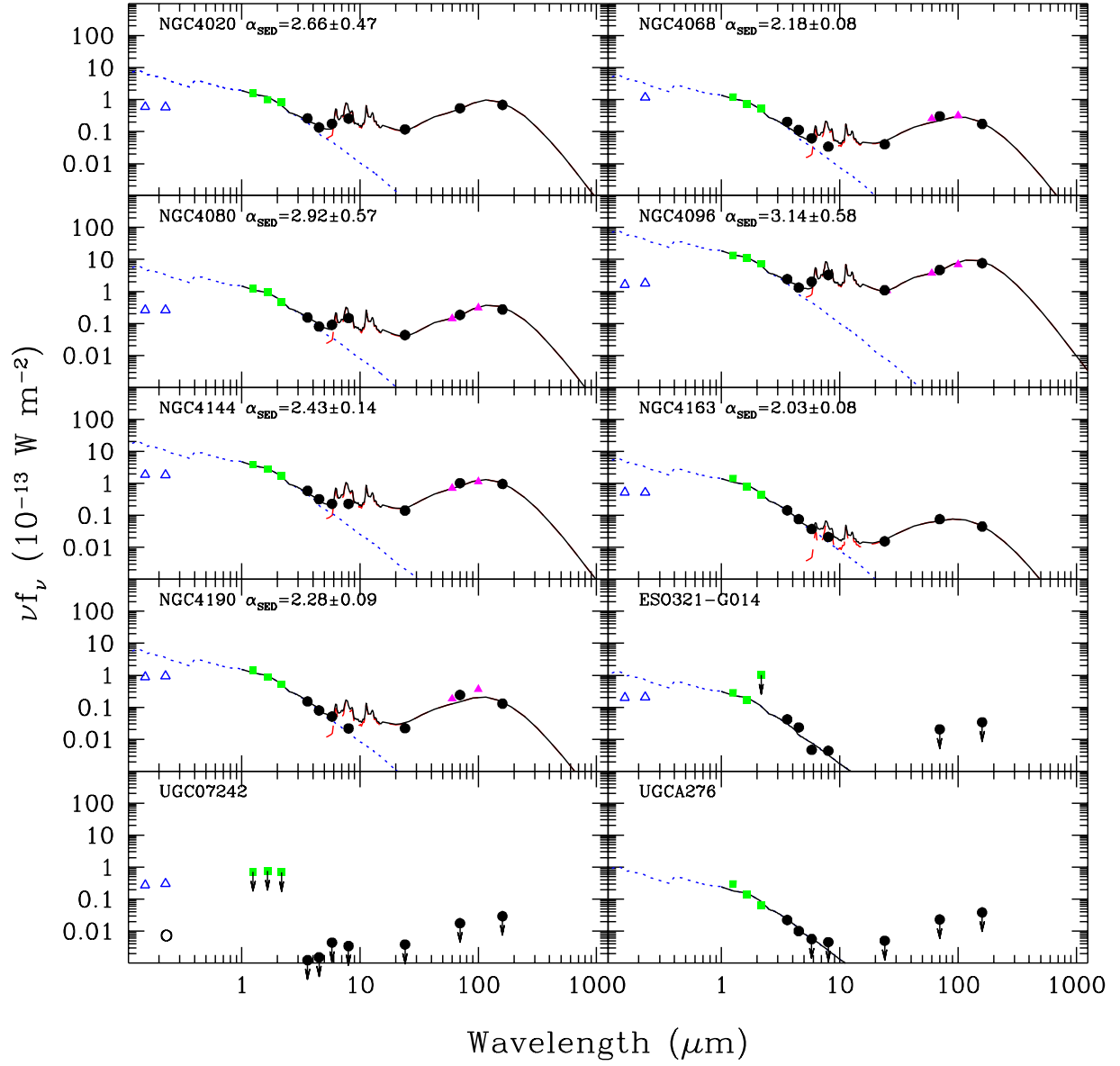


Fig. 10.— Globally-integrated 0.15-160 μm spectral energy distributions for the LVL sample (continued).

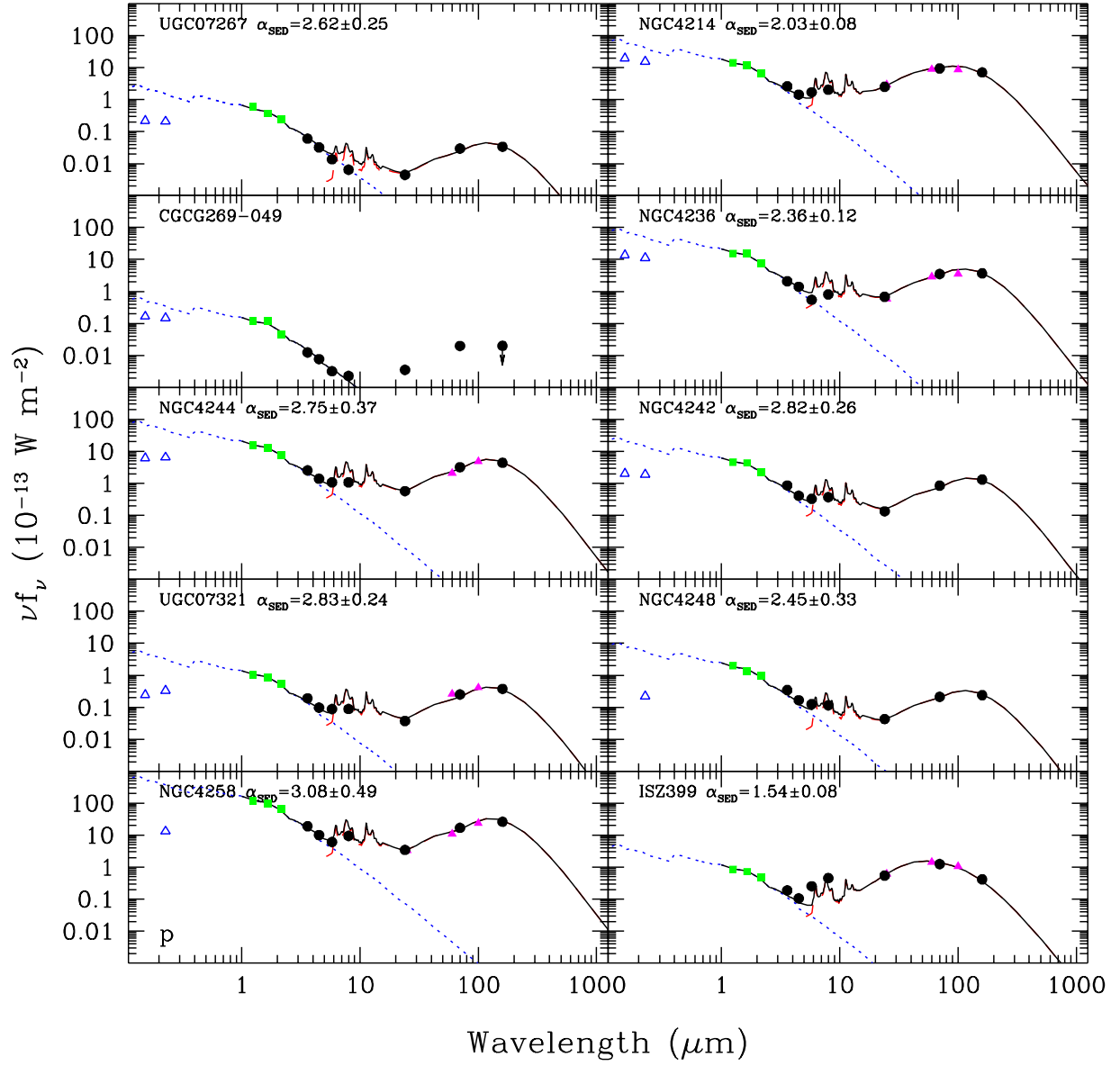


Fig. 10.— Globally-integrated 0.15-160 μm spectral energy distributions for the LVL sample (continued).

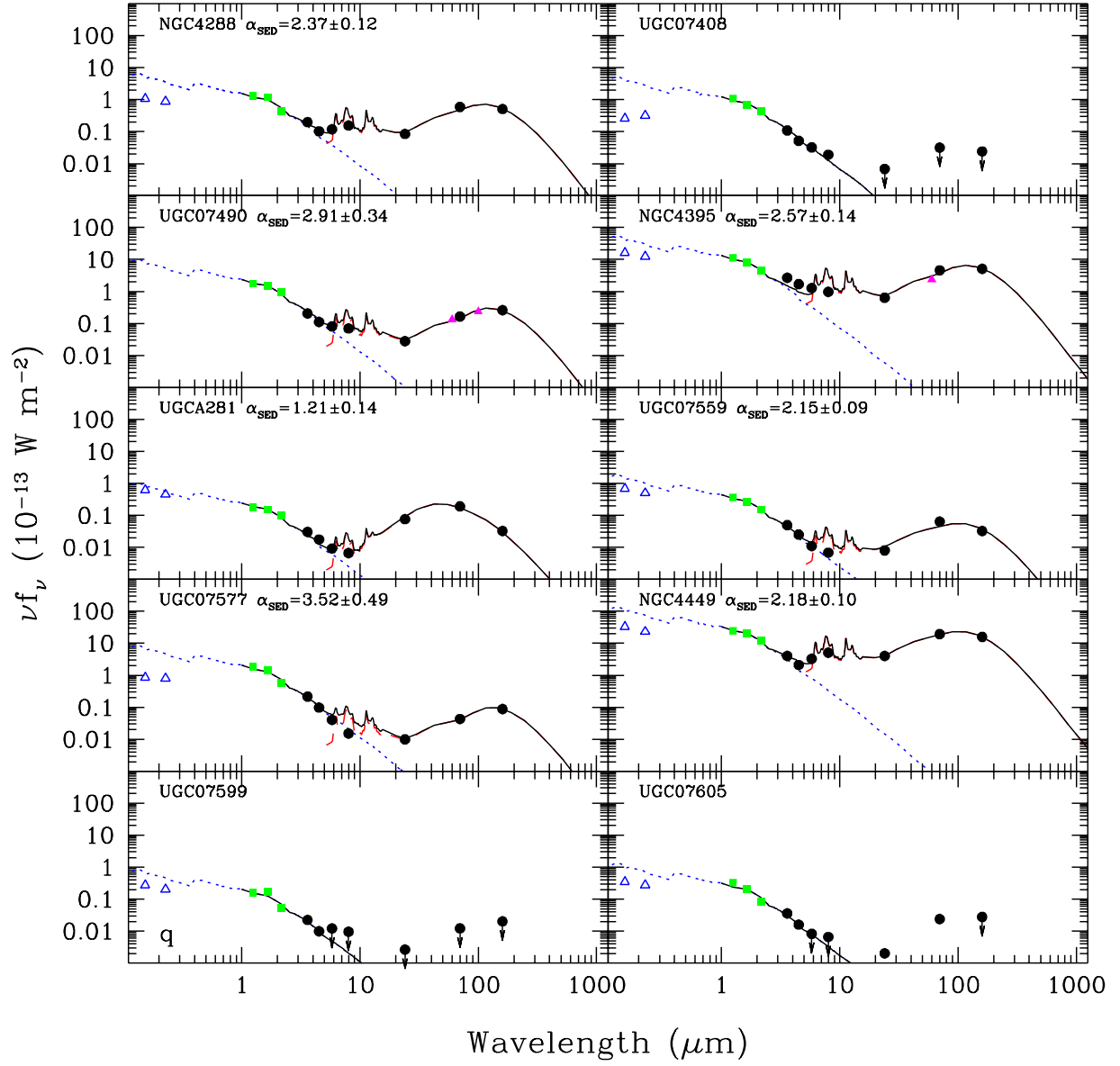


Fig. 10.— Globally-integrated 0.15-160 μm spectral energy distributions for the LVL sample (continued).

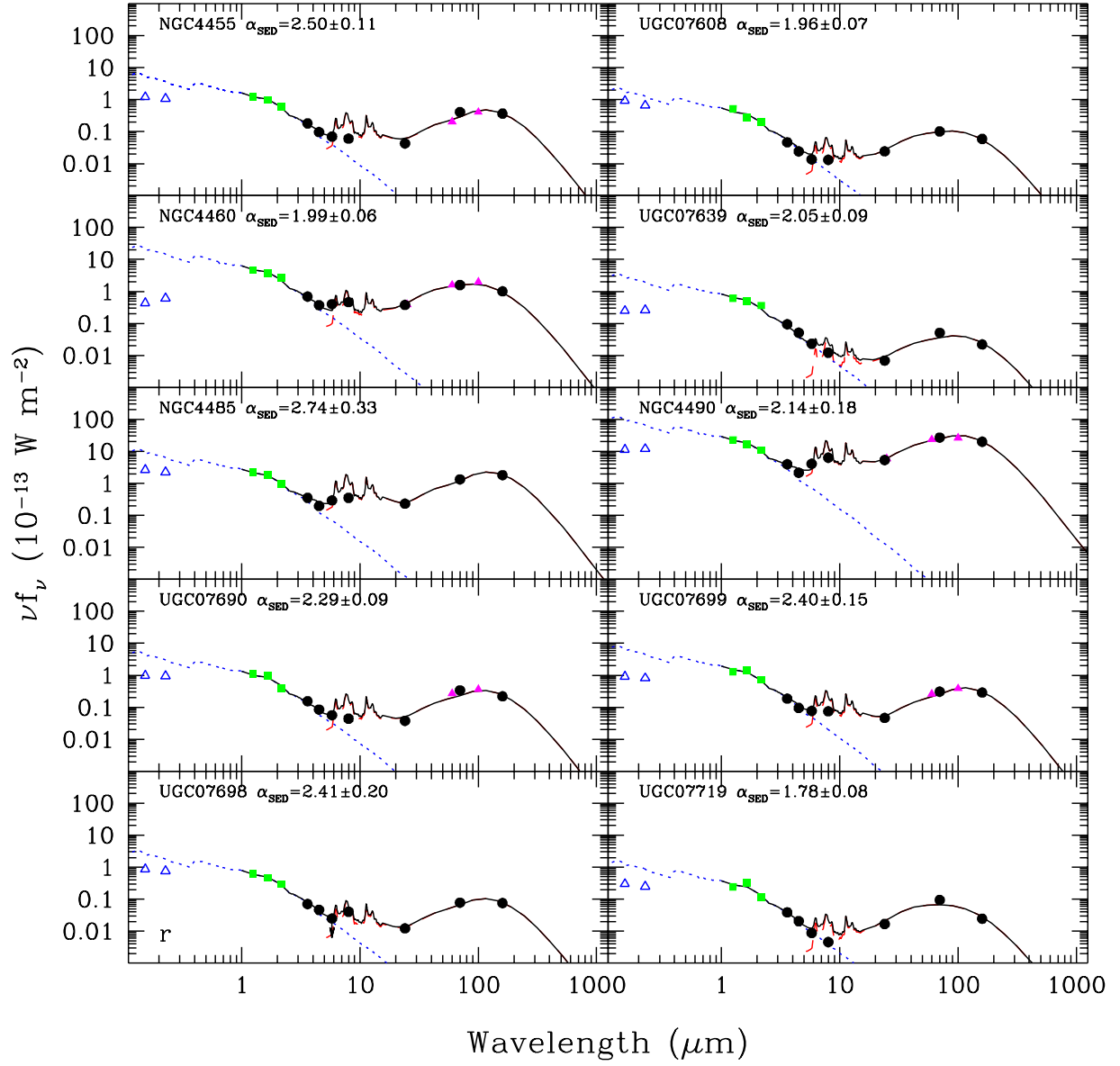


Fig. 10.— Globally-integrated 0.15-160 μm spectral energy distributions for the LVL sample (continued).

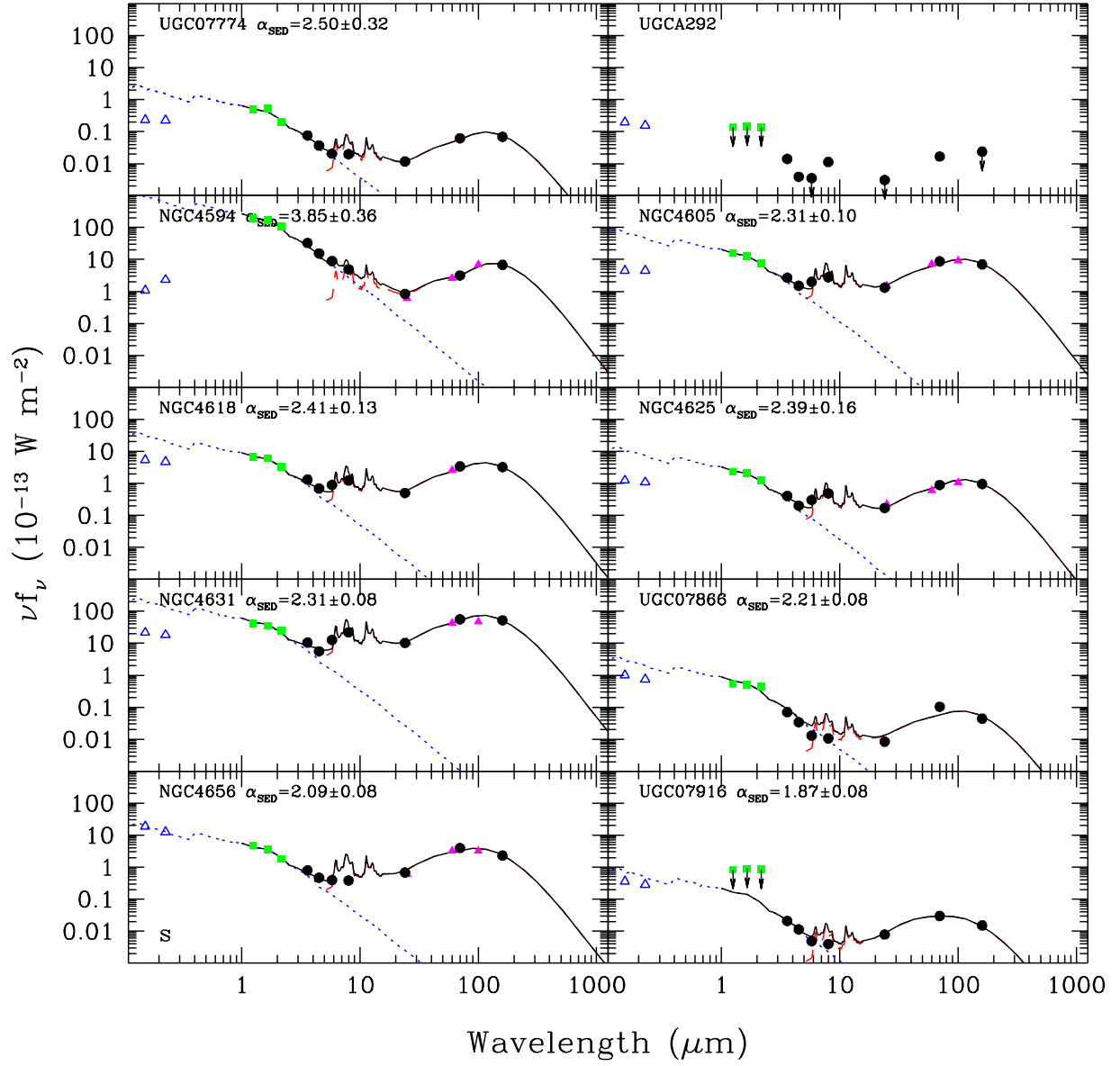


Fig. 10.— Globally-integrated 0.15-160 μm spectral energy distributions for the LVL sample (continued).

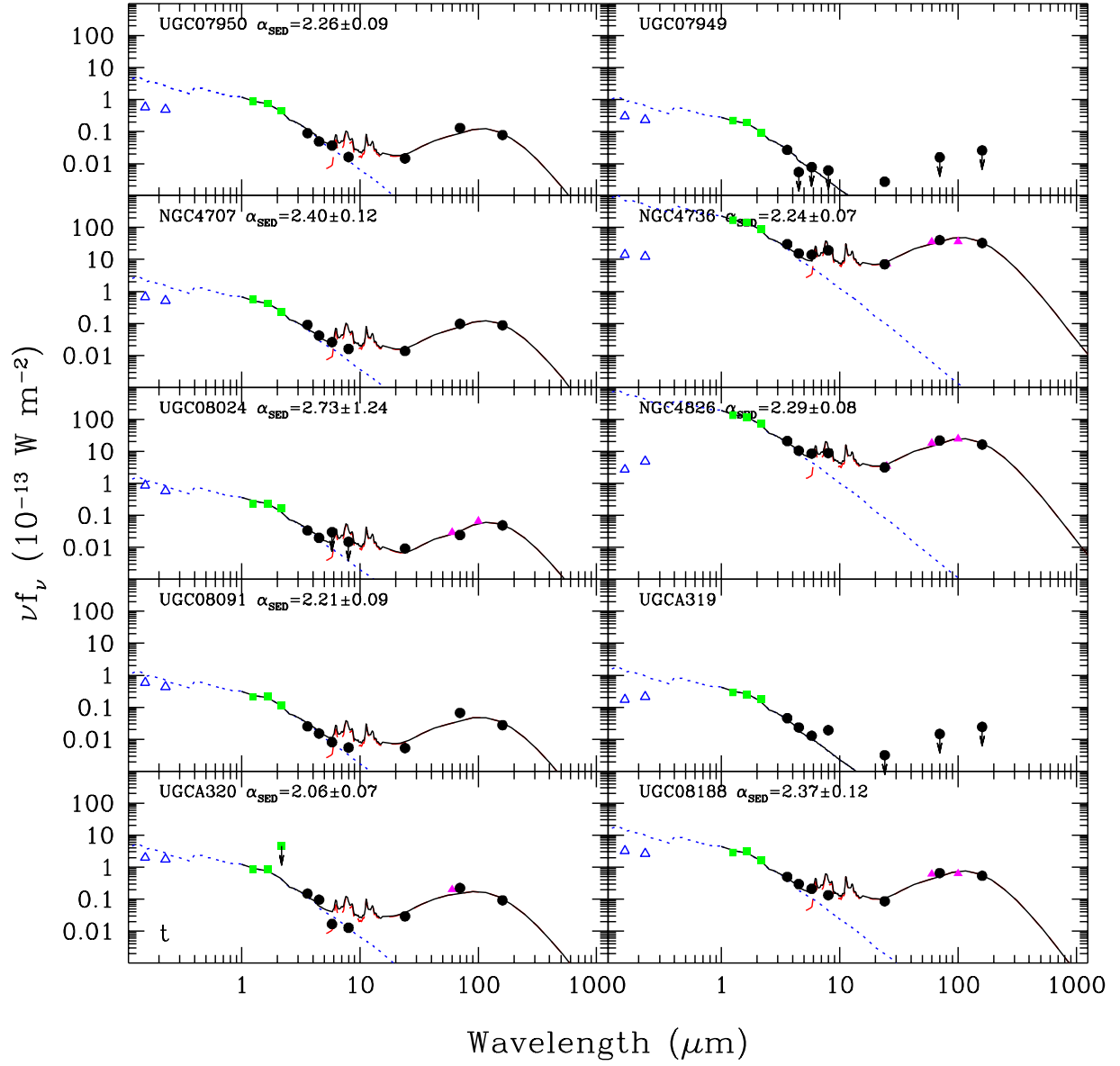


Fig. 10.— Globally-integrated 0.15-160 μm spectral energy distributions for the LVL sample (continued).

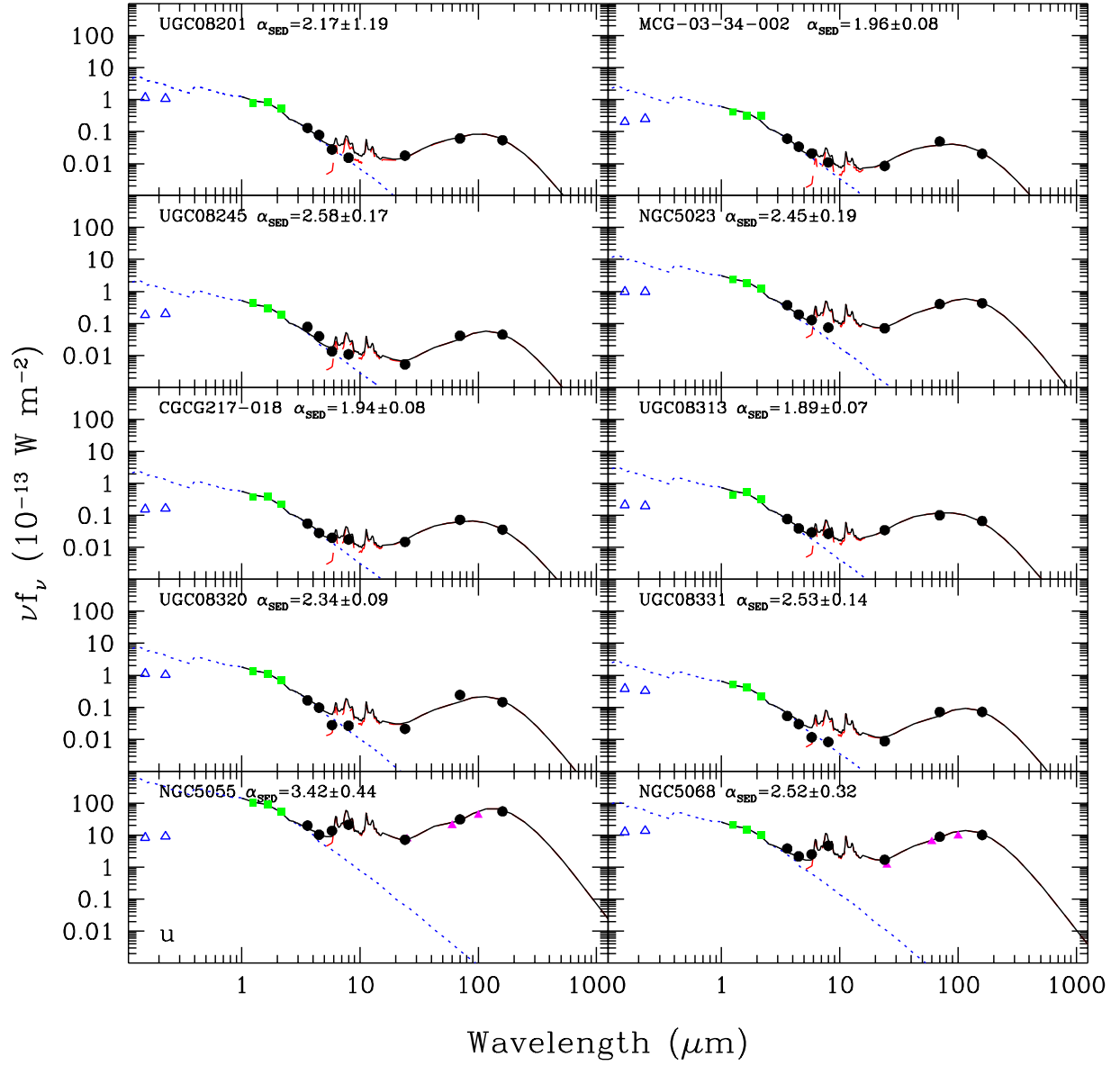


Fig. 10.— Globally-integrated 0.15-160 μm spectral energy distributions for the LVL sample (continued).

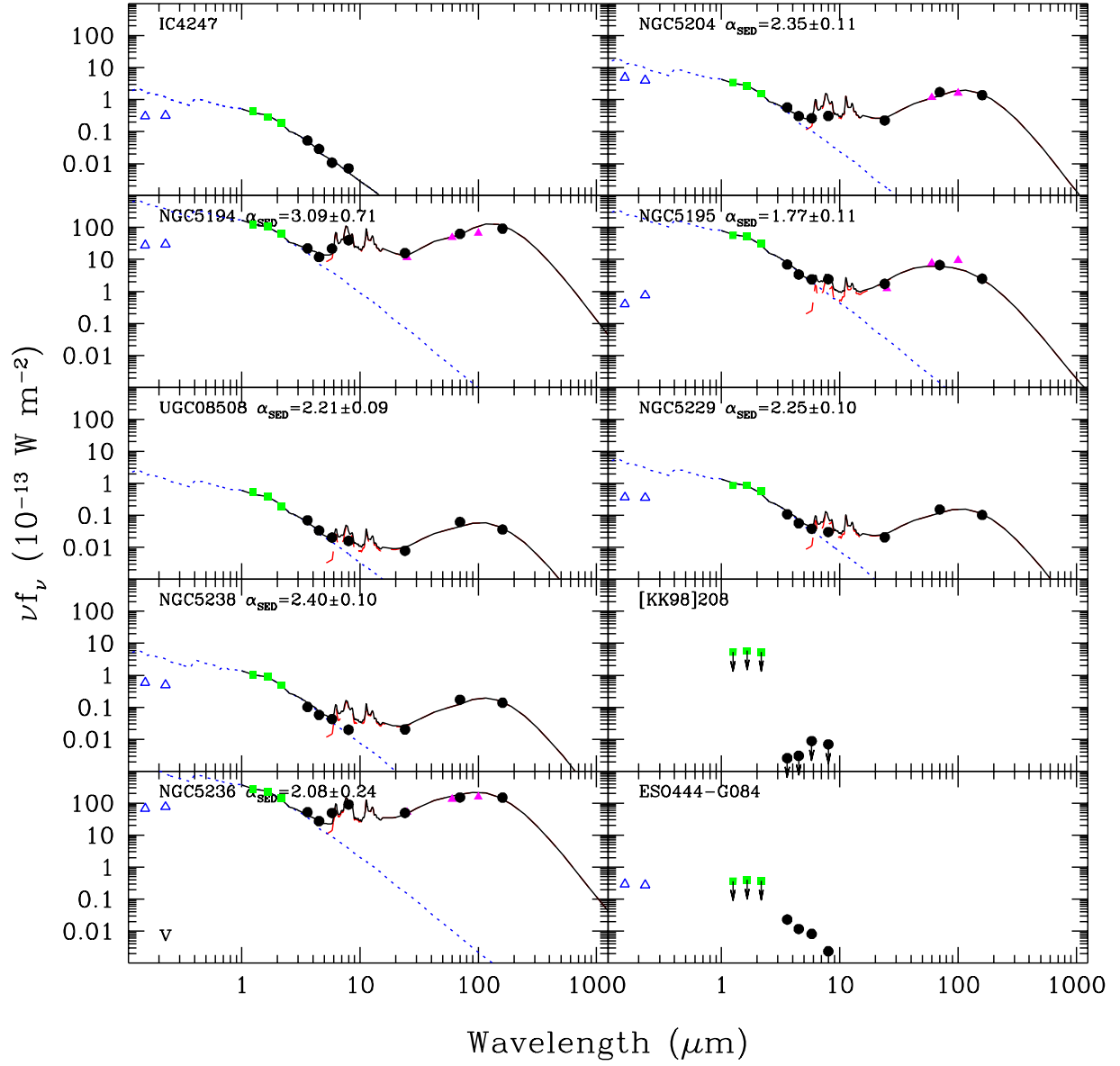


Fig. 10.— Globally-integrated 0.15-160 μm spectral energy distributions for the LVL sample (continued).

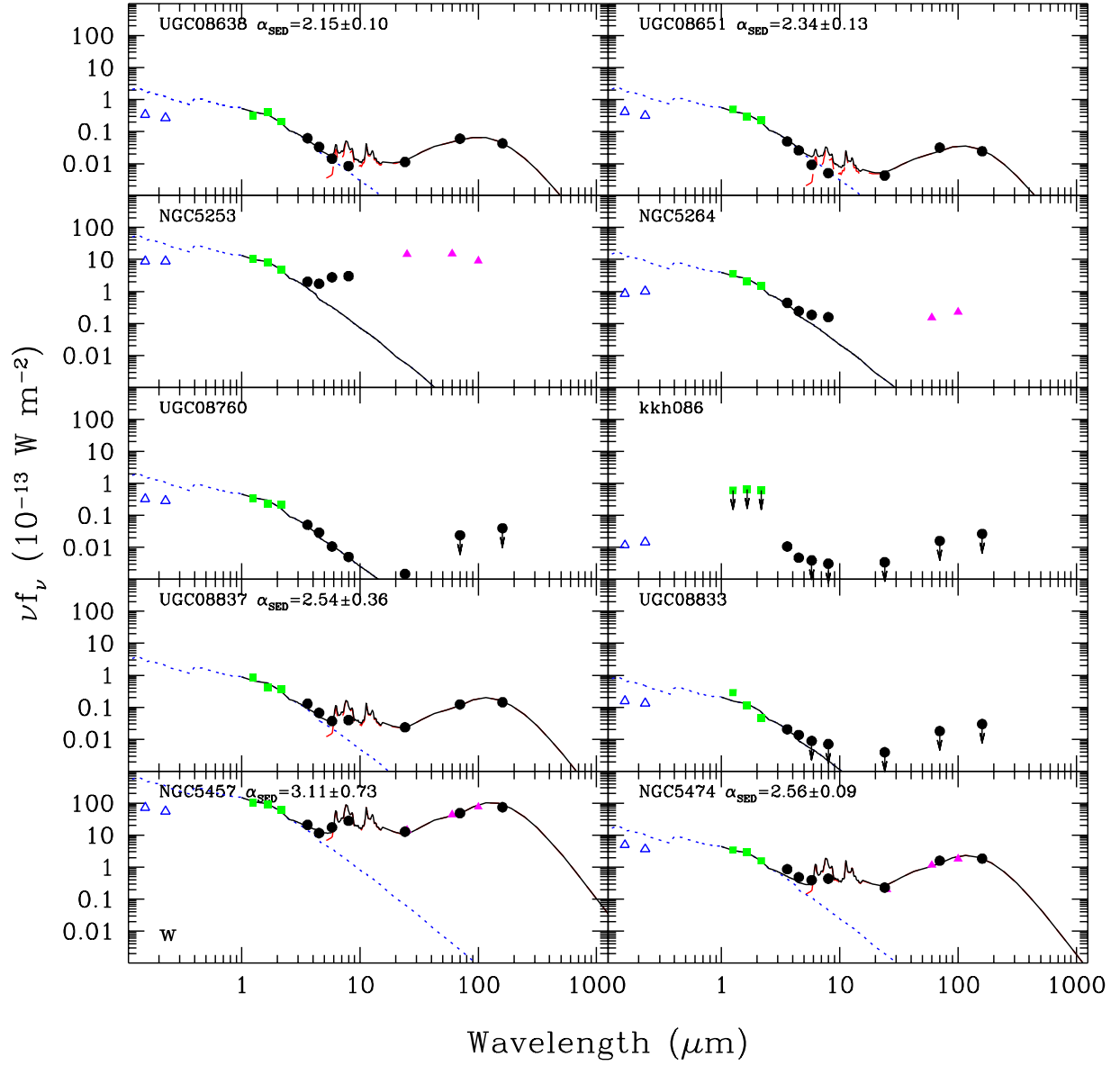


Fig. 10.— Globally-integrated 0.15-160 μm spectral energy distributions for the LVL sample (continued).

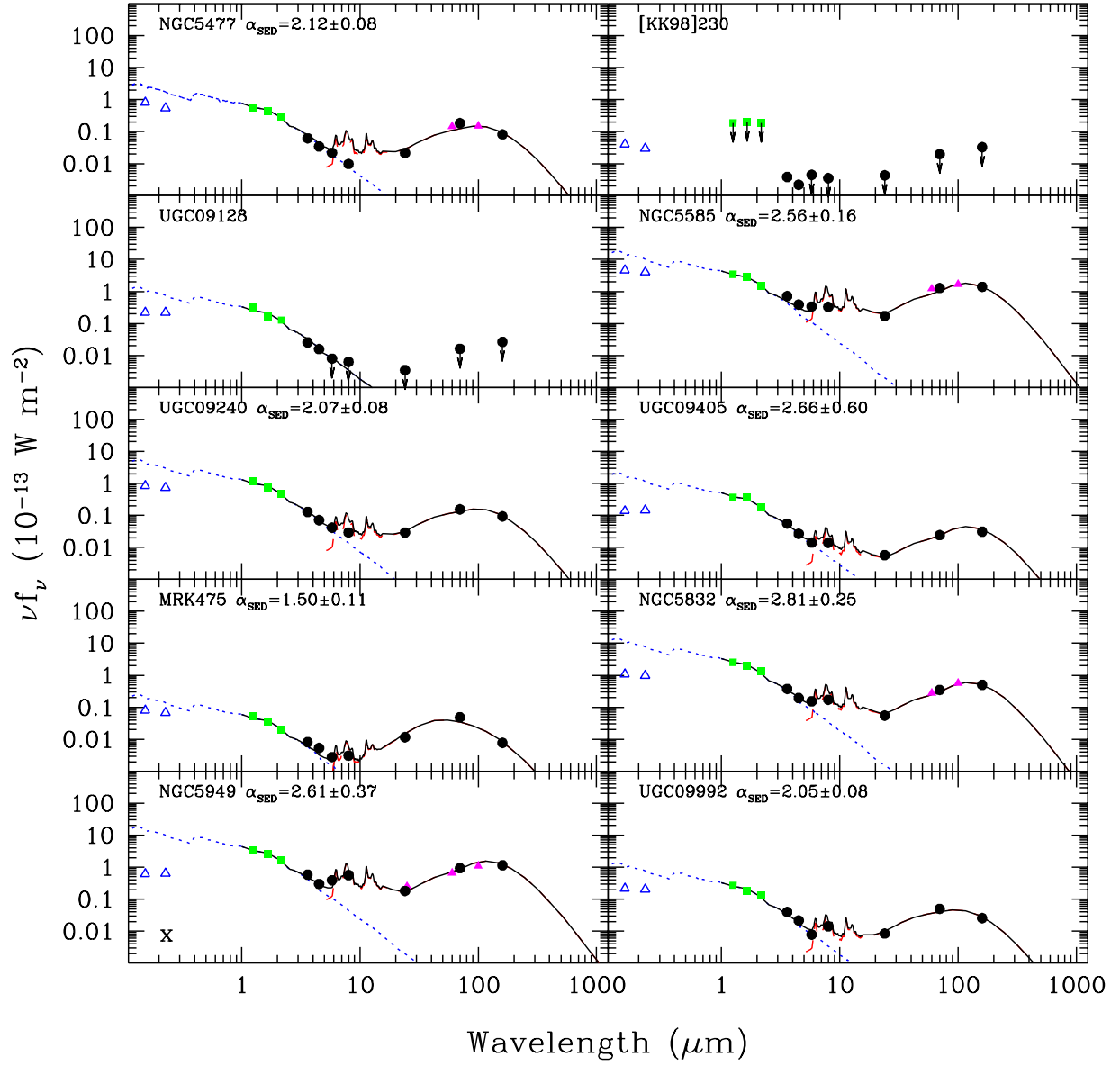


Fig. 10.— Globally-integrated 0.15-160 μm spectral energy distributions for the LVL sample (continued).

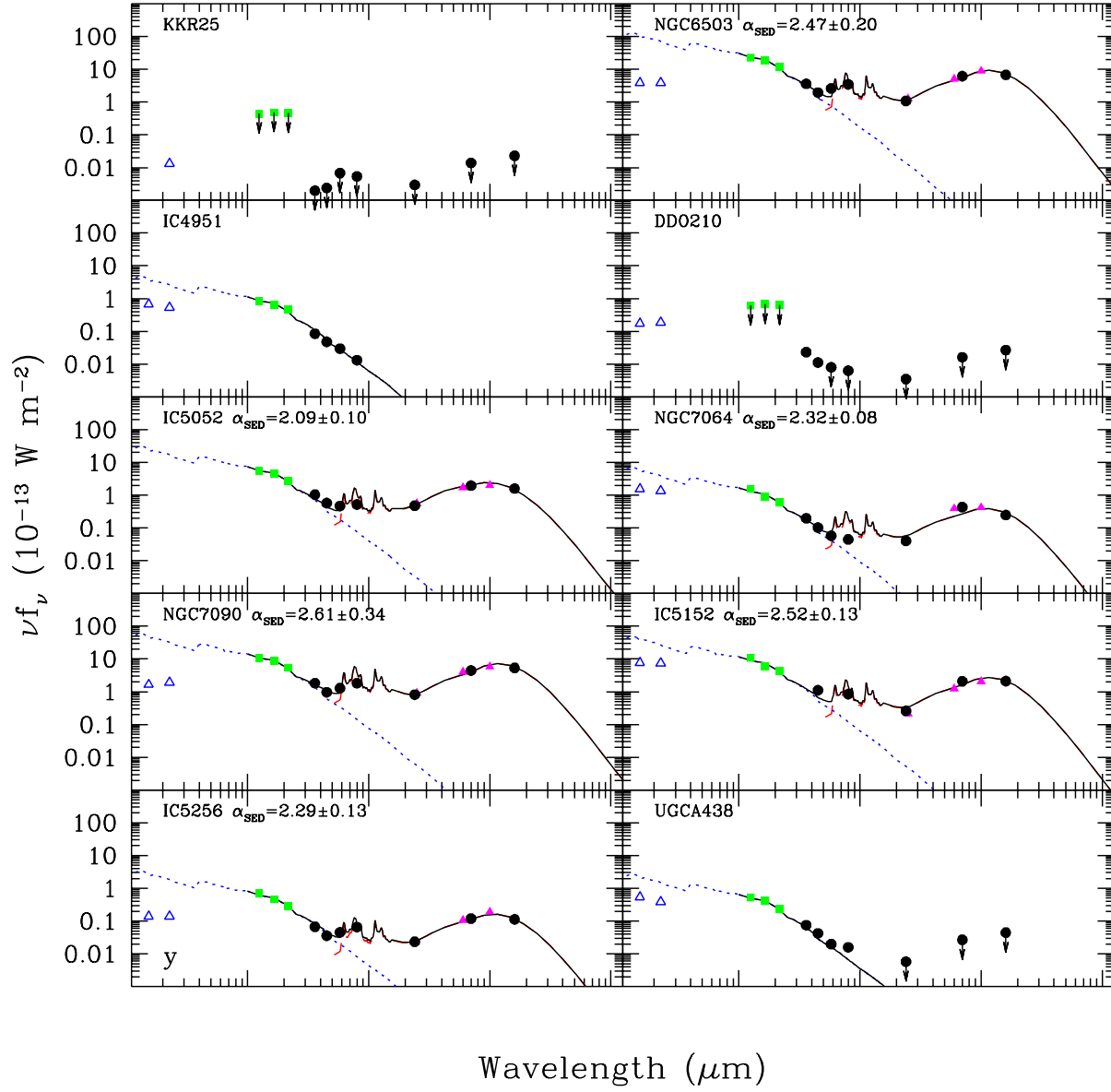


Fig. 10.— Globally-integrated 0.15-160 μm spectral energy distributions for the LVL sample (continued).

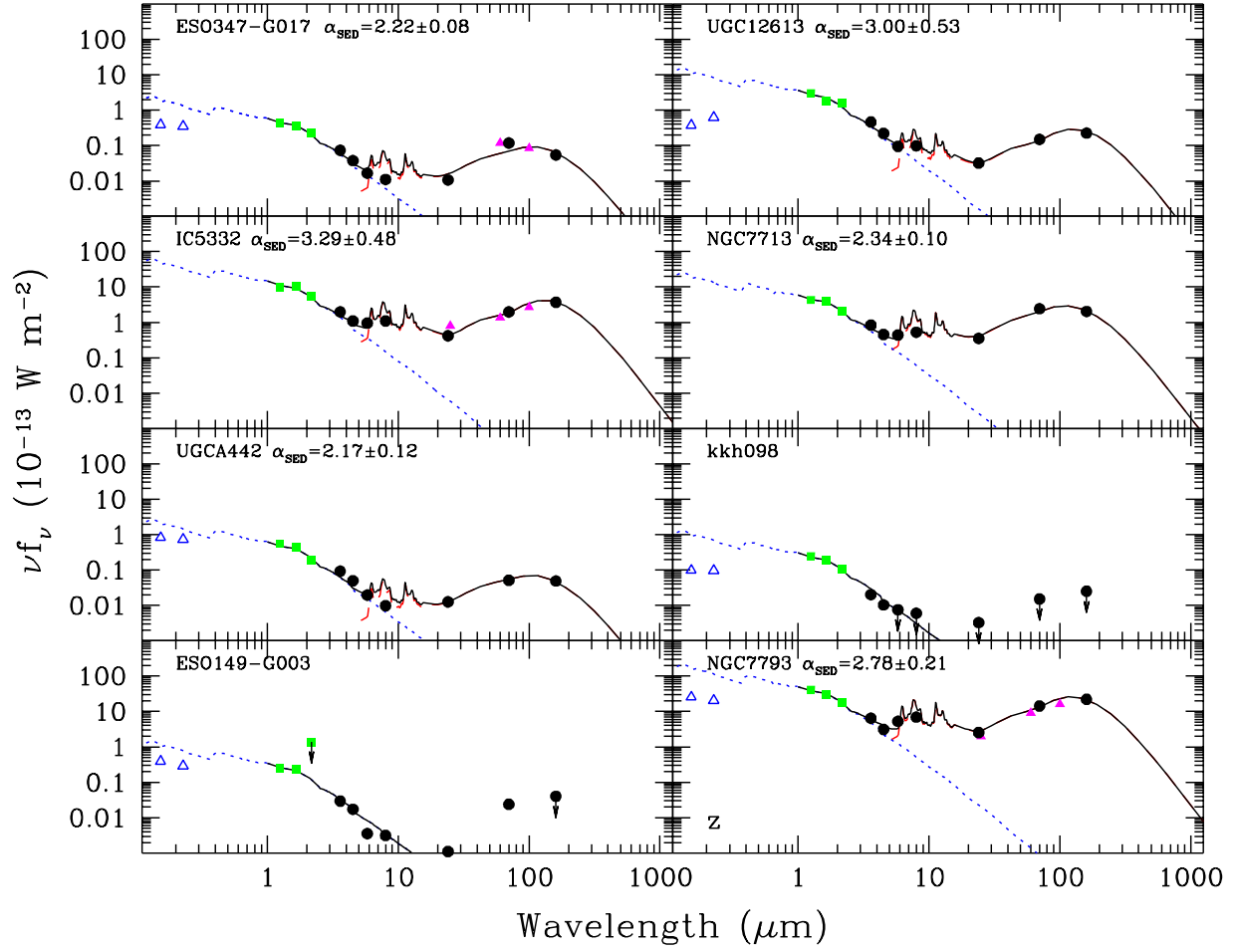


Fig. 10.— Globally-integrated 0.15-160 μm spectral energy distributions for the LVL sample (continued).

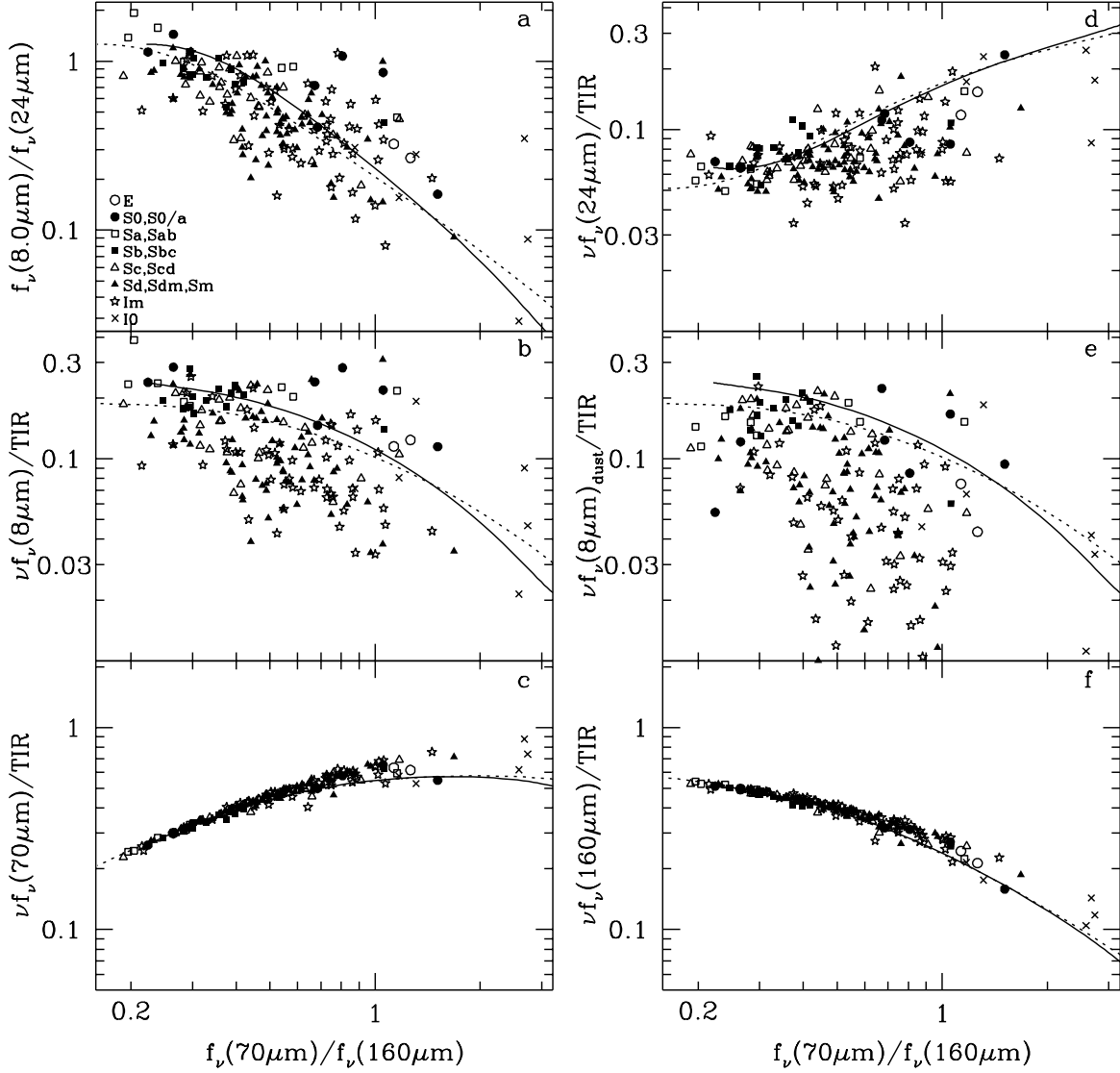


Fig. 11.— The *Spitzer* infrared colors and monochromatic-to-bolometric infrared ratios for globally-integrated LVL data. The solid and dotted lines indicate the SED models of Dale & Helou (2002) and Dale et al. (2001), respectively, derived from the average global trends for a sample of normal star-forming galaxies observed by *ISO* and *IRAS*. A y -axis logarithmic range of ~ 1.6 dex is the same for panels b–f for ease of comparison.

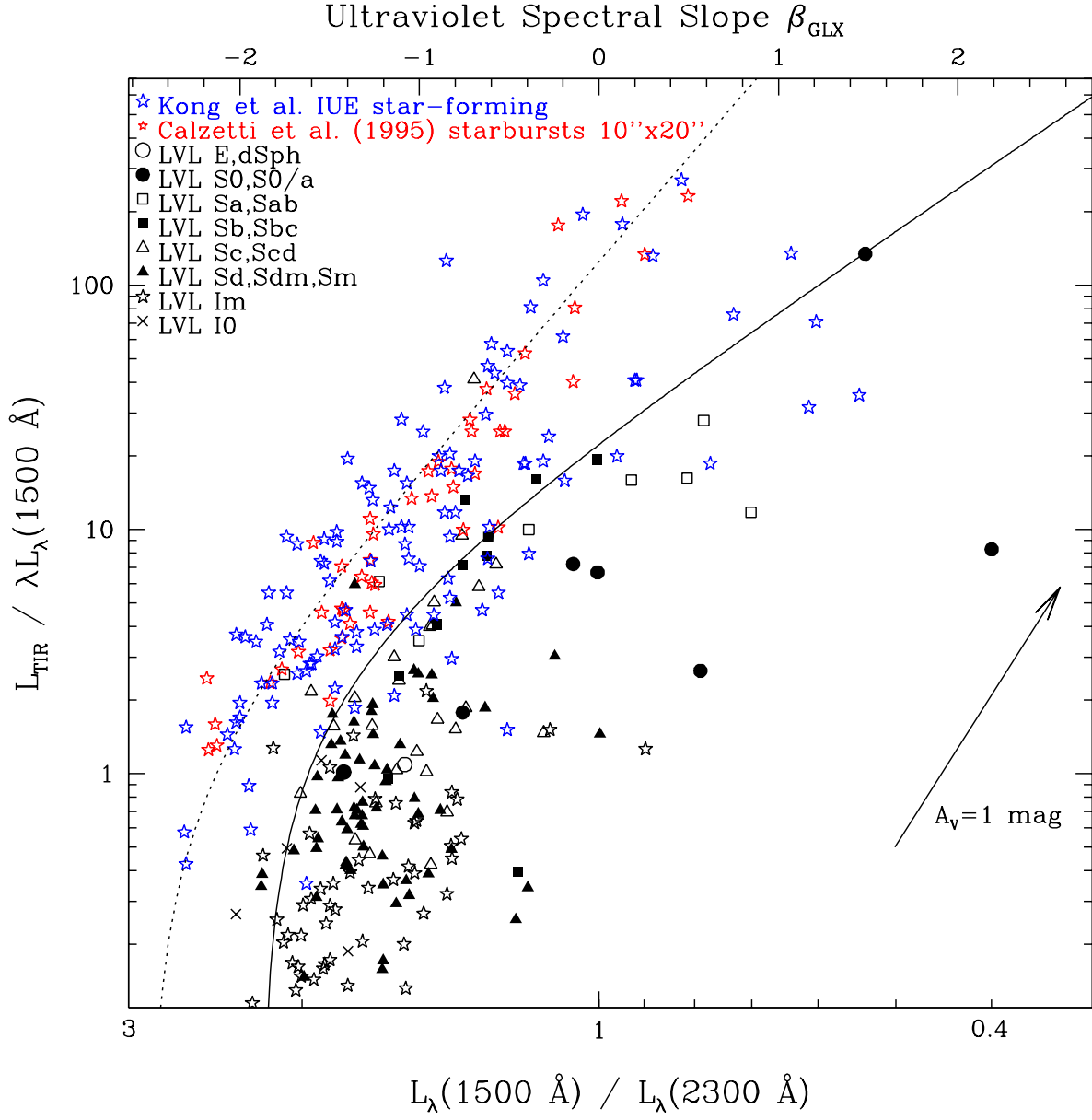


Fig. 12.— The infrared-to-far-ultraviolet ratio as a function of ultraviolet spectral slope. Normal star-forming and starbursting galaxies from Kong et al. (2004) and Calzetti et al. (1995) are plotted in addition to the LVL data points. The dotted curve is that for starbursting galaxies from Kong et al. (2004) and the solid curve is applicable to normal star-forming galaxies (Cortese et al. 2006).

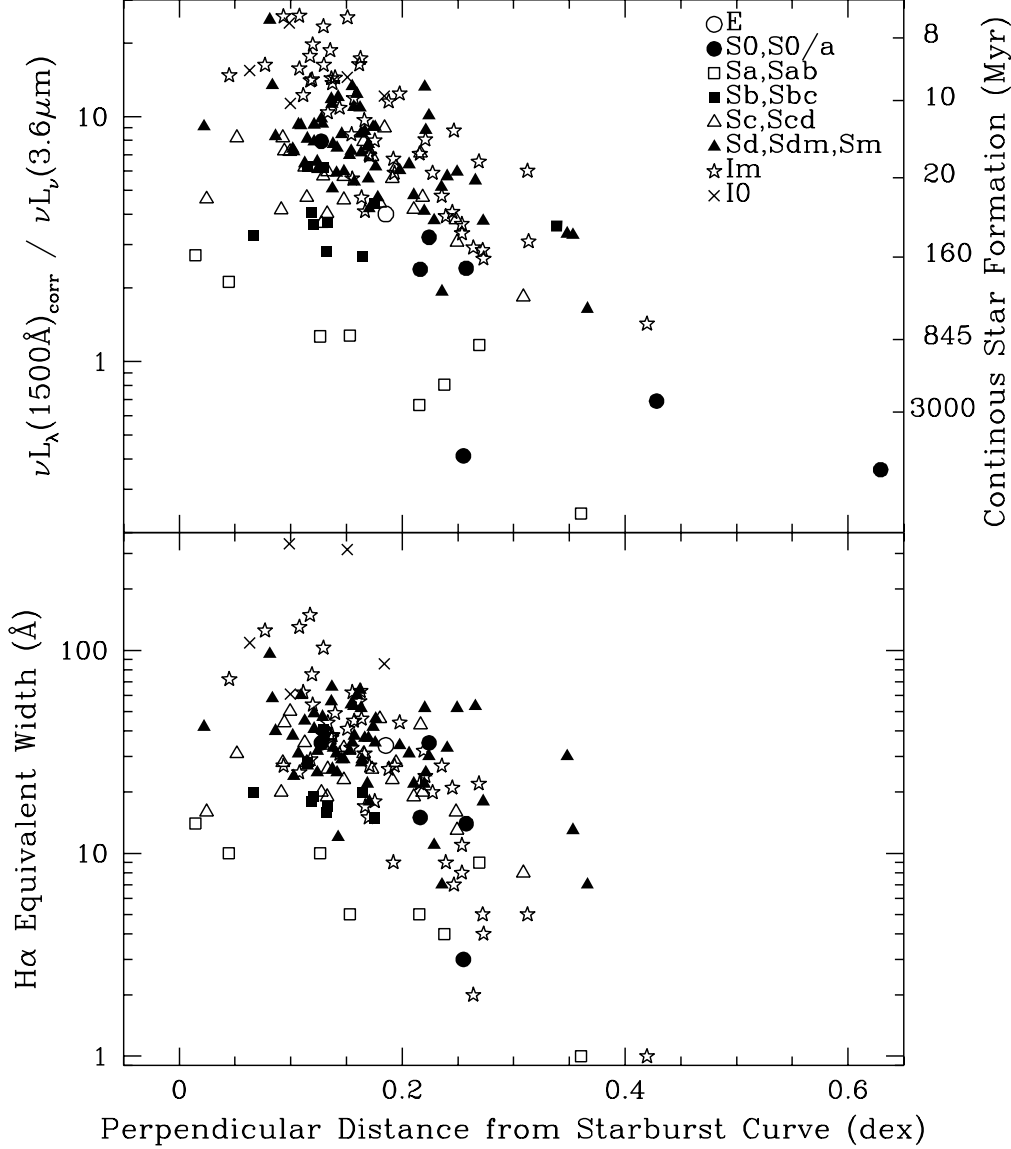


Fig. 13.— The dependence of galaxy star formation history as a function of distance from the starburst relation infrared-to-ultraviolet versus ultraviolet slope, as shown in Figure 12. The left-hand axis is an observable diagnostic of the birthrate parameter, the current star formation rate normalized to the average star formation rate. The righthand axis shows the number of years (continuous) star formation has been occurring, as measured from theoretical spectra. The theoretical spectra utilized are solar metallicity, $1 M_{\odot} \text{ yr}^{-1}$ continuous star formation curves assuming a double power law initial mass function, with $\alpha_{1,\text{IMF}} = 1.3$ for $0.1 < m/M_{\odot} < 0.5$ and $\alpha_{2,\text{IMF}} = 2.3$ for $0.5 < m/M_{\odot} < 100$ (Vazquez & Leitherer 2005).

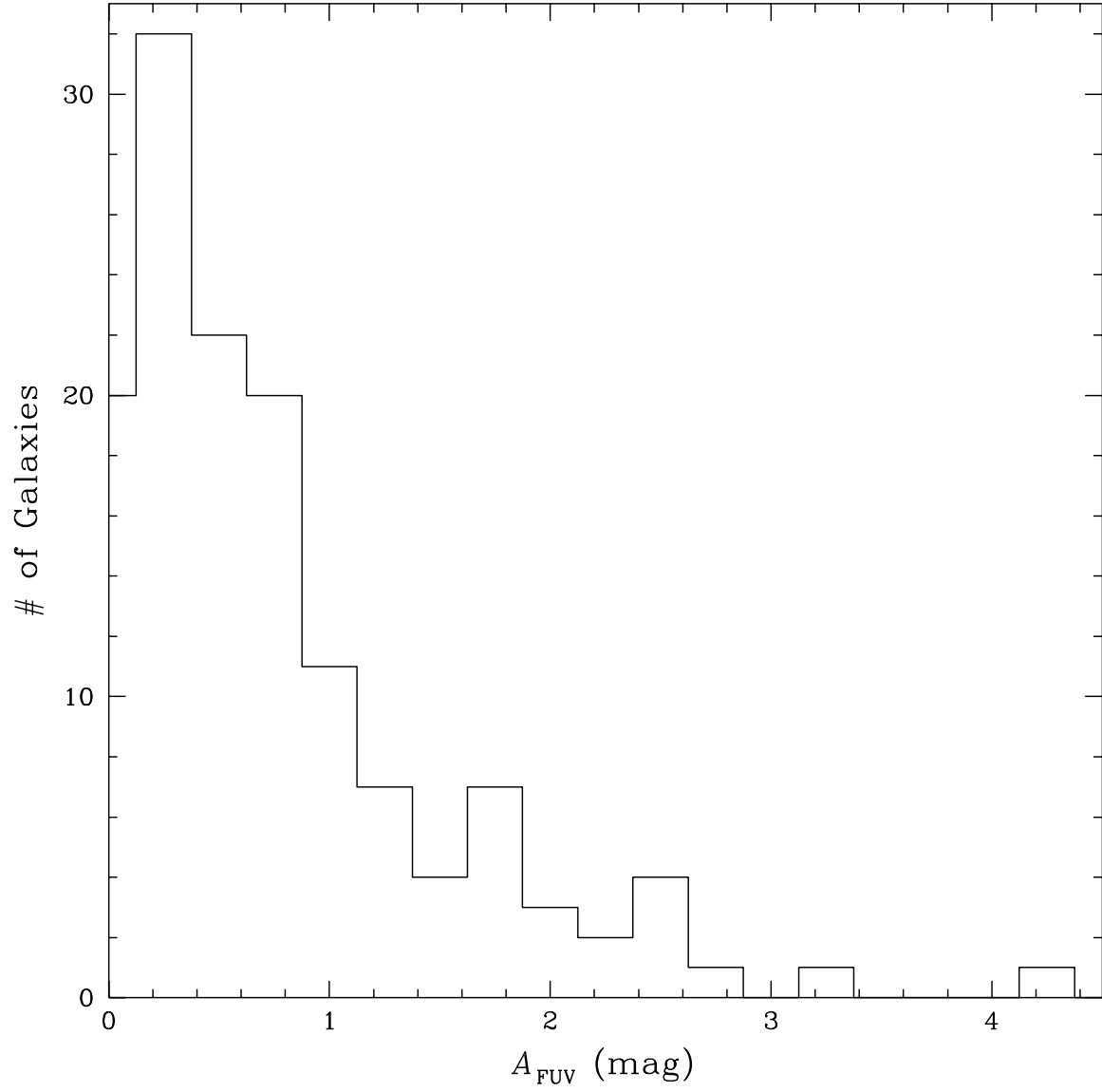


Fig. 14.— The distribution of far-ultraviolet extinctions, computed using the infrared-to-ultraviolet ratio and Equation 2 of Buat et al. (2005).